

Micron-scale monolithically-integrated ultrasonic  
wireless sensing motes for physiological monitoring

Chen Shi

Submitted in partial fulfillment of the  
requirements for the degree of  
Doctor of Philosophy  
in the Graduate School of Arts and Sciences

Columbia University

2020

© 2020

Chen Shi

All Rights Reserved



## ABSTRACT

Micron-scale monolithically-integrated ultrasonic wireless sensing motes  
for physiological monitoring

Chen Shi

There has been increasing interest in emerging implantable medical devices (IMDs) for continuous *in vivo* sensing of physiological signals, including temperature, PH, pressure, oxygen, and glucose, directly at the target locations. Many of these applications can benefit from wireless, miniaturized IMDs that eliminate the percutaneous power cords and facilitate the implantation procedures.

This thesis describes such a device for real-time *in vivo* monitoring of physiological temperature, such as the monitoring of core body temperature and temperature evaluation during thermal-related therapeutic procedures. Featuring a custom temperature sensor chip with a micron-scale piezoelectric transducer fabricated on top of the chip, the monolithic device, in the form of a mote, measures only  $380\text{ }\mu\text{m} \times 300\text{ }\mu\text{m} \times 570\text{ }\mu\text{m}$  and weighs only 0.3 mg. The device utilizes ultrasound for wireless powering and communication through the on-chip transducer and achieves aggressive miniaturization through “chip-as-system” integration. The proposed motes were successfully validated in both *in vitro* experiments with animal tissues and *in vivo* settings with a mouse model. Compared to the state-of-the-art and equivalent commercial devices, the motes performed comparably or better in a fully-wireless manner while presenting a more compact form factor.

Such extreme miniaturization through monolithic integration enables multiple of these motes to be implanted/injected using minimally invasive surgeries with improved biocompatibility and reduced subject discomfort. This offers new approaches for localized *in vivo* monitoring of spatially-fine-grained tem-

perature distributions and also provides a platform for sensing other types of physiological parameters.

---

# Contents

---

<b>List of Figures</b>	<b>iv</b>
<b>List of Tables</b>	<b>xi</b>
<b>Acknowledgments</b>	<b>xii</b>
<b>1 Introduction</b>	<b>1</b>
1.1 Implantable medical devices (IMDs) . . . . .	2
1.2 Thesis outline . . . . .	4
<b>2 Background</b>	<b>5</b>
2.1 Introduction . . . . .	5
2.2 Physiological temperature monitoring . . . . .	6
2.2.1 Monitoring of core body temperature . . . . .	7
2.2.2 Monitoring for therapeutic procedures . . . . .	8
2.2.3 Monitoring for ultrasound neuromodulation . . . . .	8
2.3 Design considerations of IMDs . . . . .	9

2.3.1	Power sources . . . . .	10
2.3.2	Power consumption . . . . .	13
2.3.3	Sensing performance . . . . .	14
2.3.4	Biocompatibility . . . . .	14
2.3.5	System miniaturization . . . . .	15
2.3.6	Biocompatible packaging . . . . .	17
2.4	Focus of this thesis . . . . .	18
<b>3</b>	<b>Design of a Temperature Sensing Mote</b>	<b>19</b>
3.1	Introduction . . . . .	19
3.2	Characterization of piezoelectric materials . . . . .	21
3.2.1	Polyvinylidene difluoride (PVDF) . . . . .	23
3.2.2	Lead zirconate titanate (PZT) . . . . .	25
3.3	Design of a temperature sensor chip . . . . .	29
3.3.1	Front-end rectifier . . . . .	31
3.3.2	Voltage regulator . . . . .	34
3.3.3	Temperature-sensitive oscillator . . . . .	38
3.3.4	Level shifter . . . . .	42
3.3.5	Modulator . . . . .	43
3.3.6	Power breakdown . . . . .	44
3.3.7	Die micrograph . . . . .	45
3.4	Measurement results by direct probing . . . . .	47
<b>4</b>	<b>Microfabrication of the Temperature Sensing Motes</b>	<b>50</b>
4.1	Introduction . . . . .	50
4.2	Integration of PVDF transducers with the sensor chips . . . . .	53
4.2.1	Microfabrication procedures . . . . .	53
4.2.2	Characterization results . . . . .	58
4.3	Integration of PZT transducers with the sensor chips . . . . .	61

4.3.1	Microfabrication procedures . . . . .	61
4.3.2	Characterization results . . . . .	65
<b>5</b>	<b>Experimental Validation of the Temperature Sensing Motes</b>	<b>67</b>
5.1	<i>In-vitro</i> characterization with the wire-bonded motes . . . . .	68
5.1.1	Board design and wire-bonding . . . . .	68
5.1.2	Ultrasound interface . . . . .	72
5.1.3	Data acquisition and analysis . . . . .	75
5.1.4	Graphical user interface (GUI) . . . . .	76
5.1.5	Temperature sensing performance . . . . .	77
5.1.6	Ultrasound beam profile . . . . .	79
5.2	<i>In-vitro</i> experimentation with the standalone motes . . . . .	81
5.2.1	Testing with chicken tissues . . . . .	81
5.2.2	Temperature sensing performance . . . . .	83
5.2.3	Comparison with the state-of-the-art . . . . .	85
5.3	<i>In-vivo</i> evaluation in mice with the standalone motes . . . . .	85
5.3.1	On the brain . . . . .	87
5.3.2	In the hind limb . . . . .	88
5.3.3	Under the sciatic nerve . . . . .	91
<b>6</b>	<b>Conclusions and Future Work</b>	<b>99</b>
6.1	Summary . . . . .	99
6.2	Future work . . . . .	100
6.3	Final thoughts . . . . .	100
	<b>Bibliography</b>	<b>102</b>

---

# List of Figures

---

1.1	Common examples of IMDs implanted at various parts of the interior body for sensing and actuation. . . . .	3
2.1	State-of-the-art applications for wireless power transfer. (a) A cochlear implant; (b) a visual prosthesis; (c) a mobile phone charger; (d) an NFC device; (e) an wirelessly-charged electric vehicle. . . . .	11
3.1	The system diagram demonstrating the operating principles of the mote.	20
3.2	Conceptual figure illustrating the proposed motes with integrated piezo-electric transducers performing <i>in vivo</i> temperature monitoring. . . . .	22
3.3	The electrical model of PVDF. . . . .	24
3.4	The modeled impedance in comparison with the measured impedance for a 2.4-mm-by-2.4-mm piece of PVDF. . . . .	26
3.5	The area-scaling effect of the electrical model of PVDF. . . . .	27
3.6	The electrical model of PZT. . . . .	28

3.7	The modeled impedance in comparison with the measured impedance for a 4-mm-by-4-mm piece of PZT. . . . .	29
3.8	Derived impedance of a $250\ \mu\text{m} \times 250\ \mu\text{m}$ PZT piece scaled from the measured impedance of a $2\ \text{mm} \times 2\ \text{mm}$ PZT piece. . . . .	30
3.9	The output pressure amplitude of the $2\ \text{mm} \times 2\ \text{mm}$ PZT piece with excitation voltage across frequency. . . . .	30
3.10	Block diagram of the temperature sensing mote. . . . .	31
3.11	Schematic of a voltage-doubler rectifier. . . . .	32
3.12	Schematic of an ULP diode used to implement $D_1$ and $D_2$ in Figure 3.11. . . . .	33
3.13	Detailed schematic of the rectifier with $C_1$ replaced with the electrical model of PZT and $D_1$ and $D_2$ replaced with ULP diodes. . . . .	33
3.14	Schematic of an all-NMOS subthreshold voltage reference. . . . .	35
3.15	Schematic of the reference in Figure 3.14 with stacked NMOS diodes. . . . .	36
3.16	Schematic of the the complete voltage regulator. . . . .	37
3.17	Schematic of a relaxation oscillator. . . . .	38
3.18	The voltage waveforms at nodes $V_1$ , $V_2$ , and $V_3$ in Figure 3.17. . . . .	39
3.19	The pseudo-resistor used to implement the resistor $R$ in Figure 3.17. . . . .	40
3.20	Schematic of a conventional level shifter. . . . .	42
3.21	Schematic of a contention mitigated level shifter used in this design. . . . .	43
3.22	The simulated power breakdown of the major circuit blocks. . . . .	44
3.23	The die micrograph showing the three groups of temperature sensing chips with varying sizes. . . . .	45
3.24	The micrograph of one $350\text{-}\mu\text{m}\text{-by-}250\text{-}\mu\text{m}$ chip showing the locations of the major circuit blocks. . . . .	46
3.25	(a) The testing setup on the probe station to test the oscillators; (b) a micrograph showing three DC probes landing on the testing pads of an oscillator for powering up the oscillator and taking measurements. . . . .	47

3.26	(a) The line sensitivity of six oscillators; (b) the power consumption of the six oscillators. . . . .	48
3.27	(a) The line sensitivity of three oscillators with voltage regulation; (b) the power consumption of two of the three regulated oscillators. . . . .	48
4.1	(a) The micrograph of one 1.1-mm-by-1-mm chip with the input pad ( $150\text{ }\mu\text{m} \times 65\text{ }\mu\text{m}$ ) and the ground pad ( $1\text{ mm} \times 1\text{ mm}$ ) labeled; (b) the micrograph of one 600- $\mu\text{m}$ -by-500- $\mu\text{m}$ chip with the input pad ( $100\text{ }\mu\text{m} \times 65\text{ }\mu\text{m}$ ) and the ground pad ( $500\text{ }\mu\text{m} \times 500\text{ }\mu\text{m}$ ) labeled; (c) the micrograph of one 350- $\mu\text{m}$ -by-250- $\mu\text{m}$ chip with the input pad ( $65\text{ }\mu\text{m} \times 65\text{ }\mu\text{m}$ ) and the ground pad ( $250\text{ }\mu\text{m} \times 250\text{ }\mu\text{m}$ ) labeled. . . . .	51
4.2	The comparison of chip surface before and after removing polyimide. . .	53
4.3	Effects of temperature on the $d_{33}$ of PVDF. . . . .	54
4.4	Surface roughness of PVDF before and after RIE treatment. . . . .	55
4.5	The tensile test results of a plasma-treated PVDF piece. . . . .	55
4.6	Fabrication flow for integrating PVDF with the CMOS chips. (a) Removal of polyimide and bonding of the CMOS die to a carrier with PMMA and silicone and (b) adhesion of pre-treated PVDF piece and the die with SU-8 and (c) patterning of PVDF areas on top of the chip signal pads and (d) RIE etching to create PVDF micro-structures and (e) patterning of chip areas and (f) metal deposition and lift-off for ground connection. . . . .	56
4.7	(a) A PVDF micro-structure integrated with the ground pad of a 1.1-mm-by-1-mm chip; (b) a PVDF micro-structure integrated with the ground pad of a 600- $\mu\text{m}$ -by-500- $\mu\text{m}$ chip; (c) a PVDF micro-structure integrated with the ground pad of a 350- $\mu\text{m}$ -by-250- $\mu\text{m}$ chip. . . . .	57



4.8	(a) A fully-fabricated PVDF micro-structure integrated with a 1.1-mm-by-1-mm chip;(b) a fully-fabricated PVDF micro-structure integrated with a 600- $\mu\text{m}$ -by-500- $\mu\text{m}$ chip; (c) a fully-fabricated PVDF micro-structure integrated with a 350- $\mu\text{m}$ -by-250- $\mu\text{m}$ chip. . . . .	58
4.9	(a) A 1.1-mm-by-1-mm standalone sensing mote; (b) a 600- $\mu\text{m}$ -by-500- $\mu\text{m}$ standalone sensing mote; (c) a 350- $\mu\text{m}$ -by-250- $\mu\text{m}$ standalone sensing mote.	59
4.10	Raman spectrum of one micro-fabricated PVDF structure in comparison with a pristine PVDF piece. . . . .	60
4.11	AFM measurements on a fabricated PVDF structure (a) without voltage excitation and (b) with 1-Hz and 10-Hz 10-V peak-to-peak square wave excitations; (c) a height plot along a vertical line on (b). . . . .	60
4.12	The fabrication procedures for monolithically integrating the CMOS chips with PZT transducers, including (a) photolithographic patterning and Cr/Au deposition, and (b) lift-off of PR to create contacts on both sides of the PZT that match with the ground pads on CMOS chips, and (c) adhesion of the ACF with the bottom side of the PZT and dicing of the PZT from the bottom side, and (d) bonding of the PZT to the CMOS chips with precise alignment, and (e) dicing of the PZT from the top side to create free-standing PZT transducers, and (f) deposition of copper to connect the top sides of the PZT transducers with the corresponding input pads. . . . .	62
4.13	The microphotograph of the major fabrication procedures for monolithically integrating the CMOS chips with PZT transducers: (a) after bottom-side dicing; (b) after bonding the PZT die with the CMOS die; (c) after the top-side dicing; (d) after metal deposition for the top-side connection.	64

4.14	(a) Fully-integrated chips separated through a dicing process; (b) an exploded-view schematic illustration of the major components of a fully-integrated and released standalone mote, including the CMOS temperature sensor chip with the two exposed Al pads, the microscale PZT transducer covered in Cr/Au on both sides, the ACF, and the Cu layer; (c) a detailed photograph of the mote with dimensions; (d) an SEM image of the mote; (e) the mote placed on top of a United States penny; (f) the mote placed on top of a United States dime with a different orientation as in (e). . . .	66
5.1	(a) The schematic of the testing board; (b) a populated testing board. . .	68
5.2	(a) A testing board with a chip attached for wire-bonding; (b) the wire-bonding process; (c) the board with the chip wire-bonded to it. . . . .	69
5.3	The setup for PSRR measurements. . . . .	70
5.4	PSRR measurements for both regulators. . . . .	71
5.5	(a) A fully-fabricated mote wire-bonded to a board; (b) the experimental setup consisting of the PCB inserted into a 3D-printed case filled with DI water for testing the performance of the mote. . . . .	71
5.6	The Verasonics Vantage Research Ultrasound System. . . . .	72
5.7	The waveform of the ultrasound used to power the mote, showing a pressure amplitude of $\sim 305$ kPa with a $100 \mu\text{s}$ pulse repetition period. . . .	73
5.8	The ultrasound intensity to activate the mote with respect to the number of cycles in each pulse. . . . .	74
5.9	The output voltage waveforms of the rectifier, the two regulators, and the oscillator from testing of a wire-bonded mote with an ultrasound input at $37^\circ\text{C}$ , showing an oscillation frequency of $\sim 7.6$ Hz. . . . .	74
5.10	(a) Backscattering data acquired at $27^\circ\text{C}$ with an SNR of 25.05 dB; (b) backscattering data acquired at $50^\circ\text{C}$ with an SNR of 28.04 dB. . . . .	76

5.11	The GUI for controlling the ultrasound interface and acquiring and analyzing the backscattering data. . . . .	77
5.12	(a) The temperature curves of three wire-bonded motes; (b) the temperature error for the motes with an average of $+0.18/-0.29$ °C. . . . .	78
5.13	The temperature resolution of the three wire-bonded motes. . . . .	79
5.14	Top: an illustration of measuring the ultrasound beam profile using a fabricated $250\text{ }\mu\text{m} \times 250\text{ }\mu\text{m}$ PZT transducer; bottom left: the pressure map in the XY-plane at a 22-mm distance in a $2\text{ mm} \times 2\text{ mm}$ region; bottom right: the beam pattern in the XZ-plane in a $2\text{ mm} \times 2\text{ mm}$ region.	80
5.15	(a) The peak pressure amplitude received by the PZT transducer with respect to the incident angle from $-20^\circ$ to $20^\circ$ ; (b) the required ultrasound intensity to activate the mote with respect to the incident angle. . . . .	81
5.16	The experimental setup for fully-wireless ultrasound testing with a mote released from the die. Similar to the testing setup for the wire-bonded motes, the standalone mote was mounted on a case and covered with a piece of 3-mm-thick chicken thigh as a biological tissue medium. . . . .	82
5.17	The ultrasound image showing a piece of chicken thigh placed on top of a sensing mote during a fully-wireless testing. . . . .	83
5.18	(a) The temperature curves of three standalone motes; (b) the temperature error for the motes with an average of $+0.26/-0.26$ °C. . . . .	84
5.19	The calibrated temperature outputs from the six tested motes compared with the reference temperature. . . . .	84
5.20	(a) A long-term measurement of over four hours of one wireless mote at $\sim 45$ °C compared with the reference thermometer; (b) the Allan deviation of the long-term temperature measurement in (a) showing a floor of $<138.6$ ppm (limited by the measurement time). . . . .	85
5.21	The surgical procedures for subdermal implantation on the brain. . . . .	88
5.22	The experimental setup with the mote implanted on the brain. . . . .	89

5.23	The ultrasound image showing the mote located above the skull. . . . .	89
5.24	The acoustic data obtained with the mote implanted on the brain. . . . .	90
5.25	A continuous temperature recording for 10 minutes with the mote im- planted on the brain. . . . .	90
5.26	(a) A mote fixed on a PI substrate for implantation; (b) subdermal im- plantation of the mote in the hind limb. . . . .	91
5.27	The experimental setup with the mote implanted in the hind limb. . . .	91
5.28	The acoustic data obtained with the mote implanted in the hind limb. .	92
5.29	A continuous temperature recording for $\sim 6$ minutes with the mote im- planted in the hind limb. . . . .	92
5.30	(a) A cartoon illustration of the strategy for implantation at the sciatic nerve; (b) implantation of two motes at the sciatic nerve. . . . .	93
5.31	Illustration of applying FUS from beneath the sciatic nerve. . . . .	94
5.32	The experimental setup for measuring the EMG responses in the leg of a mouse with FUS stimulation at the sciatic nerve. . . . .	95
5.33	EMG signals recorded with FUS stimulation at the sciatic nerve. . . . .	96
5.34	Area-under-the-curve analysis of EMGs acquired from FUS stimulation. .	97
5.35	The experimental setup to measure temperature increases with FUS stim- ulation. . . . .	97
5.36	The acoustic data obtained with the motes implanted under the sciatic nerve. . . . .	98
5.37	(a) The temperature increases with four different stimulation intensities; (b) negligible temperature increases with single FUS pulses. . . . .	98

---

# List of Tables

---

3.1	Derived component values of different sizes of PVDF. . . . .	25
3.2	Extracted component values of different sizes of PZT. . . . .	28
5.1	Comparison with the state-of-the-art. . . . .	86

---

# Acknowledgments

---

I am finally reaching the end of my doctoral study. This journey is made possible only with the tremendous amount of help and support from quite a few people around me. I am enormously grateful to every single one of them. First, I would like to express my deepest gratitude to my advisor, Professor Kenneth L. Shepard, who has motivated me to work on the cutting edge problems in the field of bioelectronics and guided me throughout my entire graduate study with his enthusiasm, intelligence, and vision. Without his strong support and belief in me, I would not have accomplished my thesis work, nor would I have decided to continue my endeavor in circuit and system design following my graduation.

In addition, when I started this thesis project and felt a lack of heavy circuit design flavor due to the nature of the project, Ken was very considerate and assigned me an additional project in collaboration with Dr. Tiago Costa to enhance my circuit background. This initiated my multi-year pleasant collaboration with Tiago, who has been a great mentor and friend to me and owns my most sincere gratitude. Tiago is so friendly, knowledgeable, experienced, and willing to share his ideas and offer detailed instructions.

I also would like to thank the members of my committee, Professor Ioannis Kymissis, Professor Elisa E. Konofagou, Professor Christine P. Hendon, and Professor Samuel Sia, for their time, advice, and encouragements. Particularly, Professor Konofagou has provided valuable guidance and help for the ultrasound-related portion and the *in vivo* experimentation of my thesis.

Special thanks to Dr. Victoria Andino Pavlovsky and Stephen Alexander Lee for their strong support and patient help with *in vivo* surgeries and experiments. In addition, I would like to thank Jeffrey Elloitt and Yihan Zhang for providing many technical help and discussions to me throughout the years. I am also very grateful to many of the amazing group members in the Shepard Lab, including but not limited to Jordan Thimot, who collaborated with me on two projects when we first started in the group, Dr. Siddharth Shekar, Rizwan Huq, Dr. Kukjoo Kim, Jaebin Choi, Dr. Kevin Tien, Nanyu Zeng, Fengqi Zhang, Peijie Ong, Cheng Tan, Dr. David Tsai, Boyan Penkov, Adrian Bradd, and Jake Rabinowitz. Their spiritual and technical supports mean a lot to me, without which I could not have survived this rewarding yet challenging journey.

Finally, my greatest gratitude and appreciations go to my dear parents, who have provided endless love, tender care, and unstinted support to me without any complain. They are always by my side, giving me the courage and energy to keep moving forward, experiencing with me every moment in my life, be it joyful or stressful, and accompanying me throughout each stage of my growth.

In memory of my grandmother, Yafang Lu.



---

# Chapter 1

## Introduction

---

The significant invention of the integrated circuit (IC) in 1958 followed by the rapid growth of the complementary metal–oxide–semiconductor (CMOS) technology as the dominating IC fabrication process [1] has brought us into a digital age. Virtually every electronic device in our daily life is equipped with CMOS ICs, where metal-oxide-semiconductor field-effect transistors (MOSFETs) are densely manufactured on monolithic pieces of silicon material. Driven by the miniaturization of these transistors, the number of MOSFETs on an IC of the same size increases exponentially over time as described by the Moore’s Law [2]. This technology scaling of transistor size results in circuits with largely reduced form factors, power consumption, and manufacturing costs in combination with greatly improved performance [1] compared to those constructed of discrete electronic components. The CMOS technology not only revolutionizes the electronics industry but also has a transformative impact on society.

Such great technological advancements of modern electronics have led to the continuous innovations in medical devices specifically designed for healthcare and biomedical applications [3]. These devices can provide the surveillance of health status, the assistance and augmentation of physiological functions, and the mitigation and treatment of diseases [4]. Historically, most of the medical devices, implemented with discrete components and connected to the body by many electrical lead wires and cables, have been large-sized, inconvenient to use, and expensive to produce [5]. However, the advanced CMOS technology can realize the same functionality in tiny ICs with much smaller footprints. These CMOS ICs enables the development of miniaturized, integrated, and sophisticated medical devices with high performance and low cost for various medical needs.

## 1.1 Implantable medical devices (IMDs)

Medical devices are either noninvasive or invasive depending on whether intrusion or penetration of the human body is involved. A noninvasive device does not violate the integrity of the body and can be used without cutting or puncturing the skin [3]. On the other hand, an invasive device requires the insertion into the targeted part of the body by medical procedures [3], either through a cut in the skin or through a natural orifice [6].

Implantable medical devices (IMDs) form a major class of invasive devices. They can be embedded or inserted in the interior body parts to perform *in-vivo*, *in-situ* monitoring, enhancement, and manipulation of physiological activities in the anticipated manner [7]. They are of particular interests in situations where conventional medications and surgical interventions have produced unsatisfactory response for certain diseases, or accurate and continuous monitoring of physiological parameters inaccessible from outside of the body is needed.

IMDs find wide applications in both the diagnostic and therapeutic procedures,

including measuring vital biological signals to keep surveillance over the physiological state of an individual, overcoming various diseases from neurological disorders to heart failures, and delivering controlled amount of drugs to the targeted sites precisely [3]. A variety of IMDs can be deployed in various body parts to provide essential structural and functional support and restoration as well as physiological monitoring, as illustrated in Figure 1.1 (adapted from [7]). Some notable examples include cardiac pacemakers to control abnormal heartbeats [8], cochlear implants to recover hearing loss [9], implantable neurostimulators to treat neurodegenerative dis-

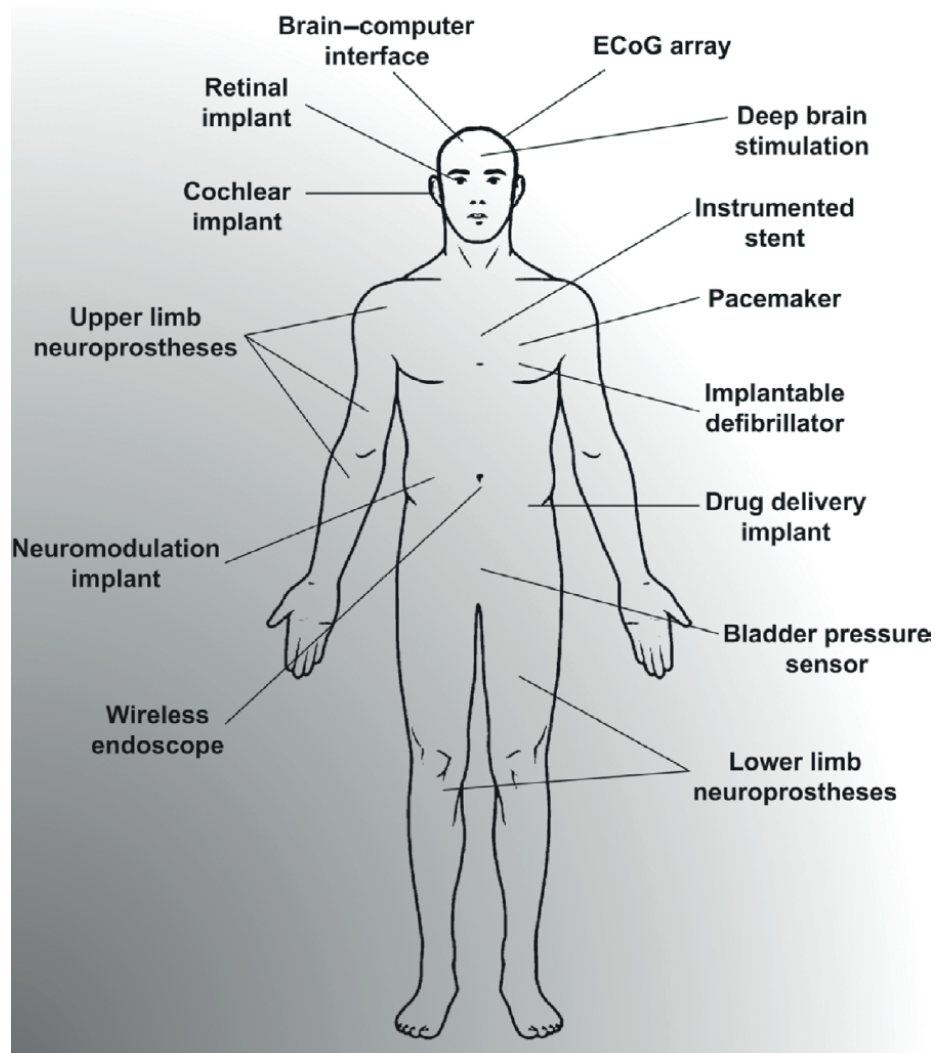


Figure 1.1: Common examples of IMDs implanted at various parts of the interior body for sensing and actuation.

eases [10], subcutaneous sensing systems to continuously monitor blood glucose [11], and deep organ sensors to monitor bladder pressure [12]. These IMDs are making broad scientific and translational impact and improving the quality of life for millions of people [7].

This thesis focuses on IMDs for measuring vital physiological signals in sensing abnormal variations to inform the health status of the human body. Specifically, a novel, micron-scale sensing device the size of a grain of sand is presented for *in vivo* physiological monitoring. This device, referred to as a sensing mote, achieves such aggressive miniaturization by integrating all the functionality monolithically in a custom CMOS sensing IC and enables new applications unachievable with larger devices.

## 1.2 Thesis outline

Chapter 2 provides the background information related to this work, mainly including physiological signal monitoring and design considerations of IMDs for such monitoring applications.

Chapter 3 describes the design approaches for the proposed sensing motes and the testing procedures to verify their electrical functionality.

Chapter 4 introduces the microfabrication techniques enabling these micron-scale, fully-integrated sensing motes.

Chapter 5 presents the experimental results of characterizing these integrated sensing motes. The *in vitro* validation of the sensing performance of the motes using chicken tissues as well as the *in vivo* evaluation with laboratory mice are discussed.

Chapter 6 concludes this work with a summary of the original contributions to the fields of miniaturized implantable sensing systems. Future improvements and potential extension for this work are also considered.

---

## Chapter 2

# Background

---

### 2.1 Introduction

Physiological signals are vital signs of human health. Some common examples are temperature, oxygen, nitrogen, glucose, pH, lactate, electrolytes ( $\text{Ca}^{2+}$ ,  $\text{Mg}^{2+}$ ,  $\text{K}^{+}$ ,  $\text{Na}^{+}$ , etc.), inflammatory cytokines, and innate biological markers like lysozyme and lactoferrin [4]. Continuous monitoring of these physiological parameters is crucial for managing personal healthcare by early detection of health issues [4] and has been of great interests to health practitioners and professionals for a long time. Such monitoring can predict, diagnose, and prevent serious diseases, such as hypertension, diabetes, cancers, cardiovascular diseases, neural disorders, stroke, chronic pain, and obesity.

Conventionally, physiological signals are measured using bulky, expensive equipment or through tedious, inconvenient procedures. Consider the case of measuring

blood pressure as an indicator for hypertension. A sphygmomanometer machine is usually used, which keeps the arm of a subject inside the inflatable cuff for taking measurements and limits the mobility and movement of the subject. Another example is the glucose measurements for patients with diabetes. Typically, the blood samples have to be acquired at regular intervals to examine the glucose concentration. Both types of measurements are inconvenient and impractical to perform continuously on a daily basis [3].

More effective and convenient monitoring can be achieved by using IMDs (also referred to as implants) equipped with suitable sensors for the specific physiological signals of interests; these sensors convert the biological signals into electrical signals, which are processed and transmitted to the outside world. Such implants can acquire accurate, real-time, and clinically-relevant physiological conditions by performing *in vivo* sensing directly at the target locations, allowing necessary interventions or therapies to be deployed at the onset of abnormal events [4, 13]. As a result, IMDs gain increasing popularity for both the transient and long-term monitoring of physiological parameters under acute or chronic scenarios. In the earlier examples of blood pressure and glucose measurements, implantable blood pressure sensors [14, 15] and implanted glucose monitors [3, 16] have been developed to enable continuous monitoring for these signals in a more potent and viable way.

## 2.2 Physiological temperature monitoring

Among the various physiological parameters, temperature is an important indicator of human health, tissue pathology, diseases progression, and thermal effects arising from particular medical procedures. Therefore, accurate and continuous monitoring of physiological temperature is important for many biomedical applications ranging from the diagnosis and therapeutics in clinical settings to the basic scientific research. Three of the major applications include: (1) daily routine monitoring of core

body temperature; (2) temperature evaluation during therapeutic procedures involving thermal treatments, such as hyperthermia therapy and tissue ablation; (3) temperature monitoring during ultrasound-evoked neuromodulation procedures. These applications will be elaborated in the following paragraphs.

### **2.2.1 Monitoring of core body temperature**

Core body temperature plays a critical role in many biological processes, including the regulation of metabolism and homeostasis. It is the temperature of the body's core, consisting of deep tissues, internal organs and the cerebrum. It is normally controlled through thermoregulation and indicates the body's state of health [17]. Although temperatures in the peripheral regions of the body and extremities vary depending upon environmental conditions, the core body temperature remains practically constant at 37 °C under normal conditions. Deviation of more than 1 °C from the normal level is usually associated with loss of thermoregulation and medical complications [18].

Therefore, monitoring of core body temperature is crucial for many medical diagnoses and finds wide applications in daily routine monitoring and clinical settings for pre-operative or post-operative patient monitoring. Conventional approaches for core temperature monitoring include the inconvenient rectal and esophageal probes [17–21], which are invasive and can cause subject discomfort and irritation at the probe insertion sites.

There are also commercially-available temperature sensors in the form of ingestible capsules [17, 20, 22] that record temperature as they travel through the digestive tract. However, these sensors, including CorTemp (CorTemp HQ Inc.) and VitalSense (Mini Mitter Co., Inc.), contain biohazardous batteries and present relatively large sizes and weights (sizes of  $>20\text{ mm} \times 8\text{ mm}$  and weights of  $>1.7\text{ g}$  [20]), causing unnecessary burdens and discomfort to subjects.

### 2.2.2 Monitoring for therapeutic procedures

In addition to measuring core body temperature, there are various biomedical needs for more localized temperature monitoring for therapeutic purposes, such as the hyperthermia treatment to eliminate tumors [23, 24] and tissue ablation applications with high-intensity focused ultrasound [25]. By raising the temperature of tumor-loaded tissues to 40–43°C, these procedure can be applied as adjunctive therapies with various established cancer treatments such as radiotherapy and chemotherapy [24].

For such thermal-related procedures, accurate real-time mapping of induced temperature elevation distributions in tissues at treatment sites is needed for consistent and proper thermal treatment by controlling the amount of applied energy to achieve the desired therapeutic effects while avoiding tissue damage [26]. Without temperature mapping, the adequacy of the treatments can not be assured.

A common approach to such temperature monitoring is the use of implanted thermal probes placed interstitially within thin plastic catheters in the treatment site [24, 27, 28]. In addition, magnetic resonance imaging (MRI) can also be used for measuring temperature by the detection of changes in the water proton resonant frequency [29]. However, its high cost, low availability, lack of portability, and long treatment times have limited its applicability to only a handful of applications [30].

### 2.2.3 Monitoring for ultrasound neuromodulation

Temperature also plays a key role in neuromodulation procedures. Neuromodulation is the process of inhibition, modification, regulation or therapeutic alteration of nerve activity, electrically or chemically, through targeted delivery of a stimulus to the central (CNS) and peripheral nervous systems (PNS).

While the mechanisms are not yet completely understood, neuromodulation through focused ultrasound (FUS) stimulation has been emerging as a way of achieving both



high spatial resolution (sub-millimeter) and high depths of penetration (several centimeter) while remaining noninvasive, which can potentially provide surgery-free therapeutics. Studies have shown ultrasound-evoked neuronal activity in mice with pressure ranges in the few MPa [31], hundreds of kPa [32, 33] and even below 100 kPa [34]. The human primary visual cortex has also been excited with pressures in the MPa range [35].

Ultrasound can have both the thermal and mechanical effects to the nervous systems. Being able to understand how these effects collaboratively lead to desired modulation effects is crucial to fully understand the mechanisms of FUS-based modulation scheme and develop effective therapeutics. For this reason, it is necessary to acquire the temperature variations during these procedures accurately. Similarly, these applications also conventionally use external probes for temperature measurements [36].

All the three categories of applications can benefit from replacing external temperature probes or expensive tools like MRI machines with miniaturized, CMOS-based implantable sensing motes. The design considerations of such a sensing mote is presented as follows.

## 2.3 Design considerations of IMDs

The development of advanced IMDs for physiological monitoring involves the careful considerations of multiple design principles and many application-specific requirements. These include power sources and power densities to provide energy to the implants, sensing modalities, power consumption and the sensing performance of the interfacing electronics, total device size and weight, placement method and location, biocompatibility and safety of implantation, and robust operation for chronic *in vivo* deployment [7]. These design aspects, sometimes presenting extremely tight constraints and even conflicts, will be discussed in detail in the following sections.

### 2.3.1 Power sources

There are many approaches to provide energy to IMDs. The most intuitive, though most inconvenient and invasive, way to power an implant is by connecting a wire passing from an external power supply percutaneously (across the skin of a subject) to the implant. It impairs the mobility and freedom of the subject. The tethered subject feels uncomfortable and is tied up due to restrictions on movements [3]. In addition, such wired device poses serious problems of infection and irritation associated with wires going through skin and tissues, unsafe for both the subject and the implant.

Another common approach to power up implants is by using batteries. However, batteries can only power these implants for a fixed lifetime [37, 38], and, once depleted, require surgical interventions to replace them each time [39, 40]. They also take up large volumes of the space-limited implants, burden the subjects with extra weights, incur high replacement costs, and can be incompatible with or even harmful to the biological environment.

To overcome these limitations, wireless power transfer (WPT) has been developed as a viable technique to power up IMDs across the skin without any direct electrical contact between the energy sources and the IMDs [7], eliminating the needs for the cumbersome and invasive wires or the bulky and biohazardous batteries [40]. Getting rid of the wires removes the rigid attachment points, the associated risk of infection [3, 41], and the restraining parameters for the monitored subject [5], allowing safe monitoring during any activity, while the absence of the batteries greatly reduces the overall dimensions as well as the implementation and maintenance costs of these implants [42]. Although possibly less efficient than wires and batteries due to the energy loss in the intervening tissue medium [3], WPT enables the development of compact, untethered, and safe implants with long-term, sustainable, and seamless operation [41, 43, 44].

WPT has been widely adopted across the breadth of the biomedical field as well

as consumer electronics with various levels of power requirements from nanowatts (nW) in wireless sensors and radio-frequency identification (RFID) tags, milliwatts (mW) in near-field communication (NFC), watts in mobile electronics, and kilowatts in electric vehicles. Figure 2.1 shows some of the state-of-the-art WPT applications (adapted from [7]).

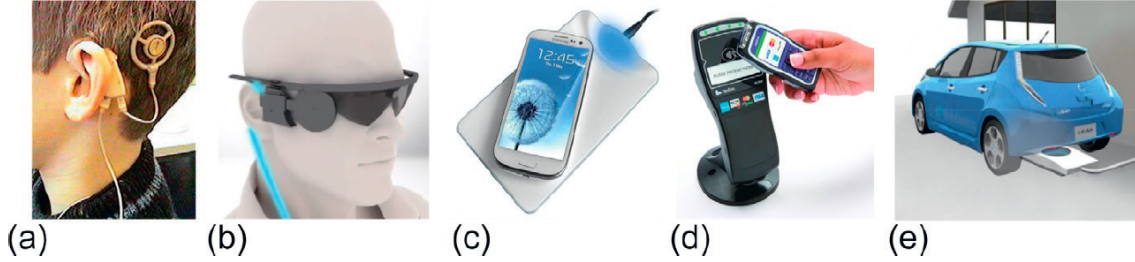


Figure 2.1: State-of-the-art applications for wireless power transfer. (a) A cochlear implant; (b) a visual prosthesis; (c) a mobile phone charger; (d) an NFC device; (e) an wirelessly-charged electric vehicle.

There are mainly three types of wireless energy sources: light energy, radio-frequency (RF) energy, and ultrasound energy. RF energy and light both rely on the propagation of electromagnetic (EM) waves. RF signals are defined between 30 kHz and 300 GHz, whereas light ranges from far infrared ( $10^{12}$  Hz) to ultraviolet ( $10^{17}$  Hz) [5]. Ultrasound is a mechanical pressure wave (sound wave) with a frequency above the range of audible frequencies for humans ( $>20$  kHz). Besides being able to provide power to implants for indefinite periods, these wireless sources can also carry information, including the commands from the external sources and data acquired by the implants, to enable bi-directional communication between the implants and the sources.

The ability to scale the size of a wireless device is limited by the wavelength of the energy used for powering and communication while the implantation depth is limited by absorption and scattering of this energy in tissue. These characteristics of the three wireless sources will be separately discussed in the sections that follow.

## Light

Light can be generated by light-emitting diodes or lasers and received by light emitting and sensitive devices like photodiodes or phototransistors. It offers the shortest wavelengths (sub- $\mu\text{m}$ ), enabling the smallest devices. In addition, optical wave communication, using light as the carrier, is immune to EM interference and can offer high available bandwidth due to a high operating frequency, allowing high data rates [5], although physiological temperature is usually a slowly-varying parameter that has a relaxed requirement on data rate.

However, light has very limited penetration depths (typically  $<1\text{ mm}$ ) [45] due to its reflection and dispersion at the skin interface between the transmitter and receiver, which causes a huge attenuation. It is, therefore, limited mostly to transcutaneous applications requiring high-speed communication.

## Radio-frequency (RF)

Radio-frequency (RF) energy uses antennas to transmit and receiver the propagated EM waves for powering and communication. Antenna design is thus one of the most important aspects for RF-based IMDs, not only due to dimension constraints but also the effective radiated power within safety limits, which is only  $10\text{-}100\text{ }\mu\text{W}/\text{mm}^2$  [46, 47].

Due to a high speed of light, the wavelength of RF energy is at the centimeter-scale even in the GHz regime, requiring large, centimeter-scale antennas for efficient power delivery [39, 48]. If the antenna size is reduced to millimeter- or sub-millimeter scales to enable smaller implants, the power harvesting efficiency will be greatly impaired [49, 50], which leads to a much higher radiated power for device operation.

In addition, at these frequencies, RF signals get heavily attenuated as they propagate through the human body because of an exponential increase in signal attenuation as the operating frequency increases, which severely limits penetration depths.

## Ultrasound

Alternatively, ultrasound energy has recently been shown as a novel, promising approach to enable small implants with large implantation depths [43]. Ultrasound uses the piezoelectric property found in some materials to convert acoustic energy into electrical energy or vice versa. As such, piezoelectric transducers replace the antennas employed in the RF-based devices. For the external transmitter, its transducer converts electrical energy into acoustic energy that is transmitted and harvested by the transducer of the receiving implant, where the inverse process takes place and the acoustic energy is transformed back to electrical energy. Ultrasound has a power transfer efficiency higher than that of RF links and it does not suffer from EM interference either inside or outside the human body [4].

The widely-used diagnostic ultrasound employs a frequency ranging from 1 MHz to 15 MHz [51]. Particularly, ultrasound in the sub-10-MHz regime offers the best trade-offs between device size and penetration depth [43, 52, 53], allowing for sizes on the order of 200-300  $\mu\text{m}$  with centimeters of penetration thanks to the low tissue attenuation of 0.5-1 dB/cm/MHz [54]. Ultrasound also offers a much higher safe exposure intensity limit in tissue, 7.2 mW/mm<sup>2</sup> [55], compared to that of RF energy, and is widely used as a safe and noninvasive medical imaging modality. We, therefore, chose ultrasound for powering the motes developed here and for transmitting the acquired temperature data. The use of ultrasound also allows these motes to be identified with imaging, providing biogeographical information in vivo.

### 2.3.2 Power consumption

In case of battery-powered IMDs, low power consumption is of paramount importance to ensure long-term function of the implants and patient safety. In practice, the operational longevity of the implants is typically dictated by the time between battery replacements.

Although this is less of a problem for wirelessly-powered devices, it is imperative to keep the power consumption low to limit heat generation of the implants and enable reliable power delivery [3, 11]. This also ensures that the requisite power level of the wireless sources complies with the governmental regulations on the exposure limits for human body [5]. Tight power budgets call for efficient power-harvesting front-end circuitry, low-power sensing modules, as well as power-saving data transmission schemes for these wireless implants.

### **2.3.3 Sensing performance**

A sensor with high performance is critical in detecting and interpreting the events or changes in the variable of interests accurately and reliably. Particularly, for physiological monitoring, the quality of the outcomes of the sensing electronics directly impacts diagnosis and informs medical decisions.

Temperature sensors involve the careful examinations of multiple design metrics, including temperature range that the sensor can accurately interpret, resolution (the smallest detectable temperature change), accuracy (the different between the actual temperatures and the sensor outputs), calibration type (the number of points required to calibrate the sensor for accurate readings), power consumption of the sensing electronics, and supply voltage at which the sensor is operated.

In healthcare applications, temperature sensors typically requires a smaller temperature range (35 to 50°C), higher resolution (0.1 °C) [56], and higher accuracy ( 0.1 °C) [57] than in general applications. Maintaining a high sensing performance while keeping the power consumption low is the key driver for reliable implants.

### **2.3.4 Biocompatibility**

One of the most important characteristics of IMDs is biocompatibility, defined as being nontoxic, inactive, and bioinert. A biocompatible IMD must not cause irrita-

tion to the surrounding tissues and any other long-term harmful effect to the host body [7]. Specifically, biocompatibility presents the following five properties: non-toxicity (not toxic to cells), non-genotoxicity (not toxic to genetic information within cells), non-mutagenicity (not causing damage to the genetic material, usually DNA), non-carcinogenicity (not causing cancer), and non-immunogenicity (not inducing the immune response) [58]. The two major strategies to improve biocompatibility for IMDs include system miniaturization and biocompatible packaging, separately discussed as follows.

### **2.3.5 System miniaturization**

As invasive devices, IMDs can present acute and chronic biological response that imposes negative effects on health and neuronal function, such as tissue strain, loss of perfusion, inflammation, and foreign body rejection [4]. The invasive procedures to implant these devices often causes discomfort, long recovery time, and post-surgery traumas and infections [59, 60]. An effective approach to minimize these adverse effects is to aggressively reduce the overall size of the IMDs to millimeter-scale or even micron-scale.

The advantages of system miniaturization are manifold: (1) small devices can be conveniently implanted through minimally invasive surgeries or even injected through syringes [59, 60], avoiding the trauma and infection associated with more invasive procedures; (2) miniaturized devices reduce foreign body rejection and tissue damage, and improve biocompatibility and chronic viability [11, 61, 62]; (3) the small size allows devices to be placed in limited interstitial spaces and enables new monitoring applications and treatment procedures [39, 43, 61]; (4) miniaturization allows for more direct interactions with biological environment at the cellular and sub-cellular levels [39, 63]; (5) the small size increases the safety and lifetime of devices [60, 64]; (6) miniaturized devices interfere less with the physical functions to be monitored

[5] and introduce low mechanical mismatch. It is, therefore, essential to reduce the overall sizes of IMDs.

The needs for miniaturization lead to custom designed CMOS ICs (also referred to as chips) that integrate the desired functions on tiny silicon dies [5]. Most components in IMDs, including electrodes, amplifiers, oscillators, memory, and wireless communication systems, can be implemented with ICs [39] thanks to the advances of CMOS technology as governed by the Moore’s Law. As a result, the dimensions and weights of IMDs have been reduced from centimeter to millimeter and from ounces to fractions of a gram, respectively [7]. In addition, the elimination of bulky batteries and wired interfaces through wireless powering and communication has also reduced the sizes of IMDs [59, 60].

In addition, system miniaturization for IMDs can be further achieved through heterogeneous integration of CMOS ICs and other components into a compact system, denoted as the “More-than-Moore” strategy [65]. It is a recent trend that augments IC functionality by integrating components or devices that can offer additional capabilities, such as sensors or actuators to interact with the outside world and energy sources for powering the device [66].

For implants that use ultrasound as the power and communication medium, the piezoelectric transducers usually dominate the device volumes. Reducing the transducer size down to the order of hundreds of  $\mu\text{m}$  reduces the overall device size. To effectively interface with these micron-scale piezoelectric transducers and achieve the smallest overall volume for these motes, we employed “chip-as-system” integration [67] by directly integrating the transducers with CMOS ICs. Such a far-back-end-of-the-line integration approach allows these motes to be viewed as “More-than-Moore” enhancements to CMOS [65, 66].



### 2.3.6 Biocompatible packaging

Packaging refers to the process of applying a biocompatible package to house all the components of an IMD into an enclosed system for reliable implantation. The human body is an intricate and delicate living system that may be harmed by some components of the implanted IMD. Meanwhile, the conductive bodily fluids of the body contain many chemical and biochemical species that can affect the performance of the implant [68]. As the outmost layer of the implant, the package directly interfaces with the body; it needs to isolate the implant from the corrosive bodily fluids while protecting the body from any harmful material within the implant [7]. With appropriate packaging, the implant is able to perform the desired function without producing any adverse effect [58].

Besides biocompatibility, the packaging materials need to be robust, lightweight, low-cost, and water-tight. They should present minimal influences on the sensing/actuation functionality and wireless power transfer and data transmission for the implants. Therefore, polymeric materials, such as polyimide (PI), poly(p-xylylene) (parylene), polyether ether ketone (PEEK), polydimethylsiloxane (PDMS), and liquid crystal polymer (LCP), have emerged as alternatives to the conventional ceramic and metal packages like aluminum oxide and titanium, respectively [58]. Polymers have high resistance to biological reactions, low densities and small volumes, low costs, high mechanical flexibility, and easy molding and processing [3]. They can be conveniently deposited as thin films with a variety of techniques and can take any shape as conformal coatings for implants, enabling the fabrication of miniaturized devices for various medical applications [7].

Among these polymer materials, we chose parylene as the encapsulation layer for the proposed motes. Parylene serves as a common protective coating for biomedical devices, such as stents, pacemakers, and neural interfaces [69]. It is a nontoxic, bioinert, and biocompatible material (currently qualified as a Class VI polymer by

the Food and Drug Administration [70]). In addition, it is chemically and biologically stable, mechanically flexible (Young’s modulus  $\sim 4$  GPa), and CMOS-compatible and allows room-temperature, pinhole-free deposition with conformal coverage [58, 71]. Parylene shows unique barrier properties from both the electrical and the chemical perspectives. On one hand, its satisfactory dielectric performance (a low dielectric constant of  $\sim 2.95$  at 1 MHz and high resistivity of  $\sim 8.8 \times 10^{16} \Omega\text{m}$ ) makes it a good dielectric barrier and allows very low leakage current [58, 69, 71]; on the other hand, its unique moisture barrier properties with low water vapor and oxygen permeability [7, 58] can isolate the integrated chips from bodily fluids.

## 2.4 Focus of this thesis

In light of these design criteria, this thesis makes efforts to address the emerging needs for the next-generation implants that are miniaturized, integrated, and wireless with a low power consumption and high sensing performance for long-term, reliable *in vivo* physiological sensing.

Particularly, a micron-scale, ultrasonic wireless sensing mote for continuous *in vivo* temperature monitoring is presented. The mote holds linear dimensions of  $380 \mu\text{m} \times 300 \mu\text{m} \times 570 \mu\text{m}$ , resulting in a total displaced volume of  $0.065 \text{ mm}^3$  and a mass of only 0.3 mg, orders of magnitude smaller and lighter than the commercial sensing capsules, while consuming only 0.813 nW of power at 37 °C. It achieves such extreme miniaturization through the monolithic integration of a custom low-power CMOS temperature sensor chip with a micron-scale piezoelectric transducer; specifically, the transducer is directly fabricated on the top surface of the CMOS chip containing all the interfacing electronics [72]. This allows these motes to be implanted using minimally-invasive procedures or even injected using a syringe with improved bio-compatibility and reduced foreign body response and offers new approaches for localized *in vivo* monitoring of spatially-fine-grained temperature distributions.

---

## Chapter 3

# Design of a Temperature Sensing Mote

---

### 3.1 Introduction

The temperature sensing mote contains a custom sensor chip implemented in a 180-nm CMOS technology and a single piezoelectric transducer integrated on top of the chip without any other interfacing electronics or bonding wires (as found in larger millimeter-sized sensing systems [39, 45, 52, 59, 73–75]). An external ultrasound probe transmits ultrasound energy to the mote, which is converted by the integrated transducer into electrical energy to wirelessly power the chip. The chip modulates temperature information on the reflected ultrasound echoes returning to the external ultrasound probe through acoustic backscattering [74–77], thus allowing both wireless

power and data transmission. There exist other methods for communication, such as the utilization of a dedicated piezoelectric transducer driven by a transmitter [78] or the employment of an RF coil antenna [52]. These require additional circuit blocks that cost power and area, not feasible for the miniaturized sub-0.1-mm<sup>3</sup> mote described here.

Figure 3.1 shows the system architecture and block diagram of the mote. The embedded sensor chip in the mote contains a front-end block to convert the incoming AC signals from the on-chip transducer into a stable DC supply for the rest of the chip, a temperature-sensing block to perform temperature measurements, and a modulation block to transfer the temperature information back to the ultrasound source by actively modifying the input impedance of the integrated piezoelectric transducer (piezo). We used a commercial linear-array ultrasound probe, L12-3v (Verasonics, Inc.), coupled with a programmable and configurable ultrasound transceiver array, the Vantage 256 system (Verasonics, Inc.), to perform ultrasound energy transmission and data acquisition and analysis through a MATLAB (The MathWorks, Inc.) interface. The Vantage system can be programmed to generate ultrasound at a specific frequency with the desired waveform (including pulse duration and pulse repetition period), beam profile (including focal depth and steering angle), and output power level through the L12-3v probe. Pulsed ultrasound with an ultra-low duty cycle of

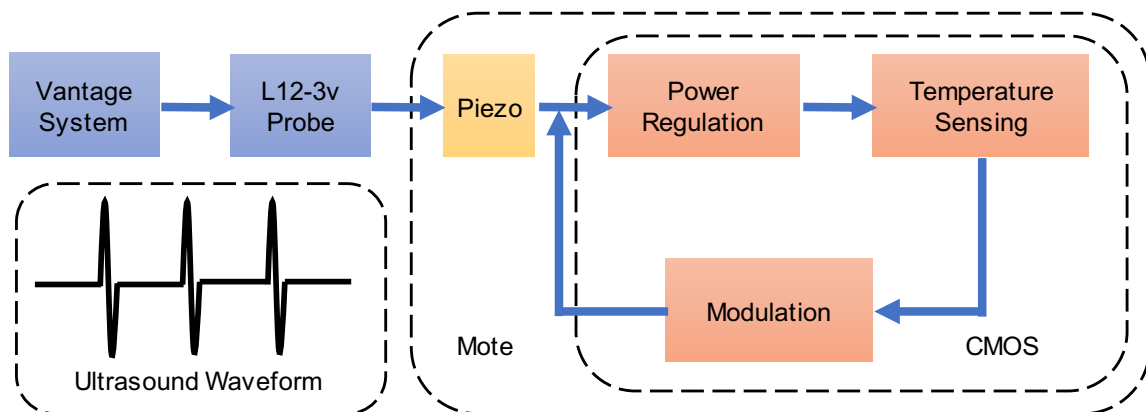


Figure 3.1: The system diagram demonstrating the operating principles of the mote.

<0.5% is used for receiving the acoustic backscattering data. After transmitting each pulse to the mote, the ultrasound system receives the reflected echoes and extracts the temperature information modulated on the echoes during the idle time in which there is no ultrasound transmission until the next pulse is transmitted, enabling continuous real-time acquisition of temperature data with repeated pulses. This imposes strict requirements on the power harvesting and energy storage components of the mote to maintain proper circuit functionality even without input power, which will be addressed in Section 3.3.

With an extremely compact and lightweight form factor, a number of these motes can be injected into animals to perform localized *in vivo* real-time monitoring of the core body temperature or continuous acquisition of temperature distributions during thermal-related procedures with the biogeographical location of the mote contained in the ultrasound image. Figure 3.2 illustrates how multiple motes can be used for mapping physiological temperature inside animal tissues.

The design of such a sensing mote involves the coordinated design of the CMOS chip and the piezoelectric transducer that interfaces with the chip, both of which will be respectively addressed in Section 3.2 and Section 3.3.

## 3.2 Characterization of piezoelectric materials

Piezoelectric materials have unique properties that allow them to convert electrical energy into mechanical energy and, for that reason, have been utilized for decades as ultrasound transducers in medical imaging. These same materials can also be used to harvest energy from ultrasound waves to power implants and transmit data by modulating information onto an ultrasound carrier. For this reason, they were used as the transducers for the proposed sensing motes.

Piezoelectricity can be introduced to some materials by poling, a procedure of applying high electrical field at elevated temperature [79], which orients the polar

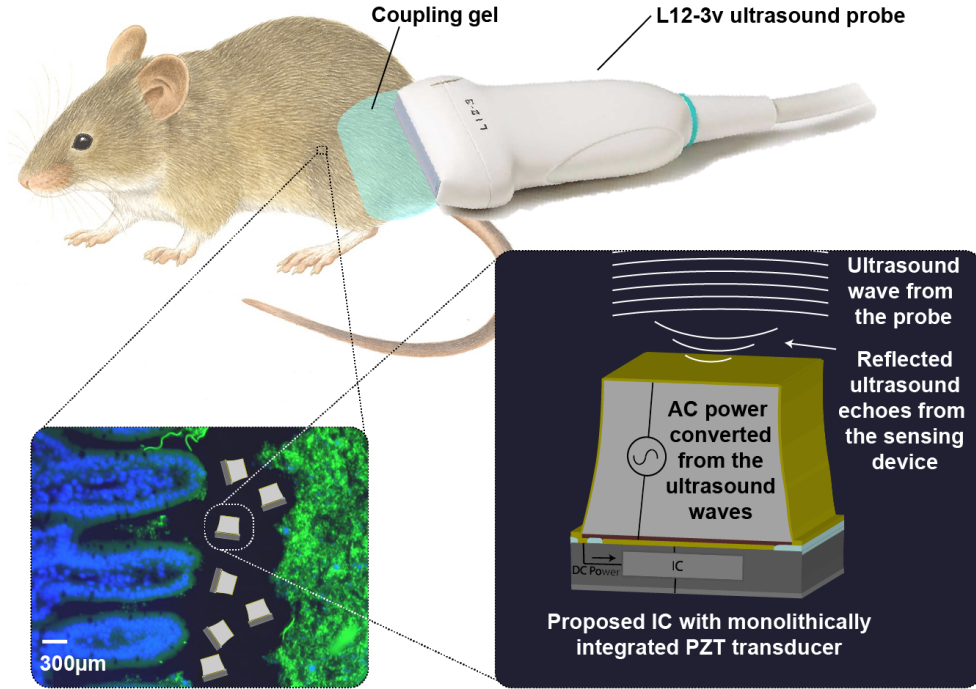


Figure 3.2: Conceptual figure illustrating the proposed motes with integrated piezoelectric transducers performing *in vivo* temperature monitoring.

domains of the materials in the direction of the external electrical field [80]. These materials now exhibit macroscopic piezoelectricity. They physically deform in the presence of an electric field, or conversely, produce an electrical charge when mechanically deformed. Specifically, if a voltage is applied in the same direction as the dipoles (the direction of the poling electric field) in a piezoelectric material, the material elongates in that direction. On the other hand, the change in volume due to mechanical stress exerted on the material along the direction of the dipoles cause the surface charges to be separated across the material, which is a dielectric [80]. This charge separation creates a voltage across the material under open circuit conditions or gives rise to a current flow under closed circuit conditions [81].

There are inorganic and organic piezoelectric materials. Inorganic ones include lead zirconate titanate (PZT), aluminum nitride (AlN), zinc oxide (ZnO), barium titanate (BaTiO<sub>3</sub>), lithium niobate (LiNbO<sub>3</sub>), and quartz. They are rigid and bio-

compatible or can be made biocompatible after being properly encapsulated. Organic materials, including polar polymers like polyvinylidene difluoride (PVDF), are flexible and biocompatible. Implants made of piezoelectric polymers are less expensive in terms of material cost and processing. However, when compared to inorganic piezoelectric materials, an organic piezoelectric material often shows more inferior piezoelectric properties [82].

The piezoelectric activity of a material can be characterized using the electromechanical coupling coefficient, a numerical measure of the conversion efficiency between electrical and mechanical energy [81]. A coupling coefficient of 1 implies perfect coupling between the mechanical and electrical domains [83]. In addition, for power-harvesting applications, the piezoelectric coefficient  $d_{33}$ , which relates the charge developed on the film surface to the stress exerted on the material, is of particular interests. A higher  $d_{33}$  is always preferable as it indicates more charges generated and more energy harvested by the material given the same mechanical stress, or the same input pressure in terms of an ultrasound source.

Two major piezoelectric materials, PVDF and PZT, were considered in this thesis. Their properties, electrical models, and impedance measurements will be discussed in Section 3.2.1 and Section 3.2.2, respectively.

### 3.2.1 Polyvinylidene difluoride (PVDF)

PVDF is a flexible, biocompatible, semi-crystalline fluoropolymer in the form of thin films [63, 84]. Its unique piezoelectric properties after poling was first discovered by Kawai [85]. Compared to other piezoelectric materials such as PZT, PVDF suffers from relatively poor dielectric and electromechanical coupling properties [86, 87]. Nevertheless, it is widely used in ultrasound imaging and power harvesting applications due to its advantages of high voltage sensitivity that can provide a higher output voltage than other materials for the same pressure input, low acoustic impedance

comparable to that of water and biological tissues, high compliance and toughness, mechanical durability and chemical resistance, flexibility that conforms to nonuniform surfaces, and availability in large area sheets [86, 88, 89].

PVDF is synthesized by addition polymerization of the  $\text{CH}_2=\text{CF}_2$  monomer, and exhibits  $\alpha$ ,  $\beta$ ,  $\gamma$ , and  $\delta$  phases. Among the four phases, the  $\alpha$  phase is not piezoelectric, while the  $\gamma$  and  $\delta$  phases are uncommon. The  $\beta$  phase form, however, has a net dipole moment pointing from the fluorine to the hydrogen and therefore exhibits the largest effective dipole moments, resulting in piezoelectricity in the PVDF polymer [90].

The electrical model of PVDF is shown in Figure 3.3.  $C_O$  and  $R_O$  represent the parallel-plate capacitance and the dielectric loss resistance of the transducer, respectively. The series equivalent resistance-inductance-capacitance (RLC) resonant branch of  $R_S$ ,  $L_S$  and  $C_S$  captures the mechanical behavior and models the electrical equivalent of the mechanical resonance [91, 92].

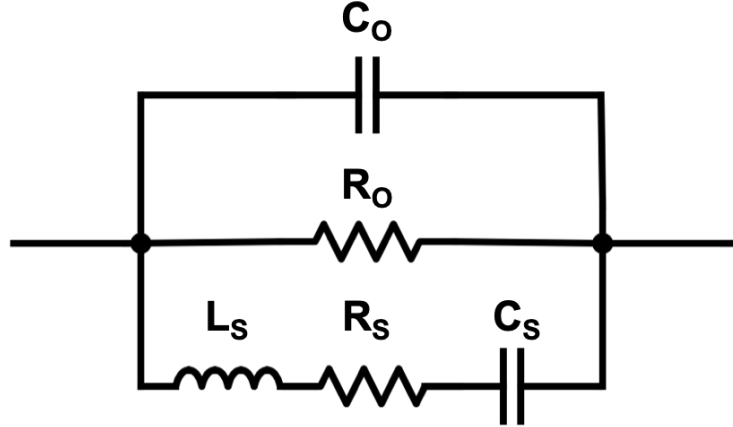


Figure 3.3: The electrical model of PVDF.

The impedance measurements of seven PVDF pieces with varying sizes from 2.4 mm  $\times$  2.4 mm to 16.1 mm  $\times$  16.4 mm were performed with a network analyzer (N5230A, Keysight Technologies Inc.) from 1 MHz to 100 MHz. This study employed commercially-available, uniaxially-oriented, and pre-poled PVDF (Measurement Specialties) sheet with a thickness of 33  $\mu\text{m}$ . The film thickness was confirmed with a



stylus profiler (Dektak-XT, Bruker).

The measured impedance across frequency in the form of  $S_{11}$  parameter was converted to  $Z_{11}$  parameter, from which the values of  $C_O$ ,  $R_O$ ,  $L_S$ ,  $R_S$ , and  $C_S$  can be extracted as proposed in [86]. The component values of the electrical model derived from the measured impedance at a frequency of 7.8125 MHz for all the seven samples are summarized in Table 3.1.

Table 3.1: Derived component values of different sizes of PVDF.

Size (mm)	$C_O$ (pF)	$R_O$ ( $\Omega$ )	$L_S$ ( $\mu\text{H}$ )	$R_S$ ( $\Omega$ )	$C_S$ (pF)
$2.4 \times 2.4$	10.16	8568.82	284.12	5276.03	0.08
$2.4 \times 4.5$	17.62	4584.16	159.69	3082.58	0.14
$4.3 \times 4.4$	32.33	2526.74	74.50	1495.79	0.30
$4.4 \times 8.2$	59.69	1357.03	39.80	766.01	0.55
$7.9 \times 8.5$	111.29	735.89	20.44	391.53	1.07
$8.7 \times 16.2$	229.41	356.92	9.62	182.91	2.28
$16.1 \times 16.4$	416.45	197.57	5.15	95.58	4.35

The comparison of the measured impedance and the modeled impedance for the 2.4-mm-by-2.4-mm piece is shown in Figure 3.4, indicating that these extracted values match well with the actual impedance of PVDF.

Furthermore, it is noted that component values scale either proportionally or reversely with the area of the film (Figure 3.5). Among the five components,  $C_O$  and  $C_S$  scale linearly with film area, while  $R_O$ ,  $L_S$ ,  $R_S$  are reversely related to area. With area scaling, the magnitude of the input impedance scales down linearly as area goes up, and the phase stays the same.

### 3.2.2 Lead zirconate titanate (PZT)

PZT is a piezoelectric ceramic material that exhibits superior piezoelectric properties. The type of PZT used in this work is PZT-5H, which has a high electromechanical coupling coefficient of  $\sim 0.75$  and a satisfactory  $d_{33}$  value of  $\sim 650$  pC/N [93].

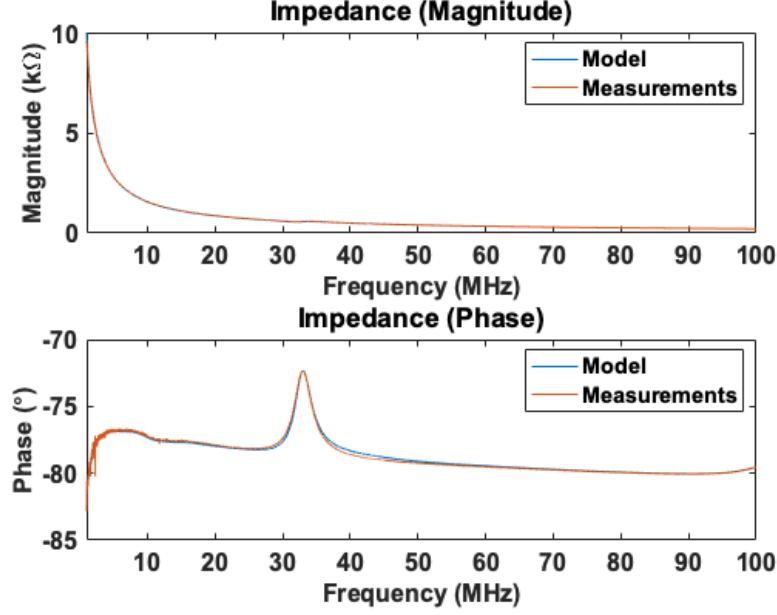


Figure 3.4: The modeled impedance in comparison with the measured impedance for a 2.4-mm-by-2.4-mm piece of PVDF.

It can be electrically modelled as a parallel-plate capacitor along with a series RLC branch representing the mechanical resonance of PZT [94], as depicted in Figure 3.6. Due to the great dielectric properties of PZT, the dielectric loss resistance present in the model of PVDF is eliminated here in the model of PZT.

A piece of commercially-available, pre-poled 267- $\mu\text{m}$ -thick PZT bulk material (Piezo Systems, Inc.) was diced into smaller samples with widths ranging from 1 mm to 4 mm using a dicing saw (DAD3220, Disco). Their impedances were acquired from 6 MHz to 10 MHz with the network analyzer. In order to simulate the acoustic load to the PZT when implanted, the measurements were performed by immersing the PZT piece into deionized (DI) water as the ultrasound transmission medium with an acoustic impedance close to that of biological tissues. The values of the electrical components in the PZT model (Figure 3.6) derived from the measured impedance are summarized in Table 3.2. The comparison of the measured impedance and the modeled impedance for the 4-mm-by-4-mm piece is displayed in Figure 3.7, showing an correspondence between the model and the measurements. Similar to PVDF, PZT

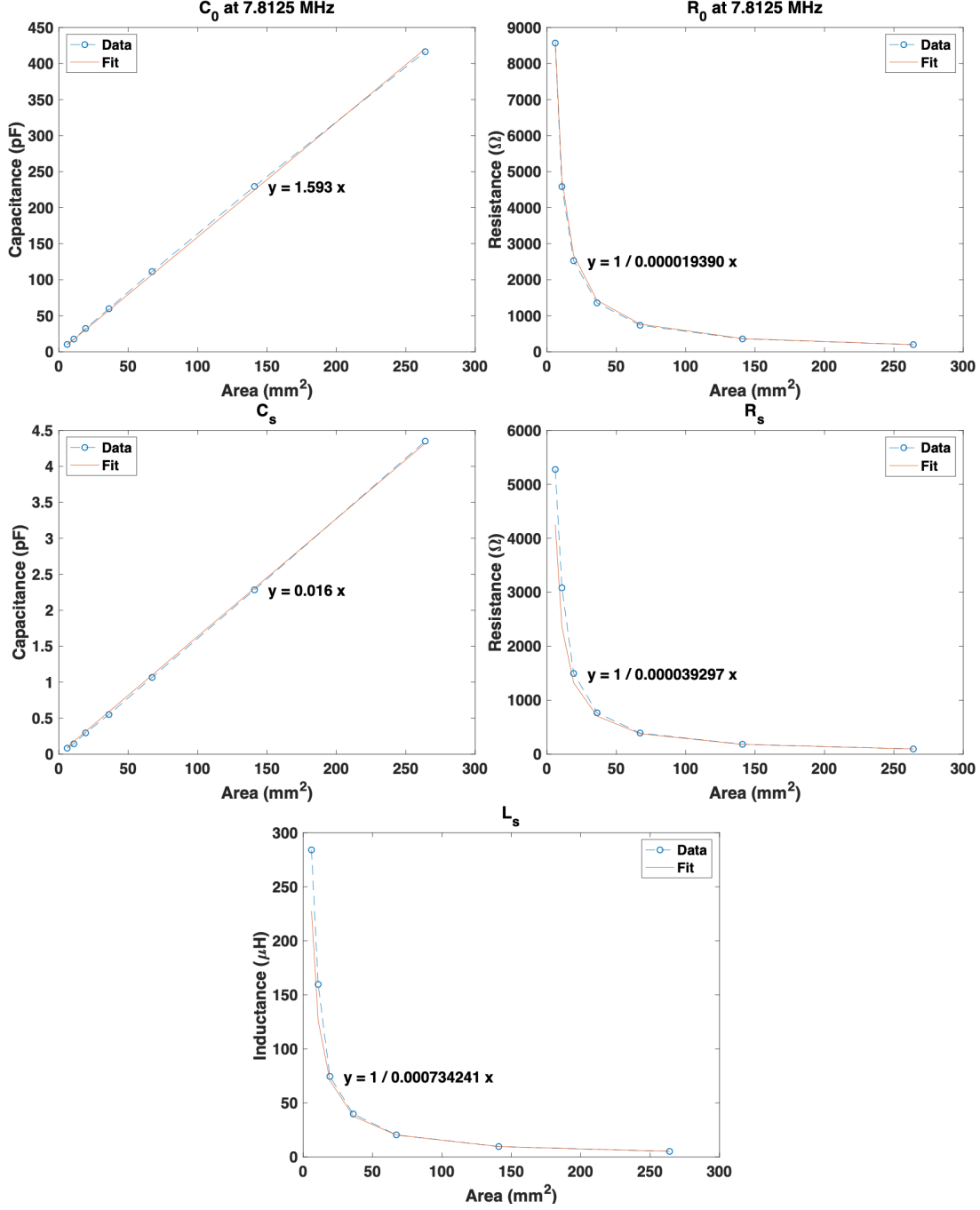


Figure 3.5: The area-scaling effect of the electrical model of PVDF.

also exhibits the area-scaling property, which can be used to derive the impedance for different sizes of PZT from these measurements.

The smallest feature size of the PZT transducers employed to interface with the CMOS chips was chosen to be 250  $\mu\text{m}$  in length, 250  $\mu\text{m}$  in width, and 267  $\mu\text{m}$

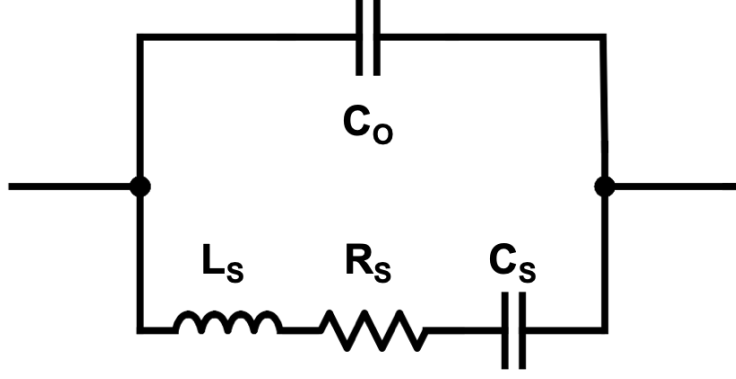


Figure 3.6: The electrical model of PZT.

Table 3.2: Extracted component values of different sizes of PZT.

Size (mm)	$C_O$ (pF)	$L_S$ ( $\mu$ H)	$R_S$ ( $\Omega$ )	$C_S$ (pF)
$4 \times 4$	680.21	1.97	3.65	200.73
$3.5 \times 3.5$	522.29	2.47	6.48	150.91
$3 \times 3$	368.24	3.64	9.54	106.80
$2.5 \times 2.5$	239.58	5.60	18.38	70.43
$2 \times 2$	172.53	8.24	17.69	46.18
$1.5 \times 1.5$	85.32	18.04	62.70	20.96
$1 \times 1$	37.25	49.90	85.82	6.85

in thickness, rendering it difficult to accurately measure its impedance due to the small size. Therefore, the impedance of the  $2 \text{ mm} \times 2 \text{ mm}$  PZT piece with the same thickness was used to derive the impedance of this micron-scale transducer by scaling the magnitude of the impedance at the same measured phase. As shown in Figure 3.8, this scaled impedance has a minimum of  $1.13 \text{ k}\Omega$  at resonance (8.1 MHz). This resonance was confirmed by exciting the same PZT piece with a 5-V-peak-to-peak sinusoidal signal between 6 MHz to 10 MHz and measuring the amplitude of the acoustic pressure generated from the PZT with a hydrophone (HGL-0200, Onda Corp.) coupled with a preamplifier (AG-2010, Onda Corp.), as plotted in Figure 3.9. The PZT exhibited the strongest piezoelectric response with the highest output pressure at 8.1 MHz. As a result, we chose our operating frequency to be 8.3 MHz, the supported frequency of the Vantage 256 system closest to 8.1 MHz. As a result, we

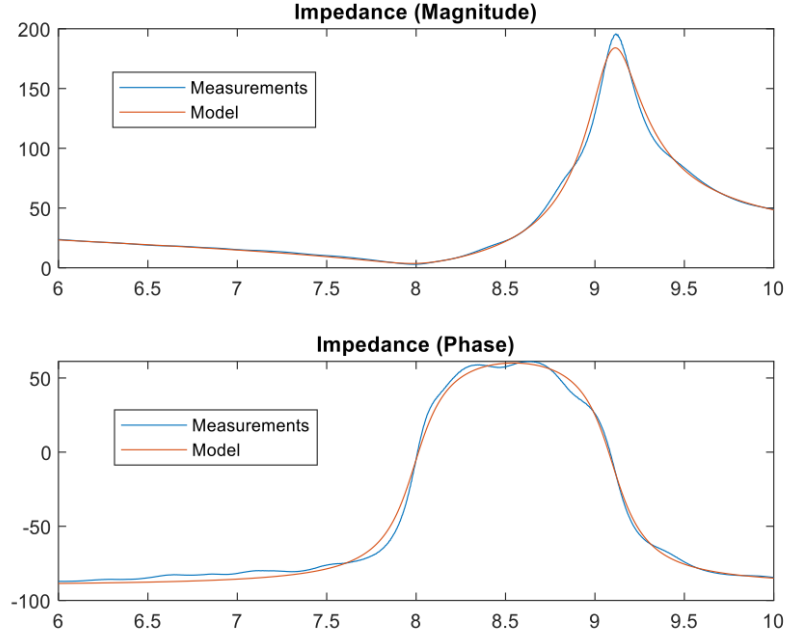


Figure 3.7: The modeled impedance in comparison with the measured impedance for a 4-mm-by-4-mm piece of PZT.

chose our operating frequency to be 8.3 MHz, the supported frequency of the Vantage 256 system closest to 8.1 MHz and also the center frequency of the L12-3v ultrasound probe. With a wavelength of  $\sim 185 \mu\text{m}$ , this operating frequency provides a lateral resolution of  $\sim 280 \mu\text{m}$  and a focal spot size as small as  $\sim 350 \mu\text{m}$  [92], matching the dimensions of the motes and enabling these motes to be resolved and detected in imaging and to be targeted for more effective powering and communication.

### 3.3 Design of a temperature sensor chip

The temperature sensor chip of the proposed sensing mote was implemented in a Taiwan Semiconductor Manufacturing Company (TSMC) 0.18- $\mu\text{m}$  CMOS mixed signal 1P6M (a single polysilicon layer underneath six metal layers) process. As illustrated in Figure 3.10, the chip consists of a front-end rectifier, two voltage regulators with built-in voltage references, a temperature sensing oscillator, a level shifter, and an

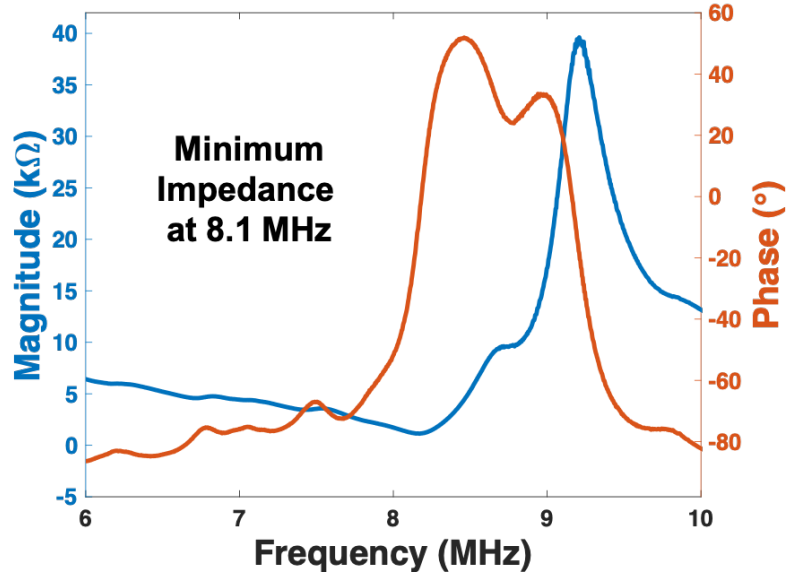


Figure 3.8: Derived impedance of a  $250 \mu\text{m} \times 250 \mu\text{m}$  PZT piece scaled from the measured impedance of a  $2 \text{ mm} \times 2 \text{ mm}$  PZT piece.

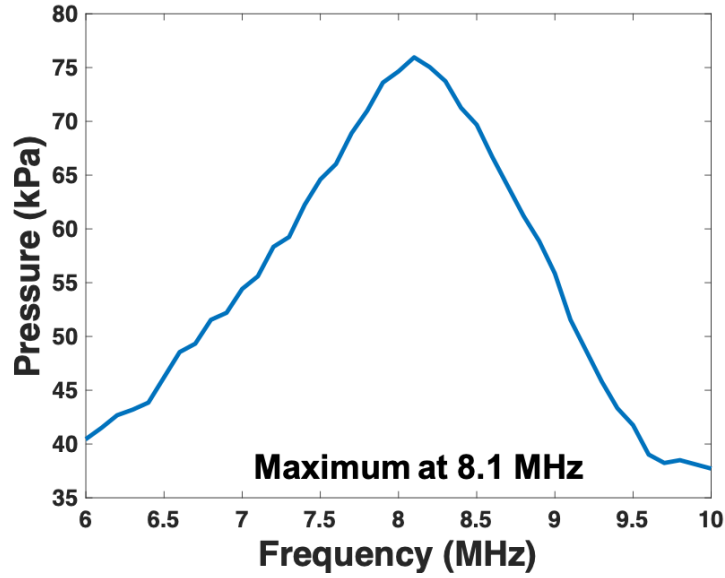


Figure 3.9: The output pressure amplitude of the  $2 \text{ mm} \times 2 \text{ mm}$  PZT piece with excitation voltage across frequency.

n-type MOS (NMOS) transistor acting as a backscatter modulator.

The rectifier is based on a voltage-doubler topology implemented with low-leakage MOS diodes. It converts the alternating-current (AC) ultrasound energy harvested from the piezoelectric transducer into the direct-current (DC) supply voltage  $V_{DD}$ .

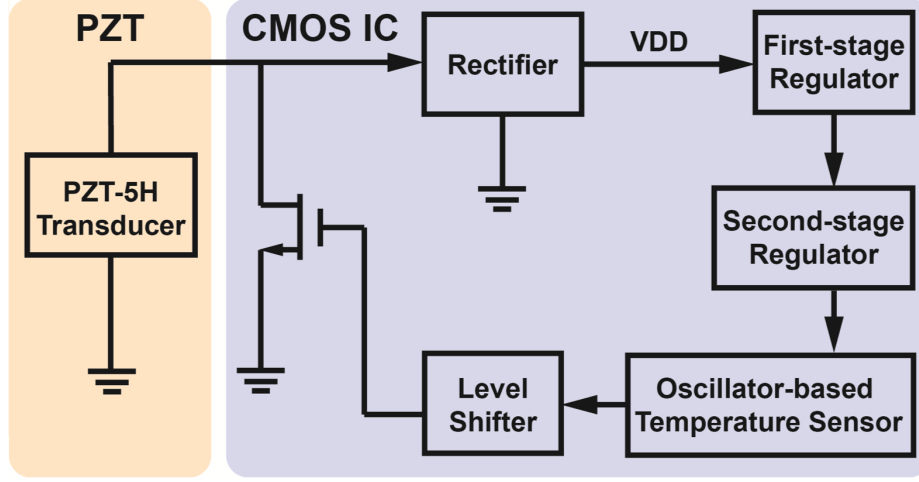


Figure 3.10: Block diagram of the temperature sensing mote.

[95], which is fed into two stages of subthreshold voltage regulators. The output of the second-stage regulator provides the supply for a temperature-sensing subthreshold relaxation oscillator, whose oscillation frequency varies with temperature. The temperature-dependent oscillator output is level-shifted to  $VDD$  to drive the NMOS modulator shunted across the piezoelectric transducer to induce a two-level change in the electrical loading of the transducer. The resulting modulated ultrasound echoes transmit the temperature information back to the ultrasound probe through acoustic backscattering. Subthreshold operation of the major circuit blocks ensures sub-1-nW power consumption for the mote. The design specifications and considerations of each circuit block are detailed below.

### 3.3.1 Front-end rectifier

The front-end rectifier driven by an AC voltage source is shown in Figure 3.11. The steady-state circuit operation can be described for each half-period [58]. During the negative phase,  $D_1$  is forward-biased and the current  $I_1$  through  $D_1$  charges  $C_1$  to a DC voltage ideally equal to the AC input voltage amplitude;  $D_2$  is reverse-biased and prevents charge on  $C_2$  from flowing back into  $C_1$ . During the positive phase,  $D_2$  is

forward-biased and the current  $I_2$  through  $D_2$  discharges  $C_1$  and charges  $C_2$  to create an output voltage ideally equal to twice the input voltage amplitude;  $D_1$  is reversed biased and prevents charge on  $C_1$  from flowing back to ground.

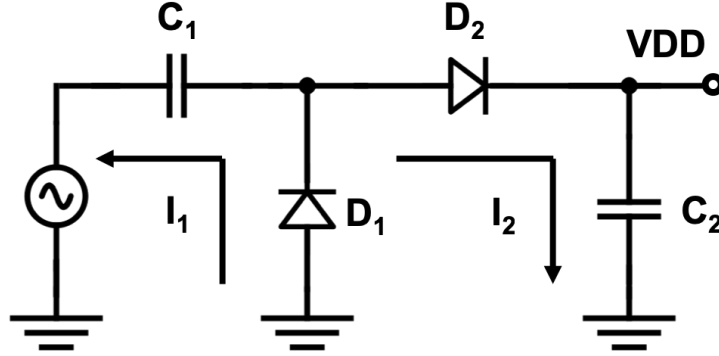


Figure 3.11: Schematic of a voltage-doubler rectifier.

The rectifier output is usually lower than twice the input voltage amplitude due to a finite turn-on voltage and a finite on-state resistance of the diodes. For conventional MOS-based diodes, the turn-on voltage is the threshold voltage  $V_{th}$  of the MOS transistors; this voltage drop is usually minimized through the use of low- $V_{th}$  devices. However, low- $V_{th}$  transistors, especially native transistors with a near-zero  $V_{th}$ , typically come with large leakage currents when they are reverse biased. In this design, we optimized the forward-to-reverse current ratio for the diodes that maintains proper circuit function for 0.5%-duty-cycle ultrasound pulses. To achieve this, we used the ultra-low-power (ULP) diode [96], depicted in Figure 3.12, to implement  $D_1$  and  $D_2$  in the rectifier. The ULP diode consists of an NMOS transistor and a p-type MOS (PMOS) transistor. When forward biased, the ULP diode behaves like two conventional MOS diodes connected in series. When reverse biased, however, both transistors in the ULP diode operate in the deep subthreshold region with negative gate-to-source voltages ( $V_{GS}$ ) as their sources are connected together. This leads to significantly lower leakage current compared to that of a standard MOS diode, which shows a zero  $V_{GS}$  when reversed biased.



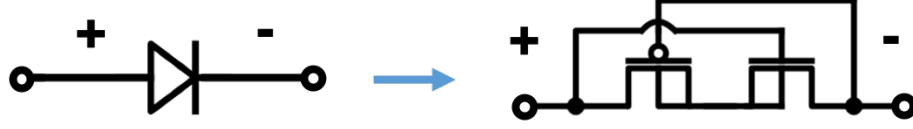


Figure 3.12: Schematic of an ULP diode used to implement  $D_1$  and  $D_2$  in Figure 3.11.

Figure 3.13 presents the detailed schematic of the rectifier, in which the electrical model of the PZT transducer (Figure 3.6) replaces  $C_1$  and different types of MOS devices are used to implement  $D_1$  and  $D_2$  for efficiency optimization. The AC voltage source along with the PZT model forms the Thévenin equivalent circuit of PZT with input excitation [94, 97–99]. The component values for a 250- $\mu\text{m}$ -by-250- $\mu\text{m}$  PZT derived from the measured electrical impedance shown in Table 3.2 is labeled on the PZT model.

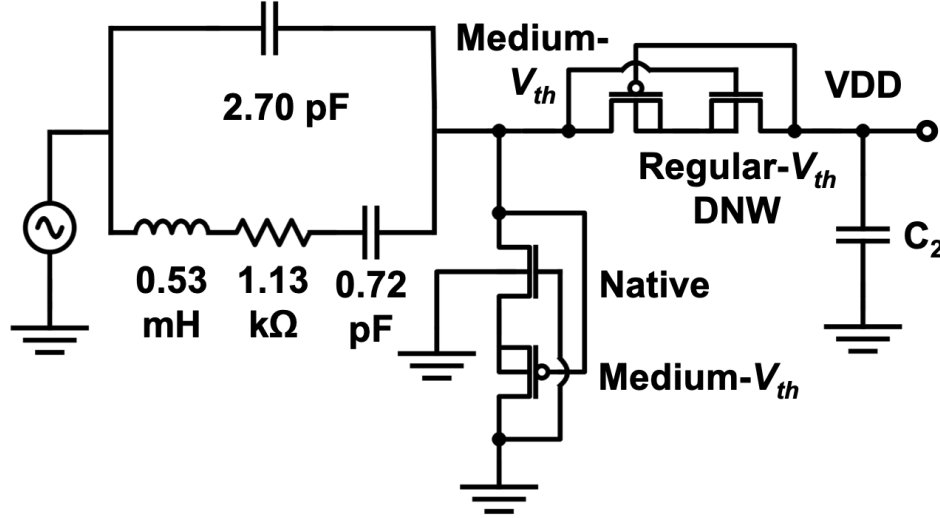


Figure 3.13: Detailed schematic of the rectifier with  $C_1$  replaced with the electrical model of PZT and  $D_1$  and  $D_2$  replaced with ULP diodes.

$C_2$  is a 250-pF on-chip capacitor, which stores the energy accumulated from the input source and stabilizes the rectifier output. This capacitor takes up the majority of the chip area and serves as the sole storage capacitor in the mote.  $D_1$  employs an NMOS native transistor to maximize the forward conduction and minimize the turn-

on voltage, while  $D_2$  is implemented with an NMOS regular- $V_{th}$  transistor with deep-N-well (DNW) to minimize the reverse leakage of charge from  $C_2$ . PMOS medium- $V_{th}$  transistors are used in both  $D_1$  and  $D_2$  to optimize the forward-conduction-to-reverse-leakage ratio.

The body connections of the PMOS transistor in  $D_1$  and both the NMOS and PMOS transistors in  $D_2$  reduce the parasitic junction leakage currents, cancel the source-body biasing in reverse bias, and also avoid latch-up during start-up [58]. The native NMOS transistor in  $D_1$  used to achieve a higher forward conduction has a slightly higher junction leakage, as native devices have no DNW for separate body connections. To further reduce the chances of latch-up, we performed careful layout by physically separating the NMOS and PMOS transistors and placing guard rings around each of the transistors. In addition, at a sub-1-nW operating power level, transiently, input voltages are less than 2 V and input currents are less than 5  $\mu\text{A}$ , minimizing the risk of latch-up.

The rectifier is designed around the operating frequency of ultrasound with a simulated power conversion efficiency of 71.3%.

### 3.3.2 Voltage regulator

Two cascaded stages of voltage regulators with the same architecture are used to regulate the rectifier output and generate a stable supply voltage (peak-to-peak ripple of  $<0.05$  V) for the temperature sensing oscillator. Employing two back-to-back regulators improves the power supply rejection ratio (PSRR), defined as the capability of a regulator to reject noise from the input supply voltage and the line sensitivity, defined as the variation of the oscillation frequency of the oscillator to the input voltage of the first-stage regulator. Each regulator contains a subthreshold voltage reference, which is regulated with a NMOS voltage follower in negative feedback. The basic structure of the voltage reference consists of two stacked NMOS transistors

[73], as shown in Figure 3.14.  $M_1$  serves as a subthreshold current source and feeds a current into the diode-connected transistor  $M_2$  to create an output voltage  $V_{ref}$ . The drain current  $I_D$ , flowing through a transistor operating in the subthreshold region can be expressed as

$$I_D = \mu_0 C_{ox} \frac{W}{L} (n-1) V_T^2 (e^{\frac{V_{GS}-V_{th}}{nV_T}}) (1 - e^{\frac{-V_{DS}}{V_T}}), \quad (3.1)$$

where  $\mu_0$  is the zero bias mobility,  $C_{ox}$  is the gate oxide capacitance,  $W$  is the transistor width,  $L$  is the transistor length,  $n$  is the substrate factor,  $V_T = kT/q$  is the thermal voltage ( $\sim 26$  mV at 300 K), and  $V_{DS}$  is the drain-to-source voltage [100]. For  $V_{DS}$  greater than 5-6  $V_T$ ,  $I_D$  can be approximated as

$$I_D = \mu_0 C_{ox} \frac{W}{L} (n-1) V_T^2 (e^{\frac{V_{GS}-V_{th}}{nV_T}}). \quad (3.2)$$

By assuming the same  $V_{th}$  for  $M_1$  and  $M_2$  and equating the current expressions for  $M_1$  and  $M_2$ , we obtain

$$\left(\frac{W_1}{L_1}\right) (e^{\frac{-V_{th}}{nV_T}}) = \left(\frac{W_2}{L_2}\right) (e^{\frac{(V_{ref}-V_{th})}{nV_T}}), \quad (3.3)$$

and  $V_{ref}$  is found to be

$$V_{ref} = nV_T \ln\left(\frac{W_1 L_2}{W_2 L_1}\right), \quad (3.4)$$

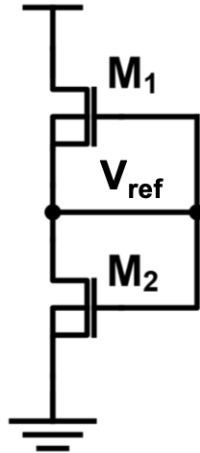


Figure 3.14: Schematic of an all-NMOS subthreshold voltage reference.

which is proportional to the process-independent thermal voltage. Since  $V_T$  is proportional to absolute temperature (PTAT),  $V_{ref}$  is also PTAT. The two transistors are both DNW devices with their bulks tied to their corresponding sources to eliminate the body effect. Transistor lengths are made large ( $>10 \mu\text{m}$ ) to reduce short channel effects.

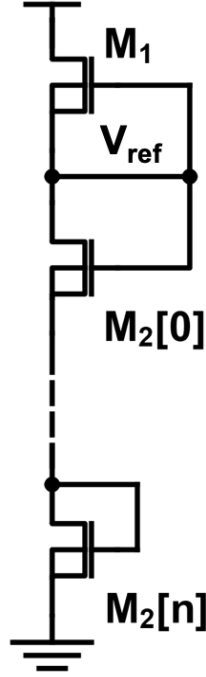


Figure 3.15: Schematic of the reference in Figure 3.14 with stacked NMOS diodes.

$M_2$  can be replaced with stacked and identical NMOS diodes to generate a different output voltage [101] (Figure 3.15). Different numbers of stacked NMOS diodes are used for the first-stage and second-stage regulators, creating  $\sim 0.64 \text{ V}$  and  $\sim 0.48 \text{ V}$  outputs with a  $1.5\text{-V}$  input while consuming  $\sim 34.4 \text{ pA}$  and  $\sim 18.9 \text{ pA}$  of currents, respectively, in simulation at  $37^\circ\text{C}$ .

For each regulator, the reference voltage  $V_{ref}$  from Figure 3.15 is then fed into an NMOS source follower  $M_3$  with the output fed back to the NMOS diode  $M_2[0]$ , providing negative feedback to create a regulated voltage approximately equal to  $V_{ref}$  [102], as illustrated in Figure 3.16. All-NMOS design for these voltage regulators

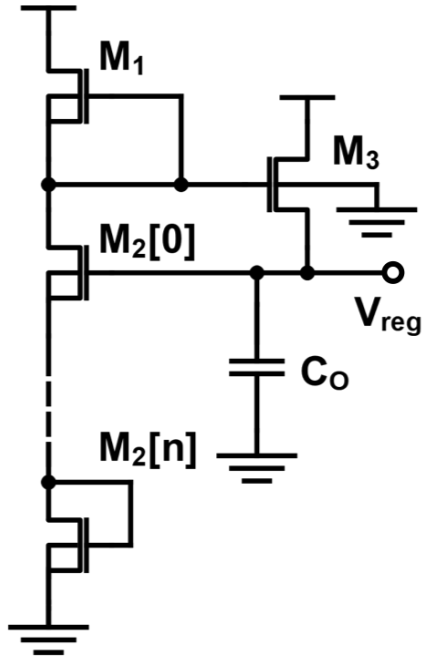


Figure 3.16: Schematic of the the complete voltage regulator.

reduces process variations. A decoupling capacitor  $C_O$  (1.45 pF for the first stage and 1.58 pF for the second stage) is added at the regulator output to improve the line sensitivity and PSRR.

The output from the second-stage regulator,  $V_{reg}$ , provides the local supply for a temperature-sensing RC relaxation oscillator with an oscillation frequency that tracks the temperature. Without dedicated compensation, the PTAT characteristic of  $V_{reg}$  is incorporated into the overall temperature characteristics of the sensing mote. When driving the oscillator, the first-stage and second-stage regulators show simulated efficiencies of 37.8% and 69.9%, respectively, where the lower efficiency of the first-stage regulator results from it having a larger drop-out voltage from the input of 1.5 V to the output of  $\sim 0.64$  V.

### 3.3.3 Temperature-sensitive oscillator

A relaxation oscillator is an astable multivibrator circuit that switches between two quasi-stable states (high and low), producing a period signal whose frequency is determined by the charging and discharging of a timing capacitor [103]. The basic architecture of the relaxation oscillator is shown in Figure 3.17, which contains two

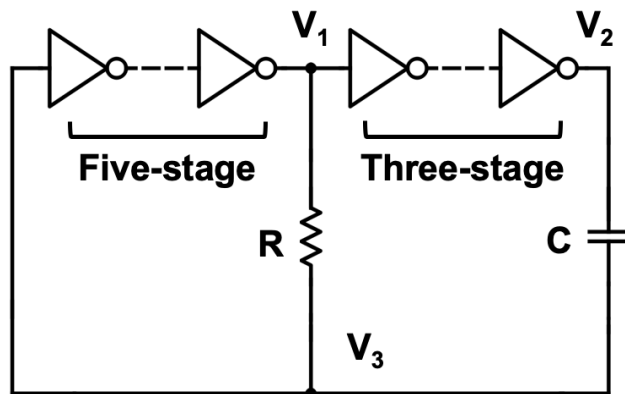


Figure 3.17: Schematic of a relaxation oscillator.

inverter chains, a capacitor  $C$  connected from  $V_2$  to  $V_3$ , and a resistor  $R$  connected from  $V_1$  to  $V_3$ . The use of inverter chains here (of five and three stages) provides high gain and ensures a square-wave voltage at the output [102]. The voltage waveforms at node  $V_1$ ,  $V_2$ , and  $V_3$  are illustrated in Figure 3.18. If we define the inverter switching point as  $K_{SW} = V_{SW}/V_{reg}$ , where  $V_{SW}$  is the switching voltage when the input equals the output, the circuit operation can be described as follows. Assuming node  $V_1$  is initially at ground, node  $V_2$  is high at  $V_{reg}$ , and node  $V_3$  is at a voltage higher than  $V_{SW} = K_{SW}V_{reg}$ . The capacitor starts to discharge with a time constant of  $RC$  until node  $V_3$  reaches  $V_{SW}$ . The inverter chains change states such that node  $V_1$  is high and node  $V_2$  is low. Node  $V_3$  is then immediately pulled down to  $(K_{SW} - 1)V_{reg}$  as the voltage across the capacitor cannot change instantaneously. The capacitor  $C$  then starts to charge up until it reaches  $V_{SW}$ , switching the inverter chains again. This time,  $V_3$  is pulled up to  $(K_{SW} + 1)V_{reg}$  before discharging starts, and the operation repeats.  $V_2$  is used as the oscillator output after a buffer stage. The oscillation period

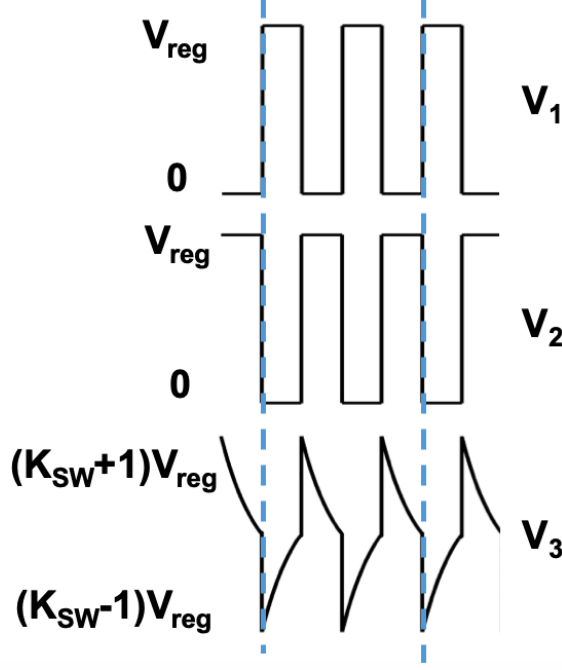


Figure 3.18: The voltage waveforms at nodes  $V_1$ ,  $V_2$ , and  $V_3$  in Figure 3.17.

is the sum of the time it takes for the capacitor to discharge ( $t_1$ ) and to charge ( $t_2$ ) and the total delay through the inverters, denoted as  $\tau_{inv}$ , during one cycle.  $t_1$  and  $t_2$  are determined by:

$$(K_{SW} + 1)V_{reg}e^{-\frac{t_1}{RC}} = K_{SW}V_{reg}, \quad (3.5)$$

and

$$V_{reg} + ((K_{SW} - 1)V_{reg} - V_{reg})e^{-\frac{t_2}{RC}} = K_{SW}V_{reg}. \quad (3.6)$$

Therefore, the oscillation frequency  $f$  can be expressed as

$$f = \frac{1}{(t_1 + t_2) + \tau_{inv}} \approx \frac{1}{Q_{SW}RC + \tau_{inv}}, \quad (3.7)$$

where

$$Q_{SW} = \ln \frac{(K_{SW} + 1)(2 - K_{SW})}{K_{SW}(1 - K_{SW})}. \quad (3.8)$$

$K_{SW}$  is designed to be 0.5, where the duty cycle of the oscillation is 50% and  $f$  achieves the highest immunity to  $K_{SW}$  variation. A 10% variation of  $K_{SW}$  from 0.5 decreases the oscillation frequency by only 0.4%. In addition, we target  $f$  in the Hz-range such that  $\tau_{inv} \ll Q_{SW}RC$  and  $f \approx \frac{1}{Q_{SW}RC} \approx \frac{1}{2.2RC}$ . Such low frequencies save power and

are sufficient for quantifying slowly-varying physiological temperature.  $V_{reg}$  allows the inverters to run in the subthreshold region with a simulated current of  $<300$  pA at oscillator frequencies of a few Hz at  $37^\circ\text{C}$ .

To achieve these oscillation frequencies, the resistor  $R$  must be in the  $\text{G}\Omega$  range, realized with the pseudo-resistor structure (Figure 3.19), in which two identical, well-matched NMOS transistors are connected in series. Looking from both terminals,

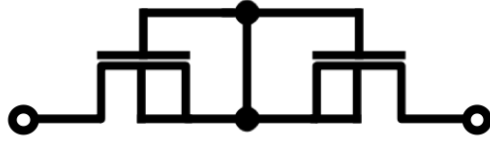


Figure 3.19: The pseudo-resistor used to implement the resistor  $R$  in Figure 3.17.

the pseudo-resistor can be viewed as an off-state NMOS with a zero  $V_{GS}$  in series with a forward-biased NMOS diode, and the equivalent resistance in both directions is determined by the voltage difference across the pseudo-resistor,  $|V_1 - V_3|$ , and the subthreshold leakage current  $I_D$  in Equation 3.1 through each of the two NMOS transistors. Since  $|V_1 - V_3|$  is between  $0.5V_{reg}$  and  $1.5V_{reg}$  (when  $K_{SW} = 0.5$ ), which is larger than  $5-6 V_T$ ,  $I_D$  becomes largely independent of  $|V_1 - V_3|$  and can be approximated as in Equation 3.2. In that case, the capacitor  $C$  is charged and discharged with a constant current flowing through the pseudo-resistor, resulting in a linear voltage ramp of  $K_{SW}V_{reg} - (K_{SW} - 1)V_{reg} = V_{reg}$  during the charging cycle and  $(K_{SW} + 1)V_{reg} - K_{SW}V_{reg} = V_{reg}$  during the discharging cycle at node  $V_3$ . Therefore,  $f$  can be calculated as

$$\begin{aligned} f &= \frac{1}{t_1 + t_2} = \frac{1}{\frac{C_{eff}V_{reg}}{I_D} + \frac{C_{eff}V_{reg}}{I_D}} = \frac{I_D}{2C_{eff}V_{reg}} \\ &= \frac{\mu_0 C_{ox} \frac{W}{L} (n-1) V_T^2 (e^{\frac{-V_{th}}{nV_T}})}{2C_{eff}V_{reg}}, \end{aligned} \quad (3.9)$$

where  $C_{eff}$  is the effective capacitance of the capacitor  $C$ , implemented with an NMOS capacitor, and  $f$  is no longer affected by  $K_{SW}$ , resulting in a stable 50% duty



cycle across process corners. By taking into account the temperature dependences of  $\mu_0$ ,  $V_T$ , and  $V_{th}$ , and letting  $V_{reg} = V_{cons}V_T$ , where  $V_{cons}$  is a temperature independent constant, the relation between  $f$  and the temperature,  $T$ , can be expressed as [104]

$$f(T) = \frac{\mu_0(T_0)(\frac{T}{T_0})^{-1.5}C_{ox}\frac{W}{L}(n-1)(\frac{kT}{q})^2(e^{\frac{-q(V_{th}(T_0)-K(T-T_0))}{nkT}})}{2C_{eff}V_{cons}\frac{kT}{q}} \\ = AT^{-0.5}(e^{\frac{B}{T}}), \quad (3.10)$$

where  $T$  is absolute temperate,  $T_0 = 300K$ , and the temperature-dependent mobility and threshold voltage are given by  $\mu_0(T) = \mu_0(T_0)(T/T_0)^{-1.5}$  and  $V_{th}(T) = V_{th}(T_0) - K(T - T_0)$  [105], respectively. Here, the secondary effects, such as the variation of  $V_{reg}$  due to supply noise, the temperature dependence of the capacitor  $C$ , and the matching errors in the pseudo-resistor  $R$ , are not included. We define the temperature-independent coefficients  $A$  and  $B$  as:

$$A = \frac{\mu_0(T_0)(\frac{1}{T_0})^{-1.5}C_{ox}\frac{W}{L}(n-1)(\frac{k}{q})(e^{\frac{qK}{nk}})}{2C_{eff}V_{cons}}, \quad (3.11)$$

and

$$B = \frac{-q(V_{th}(T_0) + KT_0)}{nk}, \quad (3.12)$$

respectively. A two-point calibration ( $f$  measured at temperatures  $T_1$  and  $T_2$ ) can be used to determine fitting values for  $A$  and  $B$ , denoted as  $\tilde{A}$  and  $\tilde{B}$ .  $\tilde{B}$  is determined from:

$$\frac{f(T_1)}{f(T_2)} = (\frac{T_1}{T_2})^{-0.5}e^{\tilde{B}(\frac{1}{T_1} - \frac{1}{T_2})}. \quad (3.13)$$

With this value of  $\tilde{B}$ , the overall scaling factor  $\tilde{A}$  is then determined from:

$$f(T_1) = \tilde{A}T_1^{-0.5}e^{\frac{\tilde{B}}{T_1}}. \quad (3.14)$$

Such two-point calibration, performed for each oscillator, accounts for the chip-to-chip variation in  $I_D$ ,  $C_{eff}$ , and  $V_{reg}$ . We define the temperature  $T_{fit}$  as the one determined by  $\tilde{A}$ ,  $\tilde{B}$  and the measured frequency  $f$ :

$$T_{fit} = \frac{\tilde{B}}{\ln(\frac{f}{\tilde{A}T_{fit}^{-0.5}})}, \quad (3.15)$$

which must be solved self-consistently for  $T_{fit}$ . The difference between  $T_{fit}$  and each measured temperature  $T$  is taken as the temperature error for this oscillator.

As an alternative to this calibration, the trimming of the oscillator frequency could also be achieved using a capacitor array with on-chip programmable fuses to implement the capacitor in the oscillator. A fuse is a metal trace that connects two nodes in the circuit, which can be disconnected through a metal etching process or laser cut. In the mass-production case, probes can be used to apply supply voltages to an oscillator-under-test and measure the output frequency using on-chip testing pads. A portion of the fuses can be selectively cut to obtain the desired capacitance for the oscillator to achieve the nominal frequency. This can be applied to mitigate part-to-part variation on the wafer level, which is not implemented in the current chip but has been demonstrated previously in our lab [77].

### 3.3.4 Level shifter

The oscillator output,  $V_{osc}$ , is level-shifted from  $V_{reg}$  to the rectifier output,  $VDD$ , which is the highest available DC voltage in the circuit, using a level shifter to provide a large enough turn-on voltage for the NMOS modulator. In a conventional level shifter that converts a lower level of  $VDDL$  to a higher level of  $VDDH$  [1] (Figure 3.20), when the input is  $VDDL$ ,  $M_4$  is turned off and  $M_3$  is turned on, pulling node

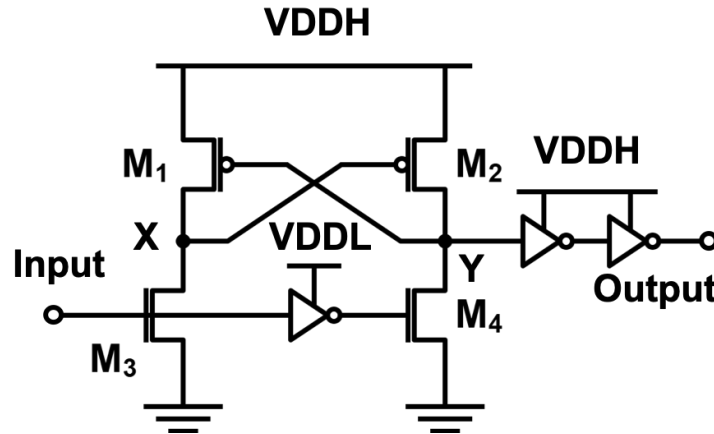


Figure 3.20: Schematic of a conventional level shifter.

X to ground, which turns on  $M_2$ . This pulls up node Y and the output to  $VDDH$ , which ensures that  $M_1$  is off. Similarly, when the input is low, the output is driven low. However, this architecture suffers from contention between the PMOS transistors and NMOS transistors and also crowbar currents when the PMOS and NMOS devices are simultaneously on during signal transitions, which increases dissipated power. We, therefore, implemented a contention mitigated level shifter [106] with two additional transistors,  $M_5$  and  $M_6$ , as illustrated in Figure 3.21.  $M_5/M_6$  along with  $M_3/M_4$  acts as a quasi-inverter to speed to full-rail logic levels at node X and Y. This reduces contention and crowbar currents and saves power with a simulated current consumption of 179.2 pA at 37 °C.

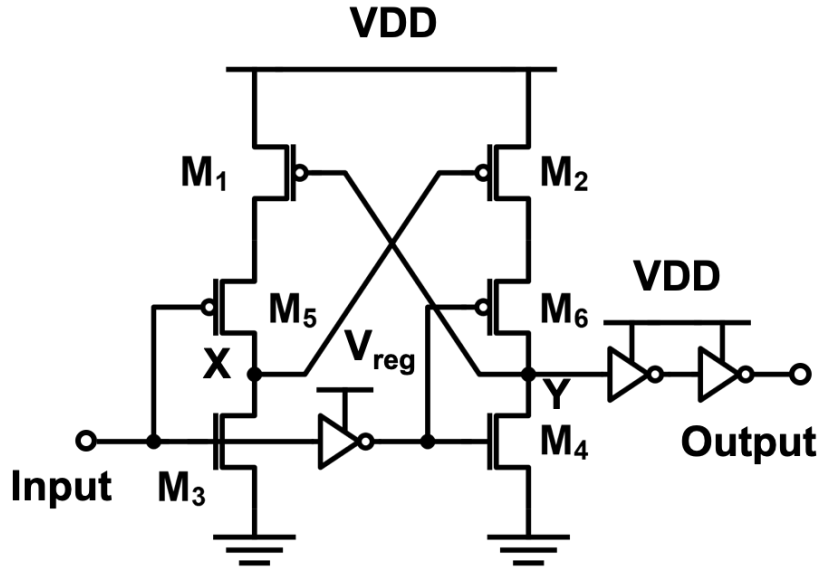


Figure 3.21: Schematic of a contention mitigated level shifter used in this design.

### 3.3.5 Modulator

The up-shifted oscillation signal from the level-shifter, periodically turns the NMOS modulator on and off (Figure 3.10). This switching places a low electrical impedance (when the modulator is on) or a high impedance (when the modulator is off) in parallel with the piezoelectric transducer. This varying electrical impedance at the transducer

causes the amplitude of the backscattered ultrasound echoes to vary accordingly [107]. In this way, the oscillation frequency and thus the encoded temperature information can be extracted with the ultrasound system that receives and processes the reflected echoes.

### 3.3.6 Power breakdown

The simulated power breakdown of each circuit block is shown in Figure 3.22. The total power consumption of the two regulators, the oscillator, and the level shifter, was found to be  $\sim 708.5$  pA at  $37^\circ\text{C}$  with a 1.5-V DC voltage driving the regulator input. The average power consumption of the modulator, or the average power absorbed into the mote, was simulated to be  $\sim 26$  nW ( $\sim 47$  nW when the modulator was on and  $\sim 2$  nW when the modulator was off).

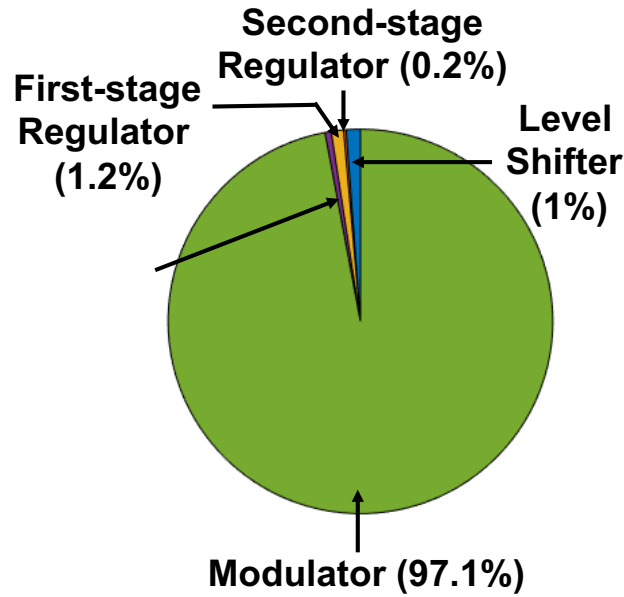


Figure 3.22: The simulated power breakdown of the major circuit blocks.

### 3.3.7 Die micrograph

The die micrograph of the chip is shown in Figure 3.23. It measures  $4\text{ mm} \times 3.2\text{ mm}$  and contains two standalone oscillators and three groups of temperature sensor chips with different sizes. One group, located on the upper part of the die, contains three identical chips with dimensions of  $1.1\text{ mm} \times 1\text{ mm}$ , the second group, located at the center of the die, contains ten identical chips with dimensions of  $350\text{ }\mu\text{m} \times 250\text{ }\mu\text{m}$ , and the third group, located on the lower part of the die, contains ten identical chips with dimensions of  $600\text{ }\mu\text{m} \times 500\text{ }\mu\text{m}$ . All these different sizes of chips contain

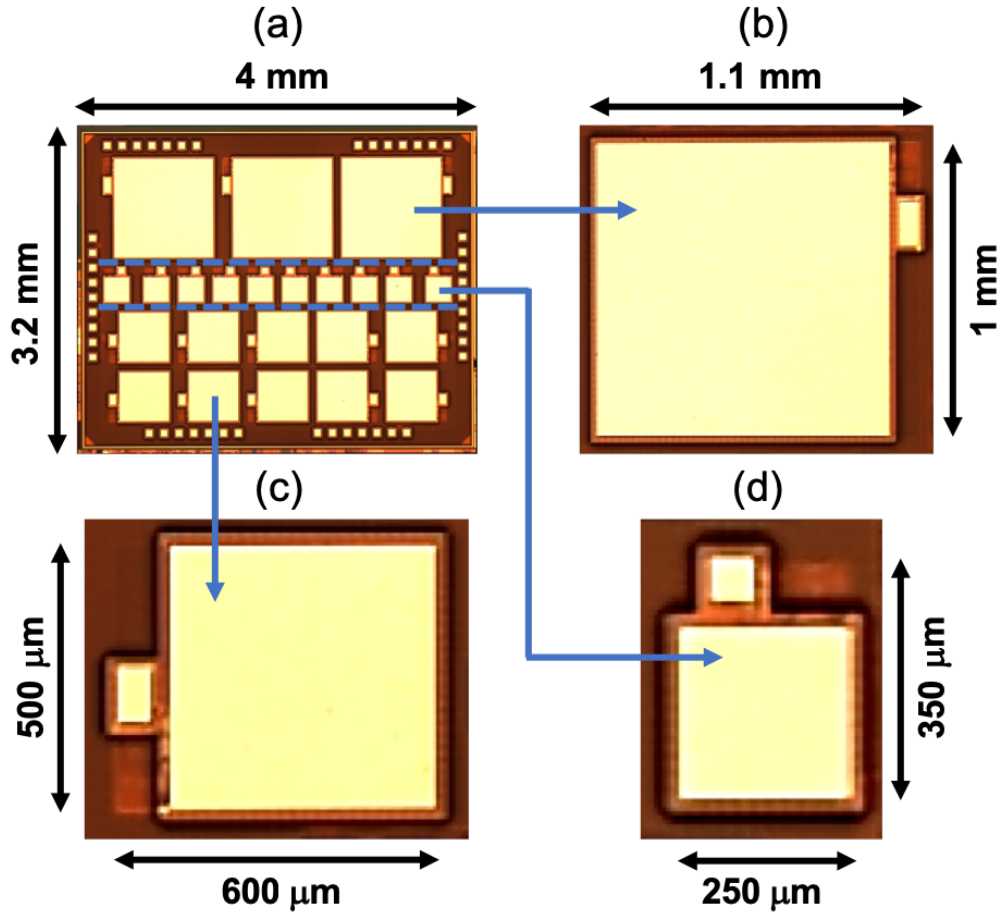


Figure 3.23: The die micrograph showing the three groups of temperature sensing chips with varying sizes.

essentially the same circuitry with similar layout, except slightly different sizing in the transistors and the storage capacitors of the rectifiers. As an example, the locations

of the major circuit blocks in a  $350\text{-}\mu\text{m}$ -by- $250\text{-}\mu\text{m}$  chip is labeled in Figure 3.24, where the first-stage regulator takes an area of  $87\text{ }\mu\text{m} \times 64\text{ }\mu\text{m}$ , the second-stage regulator maintains a size of  $110\text{ }\mu\text{m} \times 39\text{ }\mu\text{m}$ , and the oscillator occupies  $82\text{ }\mu\text{m} \times 30\text{ }\mu\text{m}$ .

I intentionally designed these three groups of chips with varying sizes to investigate the feasibility of monolithically integrating different sizes of piezoelectric transducers with the CMOS chips, which will be discussed in Chapter 4. Within each group, two chips have testing pads connected to some critical nodes inside the chips for both electrical characterization and testing with ultrasound input; the remaining chips contain no testing pads enabling only wireless ultrasonic operation.

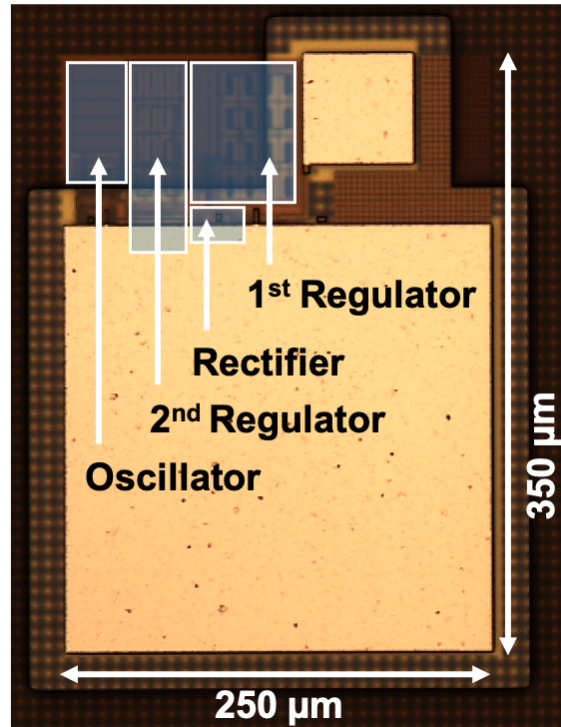


Figure 3.24: The micrograph of one  $350\text{-}\mu\text{m}$ -by- $250\text{-}\mu\text{m}$  chip showing the locations of the major circuit blocks.

### 3.4 Measurement results by direct probing

The line sensitivity, power consumption, and jitter performance of the relaxation oscillator with and without the voltage regulation were performed through direct probing on a probe station. Full-chip characterization will be detailed in Chapter 5.

First, six standalone relaxation oscillators were tested at room temperature ( $\sim 22^\circ\text{C}$ ) by directly probing the testing pads with DC probes (DCP 100, FormFactor Inc.) to power up each oscillator and take measurements, as shown in Figure 3.25. The dies containing these oscillators were covered in a metal box during the testing to prevent the effects of light on circuit operation arising from some high-impedance nodes in the circuit. The supply voltage to the oscillator was provided by a semiconductor device parameter analyzer (B1500A, Keysight). The output frequency was measured with a universal frequency counter (53132A, Keysight) and the power consumption was acquired with the parameter analyzer, as shown in Figure 3.26a and Figure 3.26b, respectively. When the supply voltage varies from 0.25 V to 0.65 V, the oscillators have an average line sensitivity of 145.3 %/V (the standard deviation  $\sigma$  over the mean  $\mu$  is 0.0087) as the average frequency changes from  $\sim 4.13$  Hz to  $\sim 1.73$  Hz. Also, the

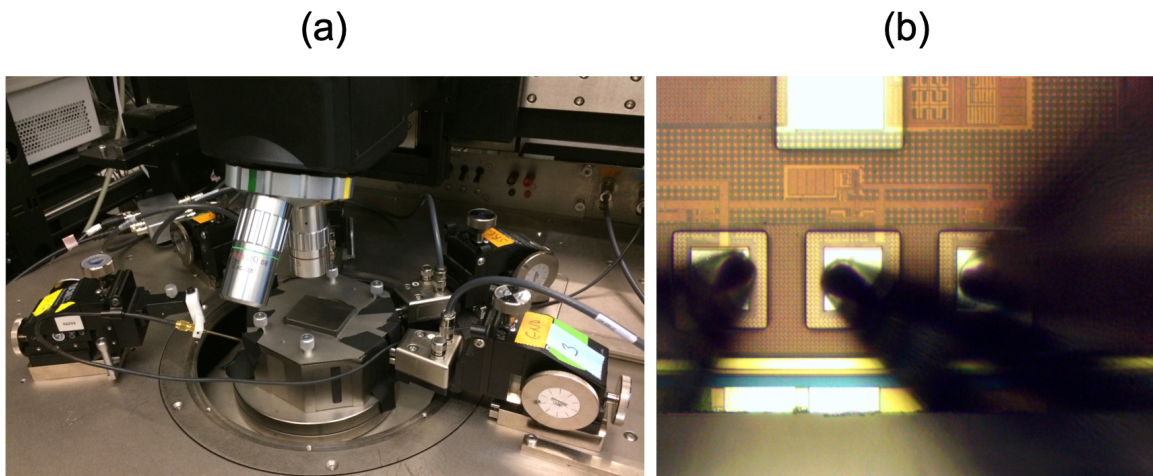


Figure 3.25: (a) The testing setup on the probe station to test the oscillators; (b) a micrograph showing three DC probes landing on the testing pads of an oscillator for powering up the oscillator and taking measurements.

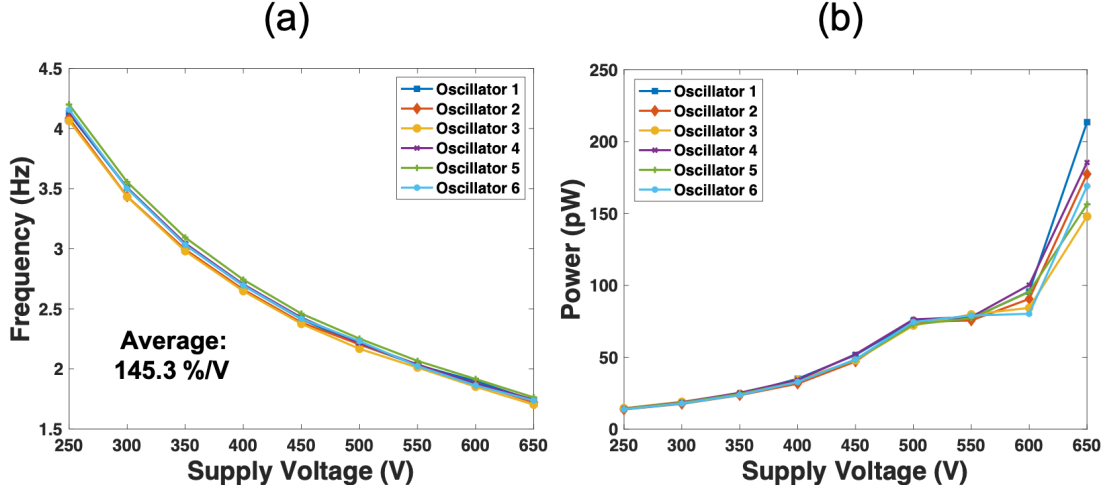


Figure 3.26: (a) The line sensitivity of six oscillators; (b) the power consumption of the six oscillators.

power consumption varies from  $\sim 14.1$  pW to  $\sim 175$  pW as the biasing condition of the inverters in the oscillator changes from weak inversion to strong inversion with increasing supply voltage.

Next, the output frequency and power consumption of three oscillators with on-chip voltage regulation was measured in a similar way using the DC probes at room temperature. With the on-chip voltage regulation, however, the average line sensitivity reduces to  $0.61$  %/V ( $\sigma / \mu = 0.17$ ), as plotted in Figure 3.27a. In this

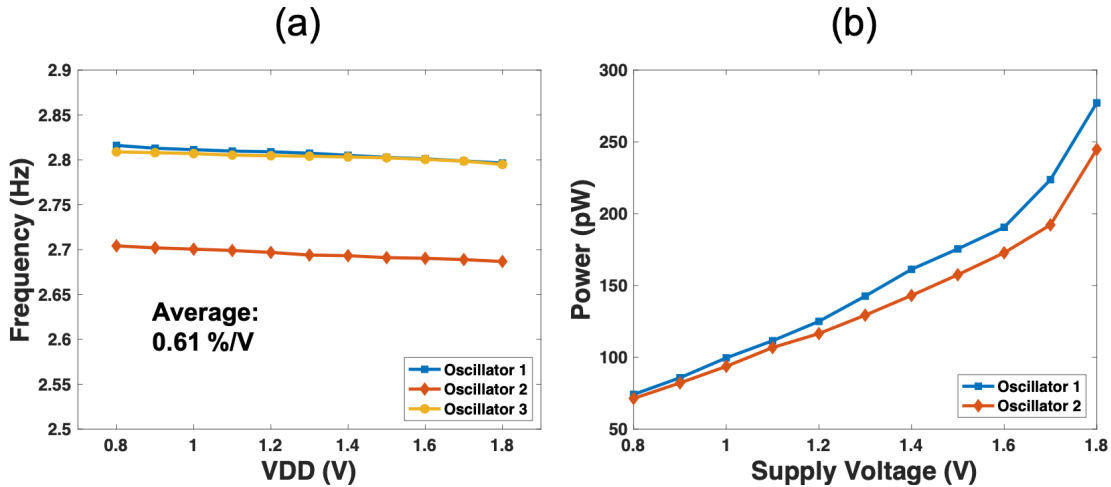


Figure 3.27: (a) The line sensitivity of three oscillators with voltage regulation; (b) the power consumption of two of the three regulated oscillators.



measurement, a DC voltage from 0.8 V to 1.8 V was directly applied to the input of the first-stage regulator, where the power consumption varies from 72.8 pW to 261 pW (Figure 3.27b).

In addition, the total power consumption of the two regulators, the oscillator, and the level shifter, was measured to be  $\sim 541.9$  pA at 37 °C with a 1.5-V supply ( $\sim 0.813$  nW) applied at the regulator input.

Finally, the period jitter for the oscillator was measured at room temperature by taking 100 consecutive periods with the counter and computing the standard deviation over the mean of the measurements. The oscillator alone shows an average jitter of 287.9 parts-per-million (ppm,  $\sigma / \mu = 0.082$ ) with a 0.4-V supply, while the regulated oscillator shows an average jitter of 401.1 ppm ( $\sigma / \mu = 0.18$ ) with a 1.5-V supply.

---

## Chapter 4

# Microfabrication of the Temperature Sensing Motes

---

### 4.1 Introduction

This chapter presents the development of microfabrication techniques achieving the monolithic integration of the CMOS temperature sensor chips with both PVDF and PZT transducers at the micron scale to create the extremely-miniaturized sensing motes. Conventionally, piezoelectric transducers are discretely packaged with the associated interfacing electronics for ultrasonic wireless systems [52, 59, 74, 75] and piezoelectric devices [108, 109], which suffer from large form factors. Here, we instead chose to directly build piezoelectric transducers on top of the sensor chips. This approach, compared to packaged solutions, significantly reduces the mote volumes

and the parasitic capacitance associated with the CMOS-transducer interfaces, which can divide-down signal levels due to the low intrinsic capacitance of the micron-scale transducers [68, 110].

For achieving this monolithic integration, the rectifier input and the ground nodes of the chips were routed to the top metal layer as accessible pads, as illustrated in Figure 4.1a, Figure 4.1b, and Figure 4.1c for the three groups of chips with sizes of  $1.1 \text{ mm} \times 1 \text{ mm}$ ,  $600 \text{ }\mu\text{m} \times 500 \text{ }\mu\text{m}$ , and  $350 \text{ }\mu\text{m} \times 250 \text{ }\mu\text{m}$ , respectively. The input pad and the ground pad will be electrically connected to the top and bottom surfaces, respectively, of a PVDF transducer or a PZT transducer, which are the two terminals for this transducer to generate an output voltage when ultrasound pressure is applied. The sizes of the ground pads as well as the sizes of the input pads for the three sizes of chips are denoted in the caption of Figure 4.1. The size of the ground pad determines the size of the PZT transducer to be integrated with a chip, whereas the size of the input pad should be minimized to reduce the parasitic capacitance of that pad to the bulk silicon of the chip, which impairs the rectifier efficiency.

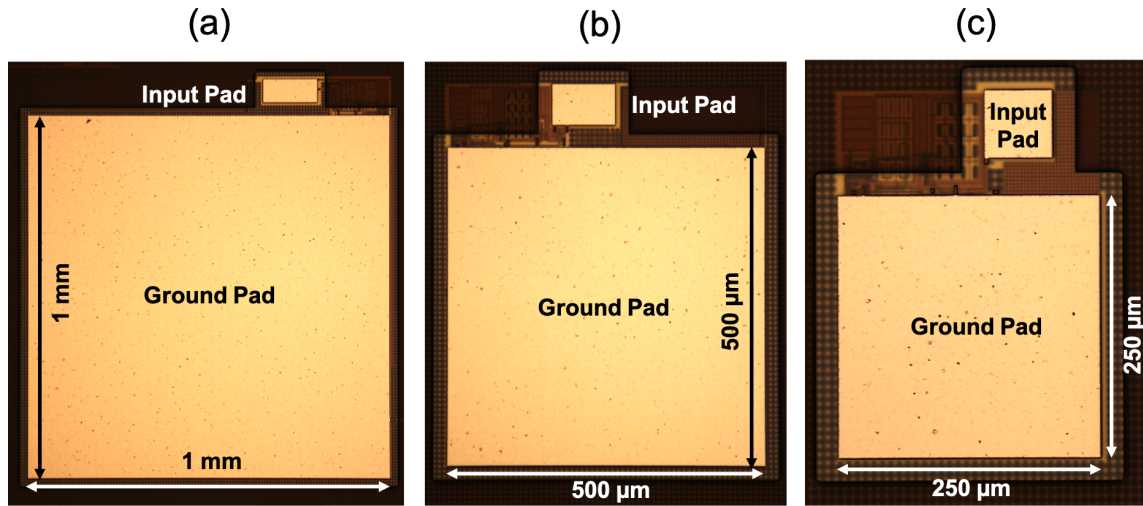


Figure 4.1: (a) The micrograph of one 1.1-mm-by-1-mm chip with the input pad ( $150 \text{ }\mu\text{m} \times 65 \text{ }\mu\text{m}$ ) and the ground pad ( $1 \text{ mm} \times 1 \text{ mm}$ ) labeled; (b) the micrograph of one  $600\text{-}\mu\text{m}$ -by- $500\text{-}\mu\text{m}$  chip with the input pad ( $100 \text{ }\mu\text{m} \times 65 \text{ }\mu\text{m}$ ) and the ground pad ( $500 \text{ }\mu\text{m} \times 500 \text{ }\mu\text{m}$ ) labeled; (c) the micrograph of one  $350\text{-}\mu\text{m}$ -by- $250\text{-}\mu\text{m}$  chip with the input pad ( $65 \text{ }\mu\text{m} \times 65 \text{ }\mu\text{m}$ ) and the ground pad ( $250 \text{ }\mu\text{m} \times 250 \text{ }\mu\text{m}$ ) labeled.

The fabrication approaches for both the PVDF transducers and the PZT transducers start with bulk materials, followed by a subtractive fabrication process to obtain the desired piezoelectric micro-structures. The fabrication procedures are applied at the die level using PVDF or PZT bulk films with sizes similar to the die area. In such a way, the three sizes of chips can be simultaneously integrated with PVDF or PZT micro-structures of the corresponding sizes. Furthermore, the same procedures can be applied at the wafer level by scaling up the sizes of the piezoelectric bulk materials to match wafer sizes.

Similar piezoelectric structures that can be integrated on-chip include the capacitive micromachined ultrasonic transducer (CMUT) [111, 112] and piezoelectric micromachined ultrasonic transducer (PMUT) [113, 114]. However, a CMUT device requires a large DC bias near the so-called collapse voltage [112], which increases the risk of failure of the device [113] and is difficult to produce from my low-voltage sensor chip. On the other hand, a PMUT device typically shows much weaker electromechanical coupling than that of bulk materials [114], which is used here.

To begin the fabrication processes to integrate both the PVDF and PZT transducers, the CMOS chips are planarized by etching away the foundry-deposited passivation layers (polyimide, silicon nitride, and silicon dioxide) to facilitate the subsequent steps, as shown in Figure 4.2. This process is performed with reactive-ion etching (RIE) using a mixture of  $O_2$  and  $SF_6$  plasma [115]. PVDF and PZT integration then follow different fabrication flows (also presented in [72, 110]) specific to their particular properties, which will be addressed in detail in Section 4.2 and Section 4.3, respectively.

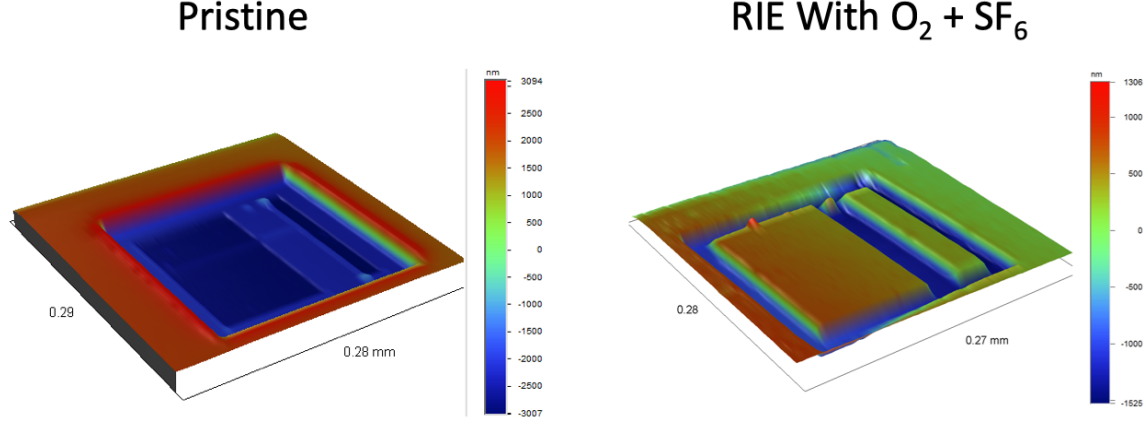


Figure 4.2: The comparison of chip surface before and after removing polyimide.

## 4.2 Integration of PVDF transducers with the sensor chips

### 4.2.1 Microfabrication procedures

PVDF cannot tolerate temperatures greater than 80 °C due to a low Curie temperature. High temperatures can alter the crystal phase of PVDF, resulting in damage to the piezoelectric properties [116]. To examine the effects of temperature treatment on PVDF, three pieces of PVDF were baked at 80 °C, 90 °C, and 100 °C, respectively, with different exposure times from 0 to 5 minutes and measured the  $d_{33}$  after each treatment. As shown in Figure 4.3, the  $d_{33}$  of PVDF was well-preserved at 80 °C but decreased by  $\sim 10\%$  and  $\sim 20\%$  at 90 °C and 100 °C, respectively, after 5 minutes of treatment. As a result, the entire fabrication flow is performed below 70 °C to maintain the piezoelectric properties of PVDF throughout the fabrication [117].

The same poled 33- $\mu\text{m}$  PVDF film as those analyzed in Chapter 3 is used, delivering a mechanical resonance frequency of  $\sim 34$  MHz but usable over a wide frequency range due to its inherently low quality factor. First, the film is to be bonded to the top surface of a CMOS die. However, PVDF has a low surface energy that makes it difficult to adhere to any substrate. Therefore, the film is loaded in a plasma asher

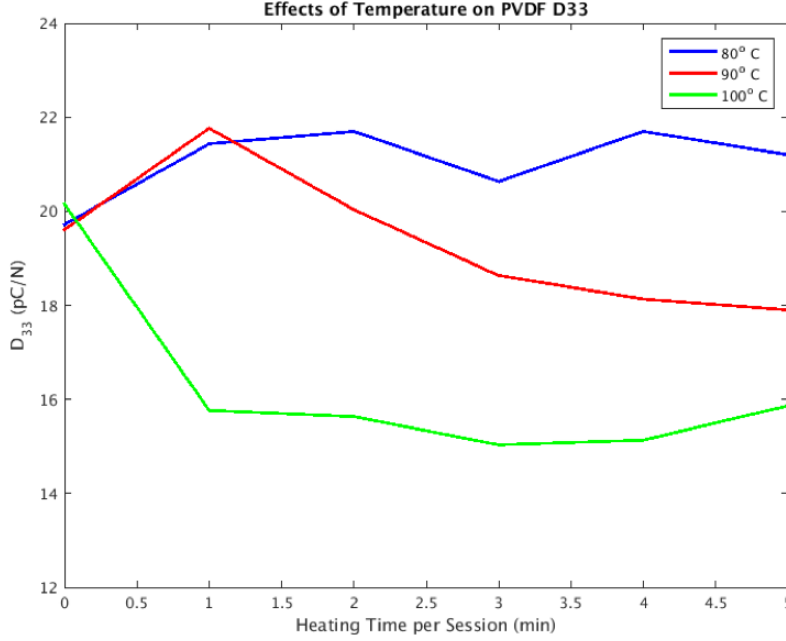


Figure 4.3: Effects of temperature on the  $d_{33}$  of PVDF.

and has its surface treated with  $O_2$  plasma for 5 minutes to enhance the interfacial adhesion [118] prior to the adhesion step. The plasma treatment roughs and also chemically activates the top surface of PVDF and greatly improves the adhesion between PVDF and metal pad to be bonded. The surface roughness before and after the plasma treatment was measured with an atomic force microscope (AFM), as shown in Figure 4.4.

To characterize the promotion of adhesion due to plasma treatment, a tensile test was performed with an electromechanical testing machine (4206, Instron). Both pristine and plasma-treated PVDF pieces were bonded to copper substrates with super glue. The forces required to peel off the PVDF pieces from the corresponding substrates were measured, which indicates the strength of adhesion (Figure 4.5a). The results of the pre-treated piece is shown in Figure 4.5b with a maximum peeling force of around 8 N, much higher than that for pristine PVDF, which was around 0.3 N. Therefore, plasma treatment is necessary to achieve good adhesion for bonding PVDF.

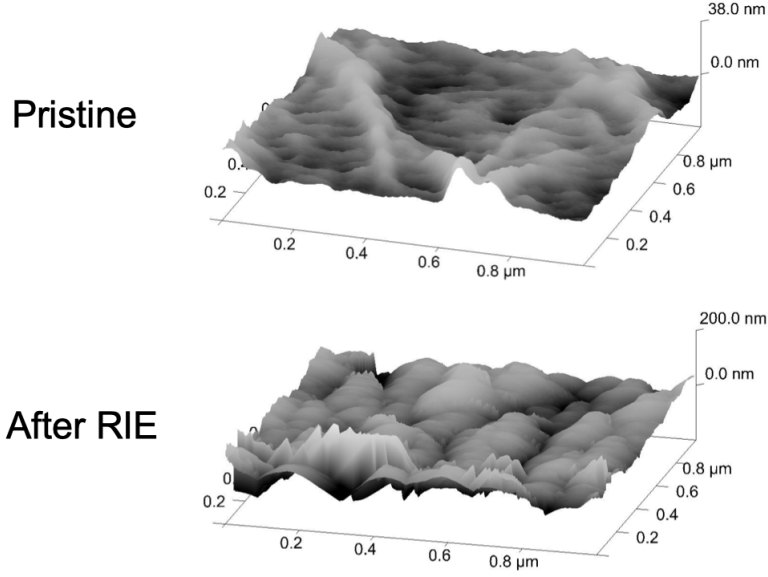


Figure 4.4: Surface roughness of PVDF before and after RIE treatment.

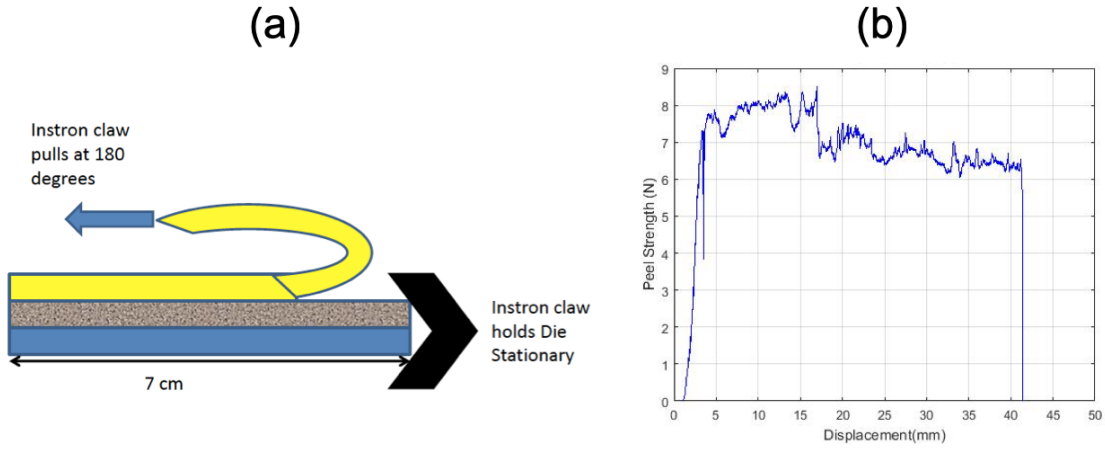


Figure 4.5: The tensile test results of a plasma-treated PVDF piece.

The fabrication flow is summarized in Figure 4.6. After plasma treatment, a 1.6- $\mu\text{m}$ -thick SU-8 2002 adhesive layer is then spun onto the die, bonded to a carrier substrate (Figure 4.6a). While this introduces a series capacitance of  $\sim 1.1$  pF for a 250- $\mu\text{m}$ -by-250- $\mu\text{m}$  area (negligible compared to a  $C_0$  of  $\sim 100$  fF for the PVDF of the same size), the more preferable anisotropic conductive adhesives cannot be applied because they typically require curing temperatures above 100  $^{\circ}\text{C}$ . The substrate is then flipped over and gently placed on the pre-treated PVDF film, baked at 70  $^{\circ}\text{C}$  for 30 minutes, and flipped back to be UV cured (Figure 4.6b).

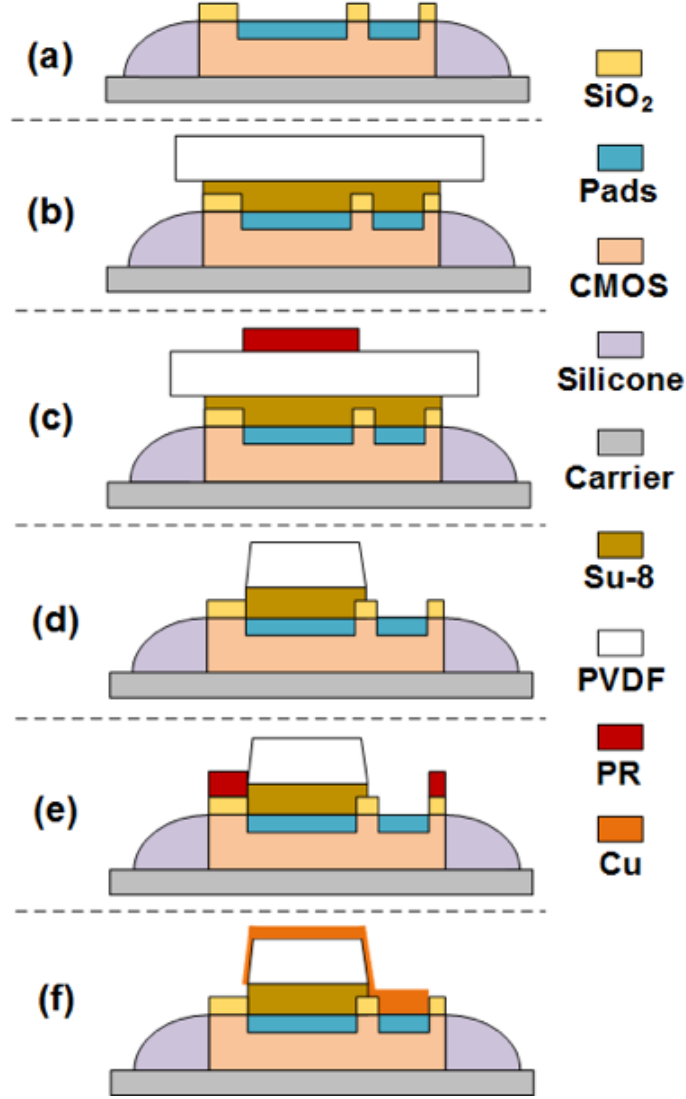


Figure 4.6: Fabrication flow for integrating PVDF with the CMOS chips. (a) Removal of polyimide and bonding of the CMOS die to a carrier with PMMA and silicone and (b) adhesion of pre-treated PVDF piece and the die with SU-8 and (c) patterning of PVDF areas on top of the chip signal pads and (d) RIE etching to create PVDF micro-structures and (e) patterning of chip areas and (f) metal deposition and lift-off for ground connection.

The now-exposed PVDF top surface is also treated with O<sub>2</sub> plasma and a  $\sim 10\text{-}\mu\text{m}$  layer of AZ-4620 photoresist (PR) is spun, followed by a baking step at 70 °C for 80 minutes. The same spinning-and-baking process is repeated two more times to create a  $\sim 30\text{-}\mu\text{m}$ -thick PR layer. Standard UV photolithography is applied to create PR patterns, used as etch masks, above the ground pads (Figure 4.6c). RIE



etching of the PVDF [119] and the underlying SU-8 layer is used to define the PVDF micro-structures (Figure 4.6d) with the bottom terminals connected to the ground pads.

Photolithography with a  $\sim 6\text{-}\mu\text{m}$  layer of AZ-4620 is performed to cover the entire die except the active chip area (Figure 4.6e). DC sputtering is used to deposit a 9-nm layer of Cr and a  $1.2\text{-}\mu\text{m}$  layer of Cu onto the die. Sputtering is used to provide sufficient sidewall coverage. Finally, the Cu over the PR layer is removed with a lift-off process, leaving Cu connection between the top terminals of the PVDF structures and the input pads (Figure 4.6f).

The micrographs of the three sizes of fabricated PVDF micro-structures after Step (d) in Figure 4.6 is displayed in Figure 4.7. In addition, the micrographs of the fully-integrated chips of varying sizes are presented in Figure 4.8, showing the micro-fabricated PVDF transducers mechanically and electrically connected to the sensor chips. These transducers maintain their  $d_{33}$  values of  $\sim 19\text{ pC/N}$ , as measured with a  $d_{33}$  meter (PM300, Piezotest).

As a final step, the fully fabricated dies are diced to separate the fully-integrated chips. The chip-separation process is performed by loading one die at a time to

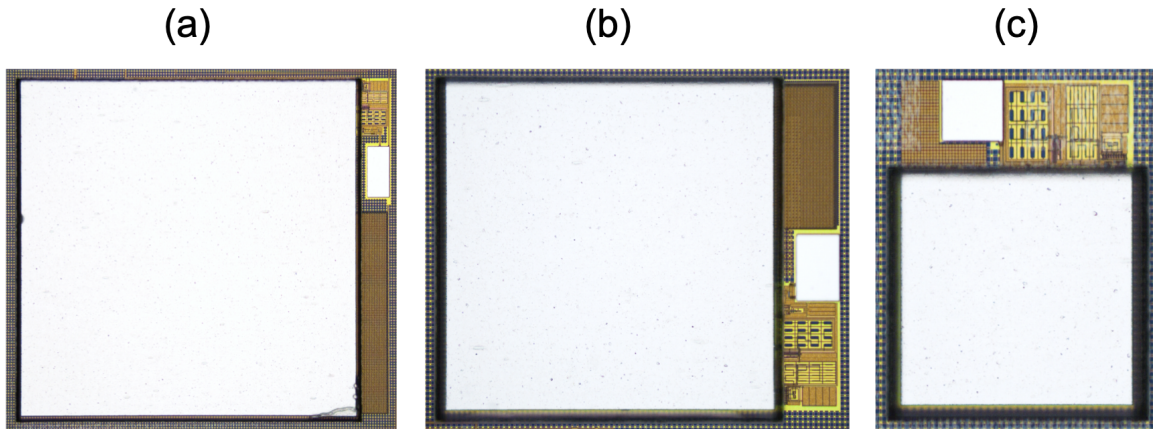


Figure 4.7: (a) A PVDF micro-structure integrated with the ground pad of a 1.1-mm-by-1-mm chip;(b) a PVDF micro-structure integrated with the ground pad of a  $600\text{-}\mu\text{m}$ -by- $500\text{-}\mu\text{m}$  chip; (c) a PVDF micro-structure integrated with the ground pad of a  $350\text{-}\mu\text{m}$ -by- $250\text{-}\mu\text{m}$  chip.

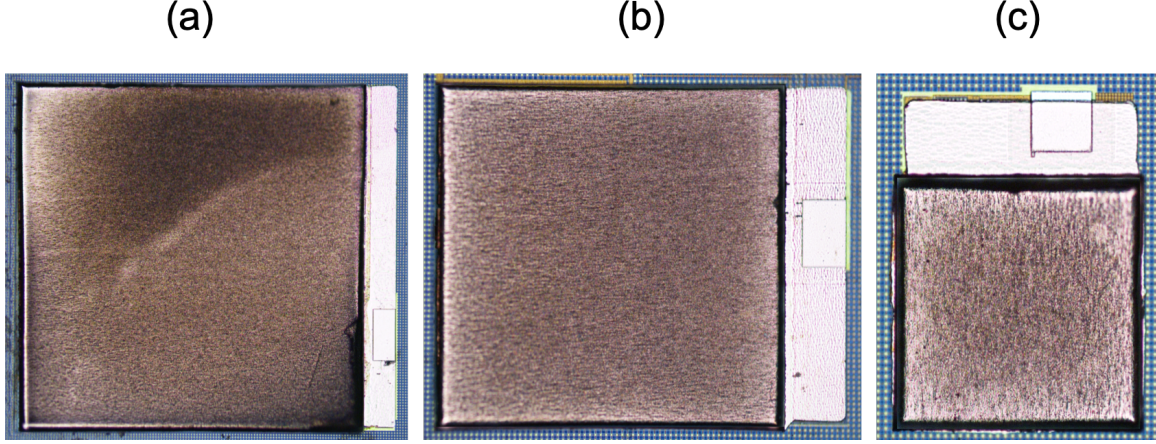


Figure 4.8: (a) A fully-fabricated PVDF micro-structure integrated with a 1.1-mm-by-1-mm chip; (b) a fully-fabricated PVDF micro-structure integrated with a 600- $\mu\text{m}$ -by-500- $\mu\text{m}$  chip; (c) a fully-fabricated PVDF micro-structure integrated with a 350- $\mu\text{m}$ -by-250- $\mu\text{m}$  chip.

the dicing saw. The die is first carefully adhered to a piece of ultraviolet (UV) releasable tape and covered with another piece of UV tape (the nonadhesive side makes contact with the die to not stick to the fabricated chips) to create a sandwich structure that protects the die in the middle from flying away during the dicing. Subsequently, the die is diced horizontally to separate the chips according to their sizes. In the end, each diced slice that contains chips with the same size, is further diced to separate the individual chips into individual sensing motes. Figure 4.9 shows the three sizes of standalone sensing motes placed on a finger tip to demonstrate their relative dimensions.

#### 4.2.2 Characterization results

The micro-fabricated PVDF structures were characterized with Raman spectroscopy and compared against pristine PVDF film to examine the effects of microfabrication on the piezoelectric properties of PVDF. The pristine PVDF film was adhered to an identical CMOS IC die using SU-8 to maintain the same substrate as the micro-fabricated PVDF structures for comparison. Raman spectroscopy was performed

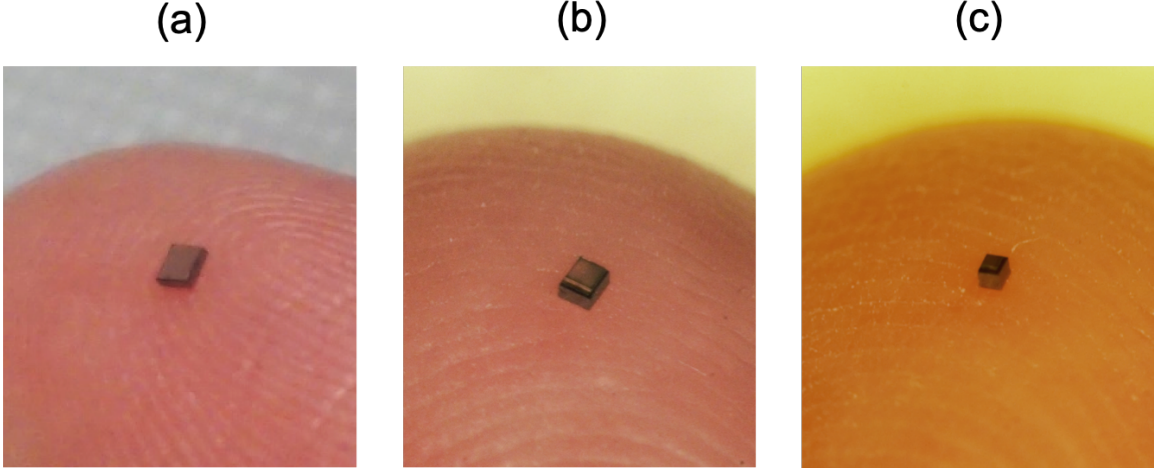


Figure 4.9: (a) A 1.1-mm-by-1-mm standalone sensing mote; (b) a 600- $\mu\text{m}$ -by-500- $\mu\text{m}$  standalone sensing mote; (c) a 350- $\mu\text{m}$ -by-250- $\mu\text{m}$  standalone sensing mote.

using a Raman spectroscope (InVia, Renishaw) with 532-nm laser with an exposure of 30 s. The background spectrum due to the IC substrate was subtracted from the absorbance measurements to obtain the spectrum of interest corresponding to PVDF. The micro-fabricated PVDF shows almost the same Raman spectrum as the pristine PVDF with the intensity peak in PVDF absorbance at  $1430\text{ cm}^{-1}$  [120] and particularly the characteristic peaks of the  $\beta$ -phase at  $511\text{ cm}^{-1}$ ,  $840\text{ cm}^{-1}$ , and  $1279\text{ cm}^{-1}$  (Figure 4.10) [120–123], demonstrating the preservation of piezoelectric properties during the fabrication processes. It did not show obvious peaks corresponding to the  $\alpha$ -phase ( $408, 531, 612, 765, 796, 855, \text{ and } 976\text{ cm}^{-1}$ ) [122, 123], which would appear if the piezoelectricity was damaged during the fabrication.

Additionally, AFM was used to measure the surface morphology of the fabricated piezoelectric transducers under voltage excitation [63]. Figure 4.11a shows the roughness of the PVDF top surface to be close to 100 nm in the absence of voltage excitation. 10-V square wave excitation at 1 Hz and 10 Hz, however, resulted in observable mechanical oscillations in the AFM that scanned at 1 Hz (Figure 4.11b and Figure 4.11c).

Due to the inherently poor dielectric properties (resulting in high input impedance

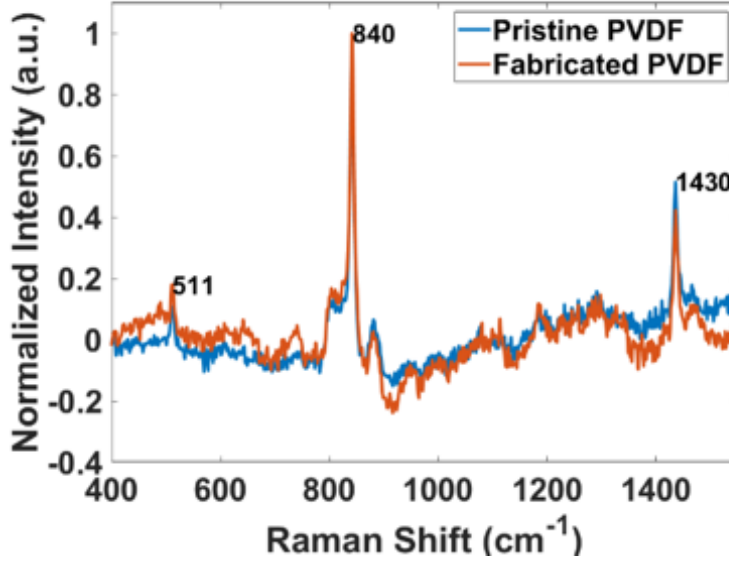


Figure 4.10: Raman spectrum of one micro-fabricated PVDF structure in comparison with a pristine PVDF piece.

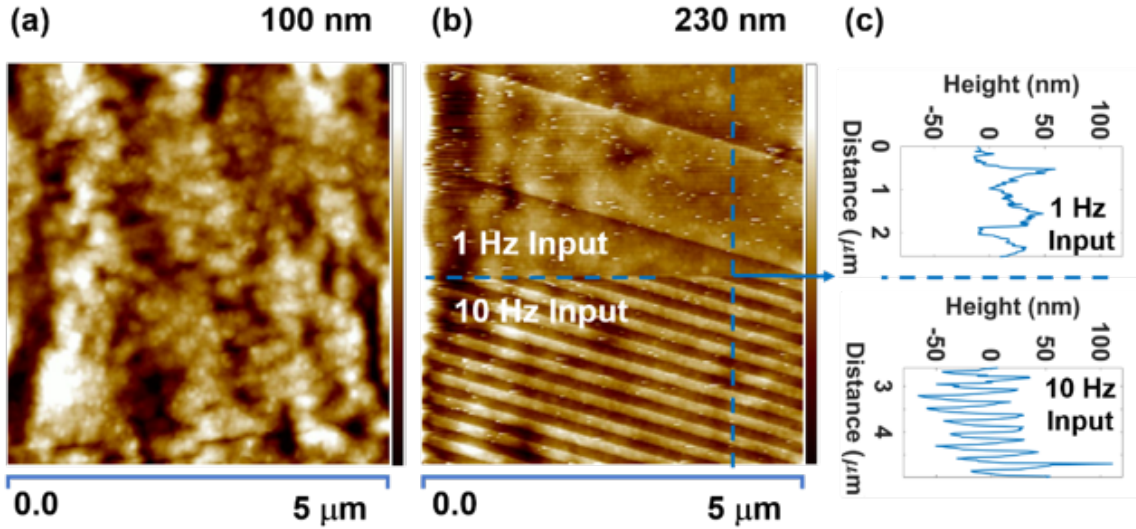


Figure 4.11: AFM measurements on a fabricated PVDF structure (a) without voltage excitation and (b) with 1-Hz and 10-Hz 10-V peak-to-peak square wave excitations; (c) a height plot along a vertical line on (b).

and dielectric loss and low power-harvesting efficiency) and weak piezoelectric activity of PVDF (a low electromechanical coupling coefficient of  $\sim 0.2$  [81] and an extremely low  $d_{33}$  value of  $\sim 19$  pC/N in comparison to that of  $\sim 650$  pC/N for PZT), no satisfactory results were obtained when I attempted to power up these micron-scale

notes with integrated PVDF transducers using an ultrasound source. As a result, I switched gears to develop and implement the microfabrication techniques to integrate PZT with the same CMOS chips, as presented below.

## 4.3 Integration of PZT transducers with the sensor chips

### 4.3.1 Microfabrication procedures

PZT, in comparison to PVDF, has a Curie temperature of 225 °C and can tolerate temperatures as high as 150 °C, which relieves the temperature requirement during the fabrication process. However, the processing temperature is still kept below 100 °C to keep a proper margin [124].

Similar to the PVDF-integration process, PZT transducers are directly fabricated on the chips with the top and bottom terminals of these transducer electrically connected to the input and ground pads, respectively. The fabrication procedures, which were co-developed with Dr. Tiago Costa, are demonstrated in Figure 4.12, where the PZT micro-structures are patterned using a mechanical dicing process [125, 126], which provides a much faster etch rate than RIE for the PZT thickness used in this work.

The fabrication flow, using the fabrication for a 350- $\mu\text{m}$ -by-250- $\mu\text{m}$  chip as an example, begins with a 7.24 cm  $\times$  7.24 cm  $\times$  267  $\mu\text{m}$  sheet of bulk PZT material, same as the one analyzed in Chapter 3. First, the nickel plating that comes with the PZT material is stripped using ferric chloride for 5 s, exposing the PZT surface. Photolithographic patterning with AZ-1512 PR is used to define arrays of 300  $\mu\text{m}$   $\times$  300  $\mu\text{m}$  openings on the top side of the PZT sheet, followed by electron-beam evaporation of a 10-nm chromium (Cr) layer and a 50-nm gold (Au) layer (Figure 4.12a). Lift-off in acetone is subsequently performed to create contacts that match



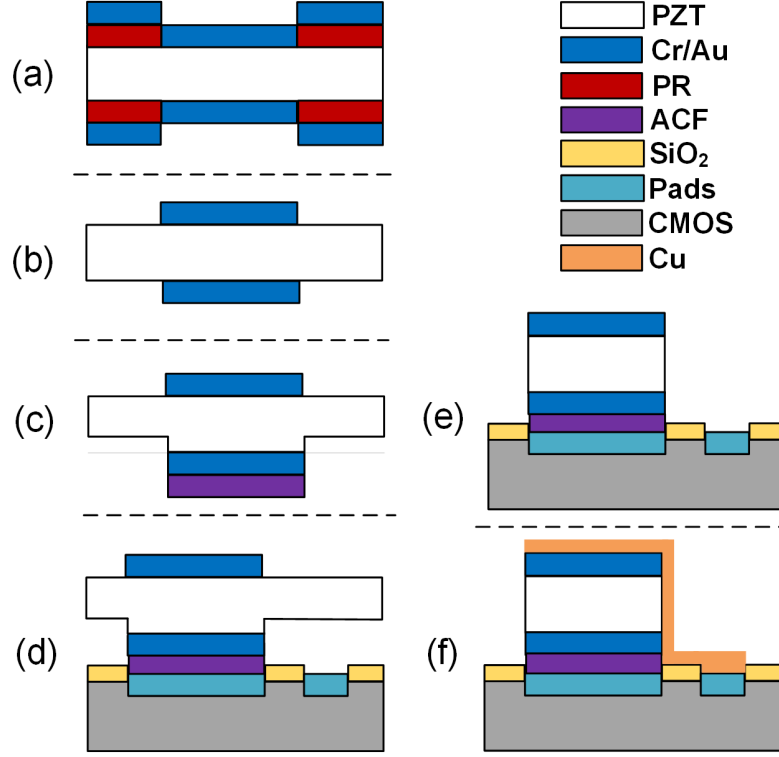


Figure 4.12: The fabrication procedures for monolithically integrating the CMOS chips with PZT transducers, including (a) photolithographic patterning and Cr/Au deposition, and (b) lift-off of PR to create contacts on both sides of the PZT that match with the ground pads on CMOS chips, and (c) adhesion of the ACF with the bottom side of the PZT and dicing of the PZT from the bottom side, and (d) bonding of the PZT to the CMOS chips with precise alignment, and (e) dicing of the PZT from the top side to create free-standing PZT transducers, and (f) deposition of copper to connect the top sides of the PZT transducers with the corresponding input pads.

the ground pads of the CMOS chips (Figure 4.12b). The same process is applied to the bottom side of the PZT sheet to create vertically aligned contacts on both sides.

The sheet is then diced into  $4 \text{ mm} \times 3.2 \text{ mm}$  pieces using the dicing saw. A piece of anisotropic conductive film (ACF, TFA220-8, H&S High Tech) of the same size is then placed on the bottom side of a diced PZT piece. A sub-micron-resolution die-bonder (Fineplacer Lambda, Finetech) is used to apply 0.1 N of force to the ACF at  $80^\circ \text{C}$  for 5 s, adhering the ACF to the PZT piece. The PZT piece is then partially diced from its bottom side to a thickness of  $\sim 60 \mu\text{m}$  into the PZT (Figure 4.12c). It is then precisely aligned and bonded to a CMOS die through the ACF by applying a

100-N force at 150 °C for 5 s with the die-bonder (Figure 4.12d), such that the metal contacts on the PZT piece are electrically connected to the corresponding pads on the CMOS die. The conductive particles in the ACF only allow conduction vertically through the metal contacts and not laterally in a manner that would short the pads together.

The remainder of the PZT piece outside of the pad areas for each chip is then diced away, leaving free-standing PZT transducers built on top of the CMOS die (Figure 4.12e). To form the top contact, photolithography with AZ-4620 PR is performed to mask the entire die except for the chip areas, followed by DC sputtering of a 9-nm layer of Cr and a 1.2- $\mu\text{m}$  layer of copper. After a lift-off process that removes the metal outside of the chip areas, the top side of each PZT transducer is electrically connected to the corresponding rectifier input pad of each chip (Figure 4.12f).

The micrographs after each of the fabrication steps illustrated in Figure 4.12c–Figure 4.12f are shown in 4.13a–4.13d, respectively. Finally, to provide biocompatibility, the fully-integrated chips are completely encapsulated with an 8- $\mu\text{m}$ -thick, biocompatible parylene film deposited with a parylene deposition system (Labcoater 2, Specialty Coating Systems Inc.).

The thickness of the parylene film for encapsulation is crucial for the durability of the integrated chips. If the parylene film is too thin, it can get worn and damaged easily in the reactive *in vivo* environment, exposing the chips and transducers to cause electrical leakage and performance degradation [127], whereas a thick layer of parylene film offers excellent isolation and protection of the chips from the surrounding environment and ensures high device resilience and robustness. However, if the film is too thick, the ultrasound will be significantly dampened and attenuated because of the strong damping and attenuation effects of the encapsulation film [127]. The film thickness needs to be carefully chosen for a trade-off between the mechanical robustness and the ultrasound transmission. Therefore, 8- $\mu\text{m}$ -thick parylene is used to provide reliable device passivation at a thickness significantly less than the ultra-

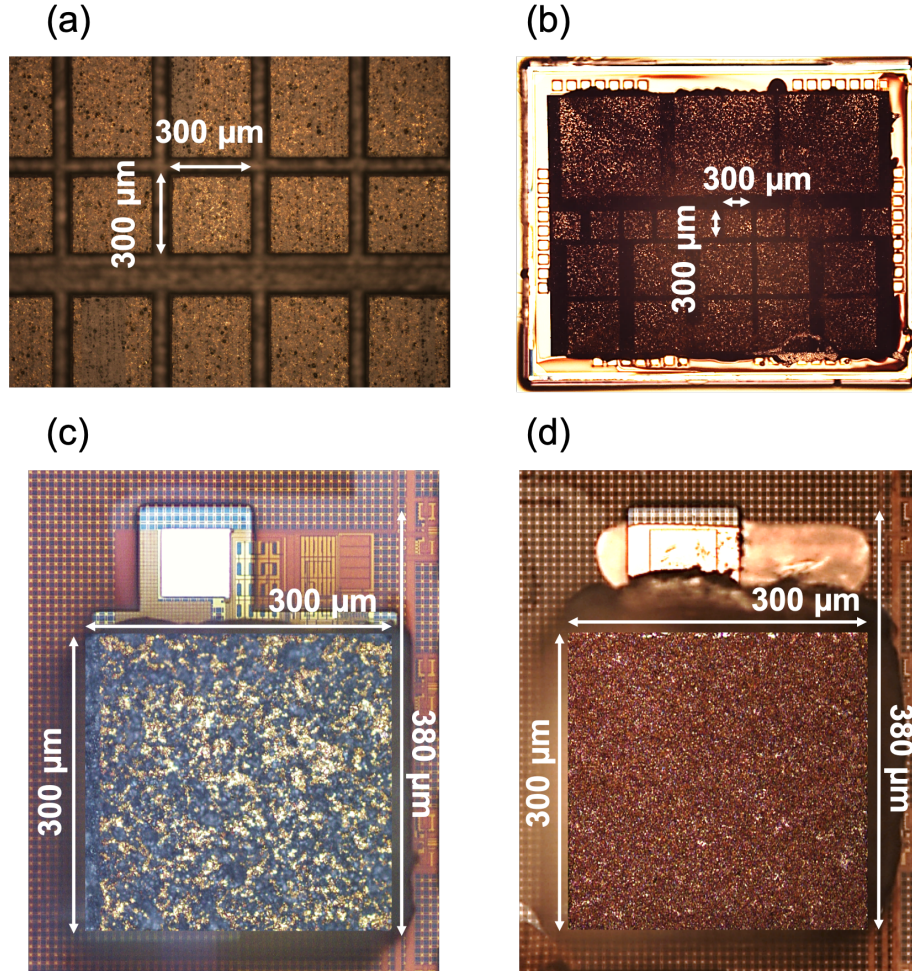


Figure 4.13: The microphotograph of the major fabrication procedures for monolithically integrating the CMOS chips with PZT transducers: (a) after bottom-side dicing; (b) after bonding the PZT die with the CMOS die; (c) after the top-side dicing; (d) after metal deposition for the top-side connection.

sound wavelength at our operating frequency, minimizing acoustic losses. Up until this step, ten  $250\text{-}\mu\text{m}$ -by- $250\text{-}\mu\text{m}$  PZT transducers are monolithically integrated with their corresponding chips on a single die.

Furthermore, some of the fully-fabricated dies, prior to receiving the parylene coating, are diced to separate the fully-integrated chips into individual notes for fully-wireless testing without any wiring or cables, as shown in Figure 4.14a. The same dicing procedures to separate the PVDF-integrated chips are used here to separate these PZT-integrated chips. An exploded-view schematic illustration of the mote



with the major components labeled is shown in Figure 4.14b. Finally, to complete the fabrication flow, these standalone motes are also coated with 8- $\mu\text{m}$ -thick parylene films for encapsulation.

Micrographs taken with a standard optical microscope and a scanning electron microscope (SEM) of a fully-integrated and released standalone mote sized  $380\ \mu\text{m} \times 300\ \mu\text{m} \times 570\ \mu\text{m}$  are shown in Figure 4.14c and Figure 4.14d, respectively. The SEM image was taken on an FEI Nova NanoSEM 450 Scanning Electron Microscope. The sample was prepared by mounting the mote to a glass cover slip ( $25\ \text{mm} \times 25\ \text{mm} \times 0.2\ \text{mm}$ ) with double-sided Kapton tape. To prevent charging of the surface, a Cressington 108 Sputter coater was used to deposit a conformal 6-nm layer of gold. This was then imaged in the SEM at a working distance of 4.9 mm from the surface, with an acceleration voltage of 5 kV. The spot size was 18  $\mu\text{m}$ , and the image was taken in secondary electron imaging mode, using the Everhartt-Thornley Detector. The scanning dwell time was set to 1  $\mu\text{s}$ . In addition, a mote placed on a United States penny and a United States dime with different orientations are displayed in Figure 4.14e and Figure 4.14f, respectively, to illustrate the relative size scale.

### 4.3.2 Characterization results

Two oscillators were measured before and after the fabrication procedures, showing a marginal changes ( $\sim 0.24\%$ ) in frequency at room temperature, demonstrating the preservation of the circuit functionality and performance throughout the fabrication process. In addition,  $d_{33}$  measurements for a PZT sample before and after fabrication showed only a 7% loss [110]. Detailed characterization of these fully-fabricated chips will be discussed in Chapter 5.

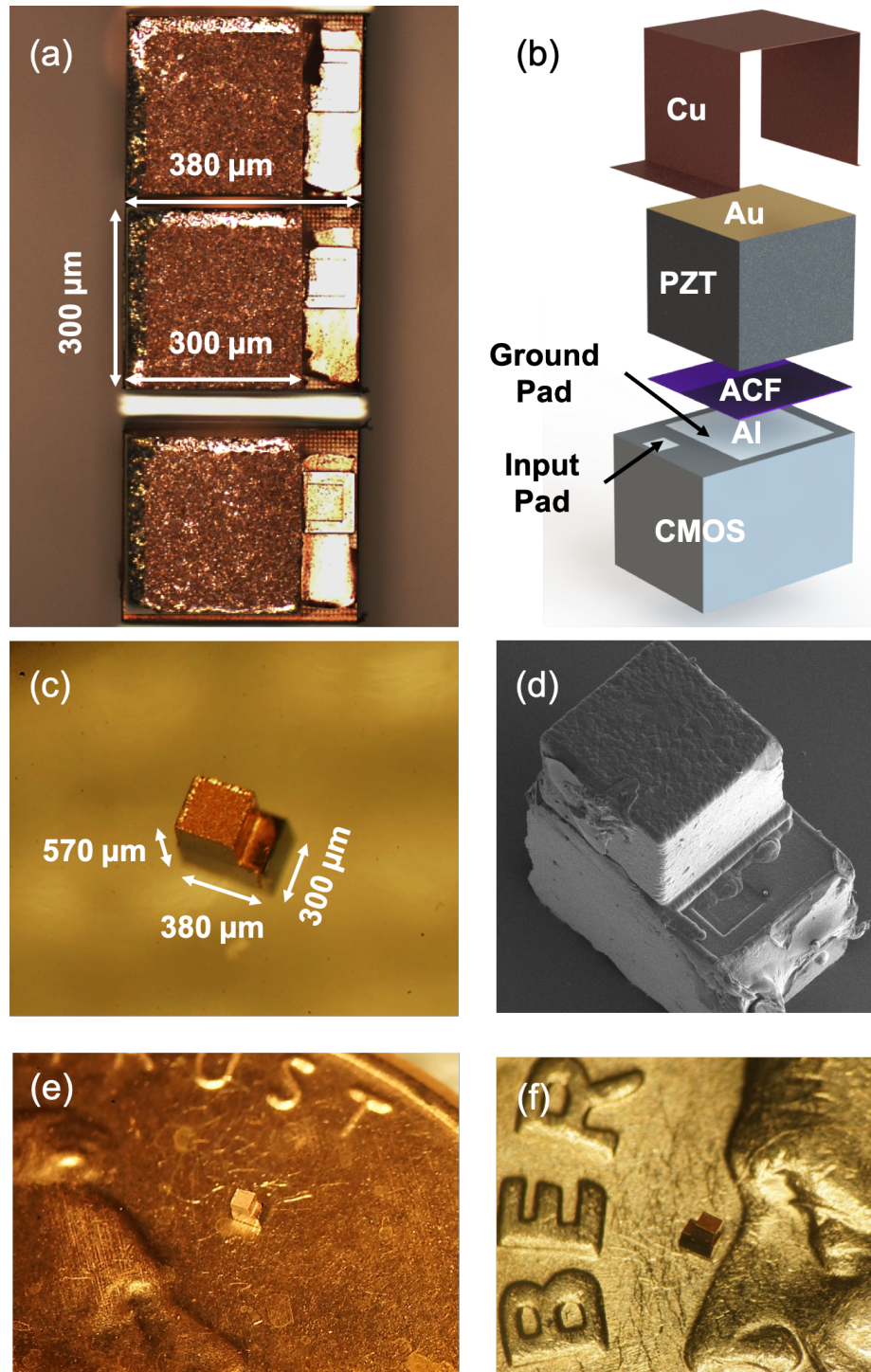


Figure 4.14: (a) Fully-integrated chips separated through a dicing process; (b) an exploded-view schematic illustration of the major components of a fully-integrated and released standalone mote, including the CMOS temperature sensor chip with the two exposed Al pads, the microscale PZT transducer covered in Cr/Au on both sides, the ACF, and the Cu layer; (c) a detailed photograph of the mote with dimensions; (d) an SEM image of the mote; (e) the mote placed on top of a United States penny; (f) the mote placed on top of a United States dime with a different orientation as in (e).

---

## Chapter 5

# Experimental Validation of the Temperature Sensing Motes

---

Following the microfabrication procedures to monolithically integrate the transducers and the sensor chips, the PZT-integrated motes were thoroughly tested in both an *in vitro* environment using chicken tissues and an *in vivo* environment using a mouse model. Specifically, the temperature sensing performance of three fully-integrated motes prior to their separations from the dies were tested *in vitro* with an ultrasound source by wire-bonding the motes to custom printed circuit boards (PCBs). Three standalone motes released from the corresponding dies were then characterized with an ultrasound input fully-wirelessly in an *in vitro* setting. Finally, the standalone

motes were implanted into different locations of mice to evaluate their *in vivo* sensing performance.

## 5.1 *In-vitro* characterization with the wire-bonded motes

### 5.1.1 Board design and wire-bonding

First, three fully-integrated motes unreleased from the die were characterized acoustically with an ultrasound input to evaluate their temperature sensing performance. For this test, a custom PCB was developed to measure the outputs from the major circuit blocks. The schematic of the PCB is shown in Figure 5.1a, which contains

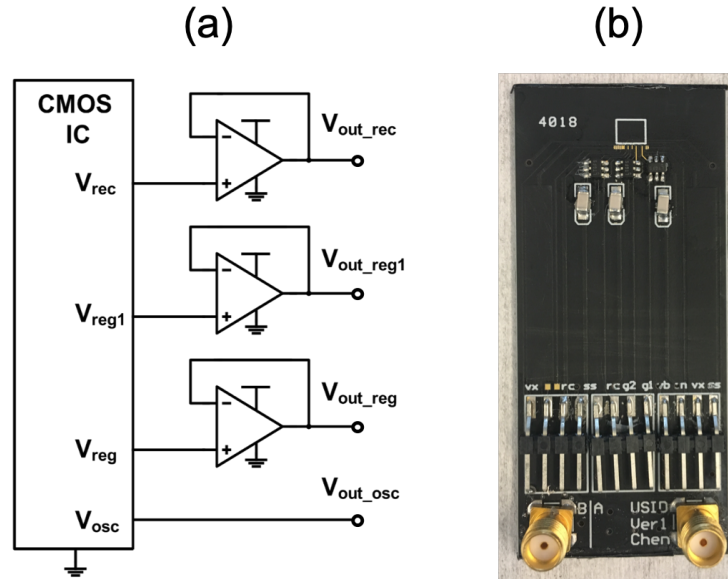


Figure 5.1: (a) The schematic of the testing board; (b) a populated testing board.

unity-gain buffers for viewing the output voltage waveforms of the rectifier, the voltage regulators, and the oscillator during circuit operation. The populated board is shown in Figure 5.1b, where the inputs to the circuit and rectifier output and regu-

lator outputs can be accessed through header pins and the oscillator output can be viewed from sub-miniature version A (SMA) connectors.

Each die was wire-bonded to a testing board so that the internal nodes of interests of the chip can be accessed and electrically interfaced from the outside. The die was attached to the board with a thin layer of polymethyl methacrylate (PMMA) (Figure 5.2a), followed by an in-house wire-bonding process (Figure 5.2b) performed at a low temperature of 80 °C to not impair the piezoelectric properties of the on-chip PZT structures. The die wire-bonded to the board is shown in Figure 5.2c with a micrograph of the wire-bonded mote shown in Figure 5.5a.

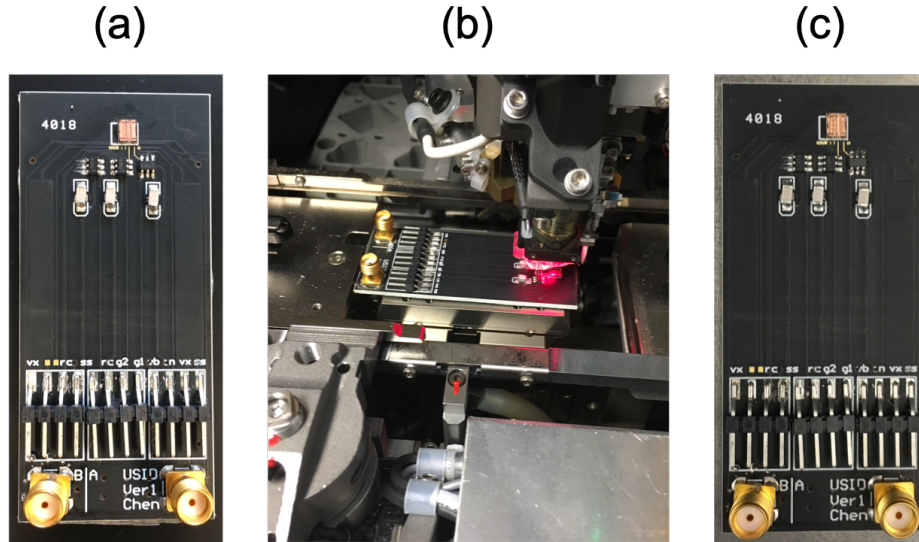


Figure 5.2: (a) A testing board with a chip attached for wire-bonding; (b) the wire-bonding process; (c) the board with the chip wire-bonded to it.

Prior to the acoustic testing, the PSRR was measured separately for both the first-stage and second-stage regulators of a wire-bonded mote from 1 kHz to 20 MHz. The PSRR results were obtained using the “Power Supply Rejection Ratio (PSRR)” function within the “Power Analysis” module of a mixed-signal oscilloscope (MSOX4054A, Keysight), as shown in Figure 5.3. An AC input swept from 1 kHz to 20 MHz from the oscilloscope was superimposed on a clean DC voltage from an external power supply (GS200, Yokogawa) through a bias tee (5575A, Picosecond Pulse Labs) with



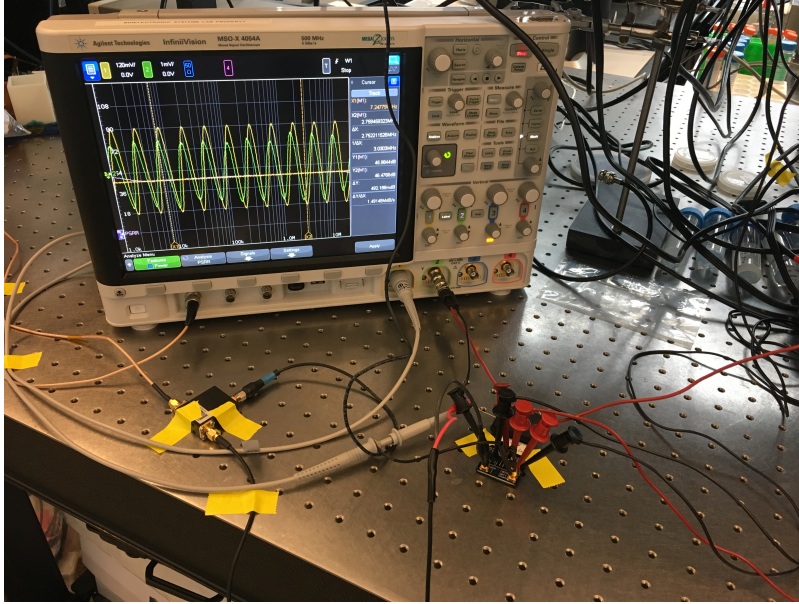


Figure 5.3: The setup for PSRR measurements.

a -3 dB bandwidth of 10 kHz to 12 GHz. This combined signal was fed into the input of each regulator to provide a DC bias and also an AC noise component to the regulator. This input and the resulting output from the regulator were measured with two channels of the oscilloscope, respectively. The PSRR were computed with the oscilloscope by dividing the input ripple by the output ripple for each swept frequency value.

The two regulators yield a combined PSRR of  $\sim 83.9$  dB at the ultrasound frequency of 8.3 MHz (Figure 5.4), demonstrating that the interference and noise from the ultrasound source is effectively rejected by the regulators.

Figure 5.5b demonstrates the experimental setup for testing one of the wire-bonded motes. The PCB with the wire-bonded mote was inserted into an opaque case to eliminate the effects of light on circuit operation. The case was filled with DI water for ultrasound transmission and placed on a hot plate with controlled temperature. A PT-1000 temperature probe in the water bath was used for feedback temperature control. The water temperature was also monitored with a high-accuracy digital thermometer (HH376, Omega Engineering) as the reference temperature through-

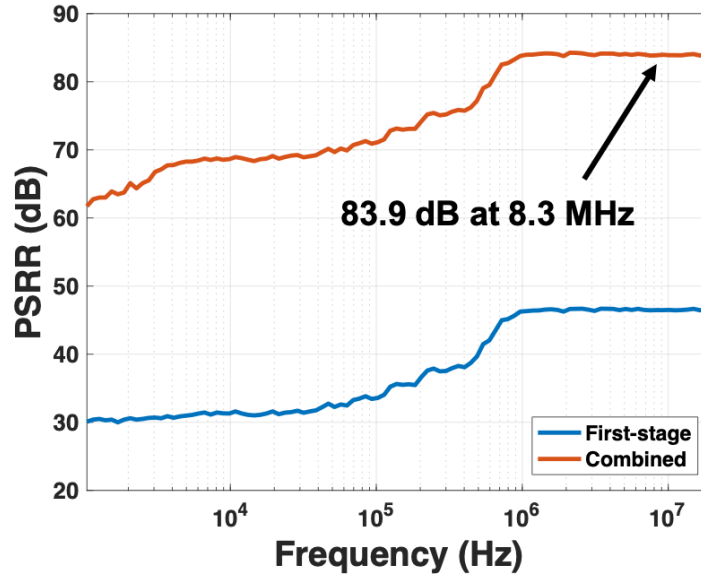


Figure 5.4: PSRR measurements for both regulators.

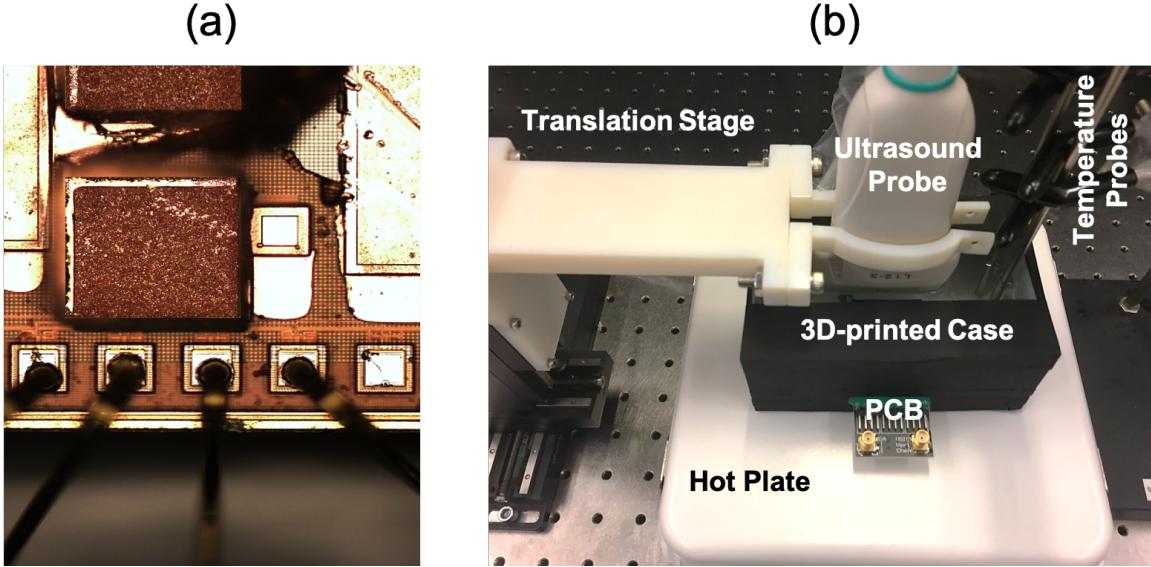


Figure 5.5: (a) A fully-fabricated mote wire-bonded to a board; (b) the experimental setup consisting of the PCB inserted into a 3D-printed case filled with DI water for testing the performance of the mote.

out the experiments. The L12-3v ultrasound probe, which contains 192 elements with a pitch of 200  $\mu\text{m}$  and an elevation focus of 20 mm [128], was controlled by a translation stage (Thorlabs, Newton, NJ) to move in three-dimensions (3D) and positioned 22 mm (limited only by the measurement setup) above the mote for power

and communication.

### 5.1.2 Ultrasound interface

Custom programs were developed in MATLAB for the Vantage 256 system (Figure 5.6, adapted from [129]) to interface with the sensing motes. A B-mode imaging script is first used to precisely locate the mote. A sub-section of 128 elements on the probe scan as a linear phased array. These are organized into 192 scan lines, segmented such that each line reconstructs a  $133\text{-}\mu\text{m}$ -wide region. The transmitted waveform is one cycle of pulse at 8.3 MHz with an on-time of  $\sim 120.5\text{ ns}$  repeated every  $160\text{ }\mu\text{s}$ , which is the pulse repetition period. A reconstructed B-mode image can be produced approximately every 40 ms, resulting in a frame rate of approximately 25 frames/s.

Once the mote is located, the software switches to a different mode, in which ultrasound is focused directly onto the mote with a  $0^\circ$  incident angle to activate the mote and process the backscattering data. Again, 128 of the 192 transducer elements on the probe are used. In this case, the ultrasound waveform consists of pulses with a pulse repetition period of  $100\text{ }\mu\text{s}$ . Each pulse is four cycles of an 8.3-MHz signal



Figure 5.6: The Verasonics Vantage Research Ultrasound System.



with an on-time of  $\sim 481.9$  ns, such that the duty cycle of the ultrasound signal is approximately 0.48%. As shown in Figure 5.7, the waveform at the location of the mote was measured using the hydrophone, where the peak pressure amplitude was found to be  $\sim 305$  kPa, resulting in a spatial-peak temporal-average intensity ( $I_{SPTA}$ ) of  $\sim 0.149$  mW/mm<sup>2</sup> calculated as the time-averaged intensity at the focal spot. Four cycles of pulses are found to be optimal with the lowest  $I_{SPTA}$  for delivering sufficient power to the mote, as demonstrated in Figure 5.8.

This ultrasound waveform successfully powered up the mote by delivering  $\sim 9.3$   $\mu$ W of power to the mote, resulting in an acoustic-to-electrical conversion ratio from the ultrasound source to the mote of  $\sim 0.28\%$ , similar to the results presented in [76] for ultrasonic devices at the 100- $\mu$ m scale. The output voltage waveforms of the rectifier, the two regulators, and the oscillator measured at 37 °C are shown in Figure 5.9. The rectifier and the two regulators had voltages of  $\sim 1.5$  V,  $\sim 0.65$  V, and  $\sim 0.45$  V, respectively, and the oscillator ran at  $\sim 7.6$  Hz. The second-stage regulator shows slightly larger ripple than the first-stage because the second-stage directly drives the oscillator which introduces current transients during transitions. However, this ripple ( $< 50$  mV in amplitude) is tolerable since it results in a less-than-120-ppm change in

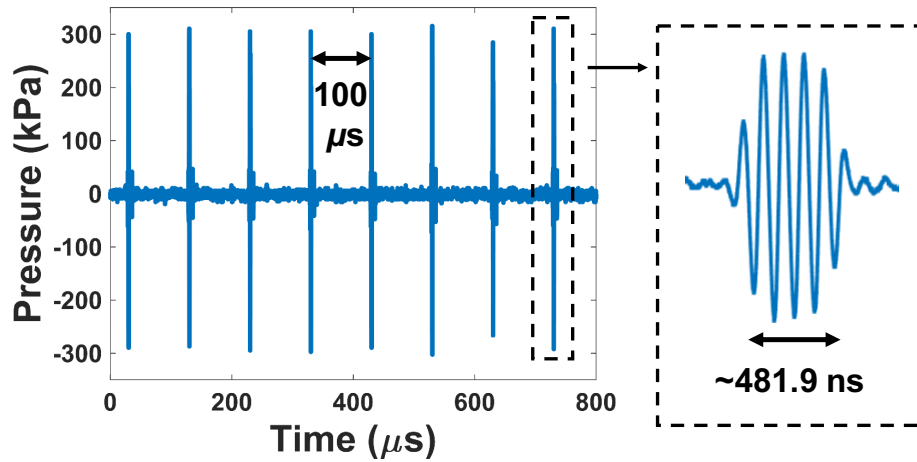


Figure 5.7: The waveform of the ultrasound used to power the mote, showing a pressure amplitude of  $\sim 305$  kPa with a 100  $\mu$ s pulse repetition period.

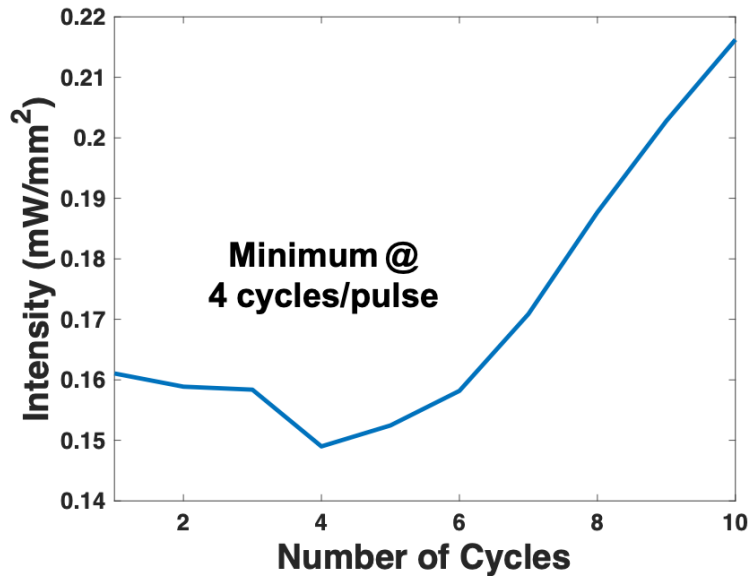


Figure 5.8: The ultrasound intensity to activate the mote with respect to the number of cycles in each pulse.

the period jitter of the oscillator.

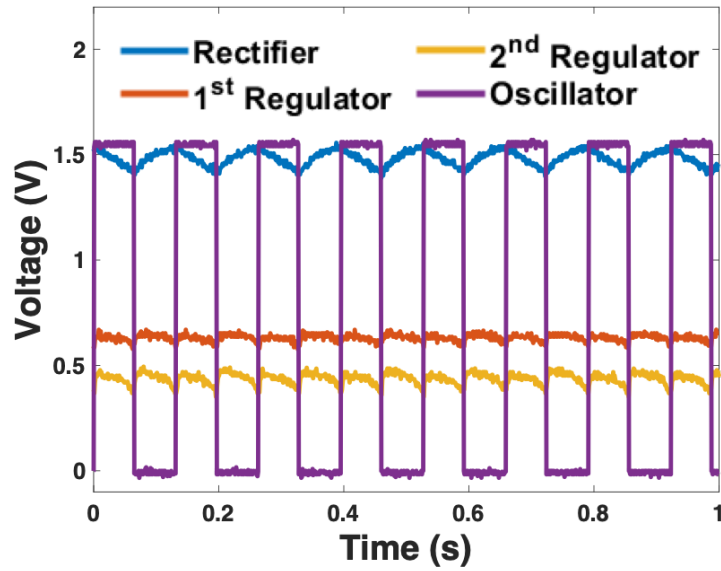


Figure 5.9: The output voltage waveforms of the rectifier, the two regulators, and the oscillator from testing of a wire-bonded mote with an ultrasound input at 37 °C, showing an oscillation frequency of  $\sim 7.6$  Hz.

### 5.1.3 Data acquisition and analysis

To obtain the acoustic backscattering data containing the temperature information, the reflected ultrasound echoes for each transmitted pulse are received by the 128 elements of the probe at two samples per wavelength for a total of 896 samples. Each sample corresponds to 60.24 ns of round-trip travel time of ultrasound, translating to a depth resolution of 46.4  $\mu\text{m}$  at a maximum depth of 41.6 mm with 896 samples. The peak amplitude of the echoes is stored as one frame of backscattering data. 12800 temporally consecutive frames, each separated by the pulse repetition period of 100  $\mu\text{s}$ , are acquired to produce 1.28 s of data. This leads to a minimum detectable change in the oscillation period of 100  $\mu\text{s}$  (limited by the Vantage 256 system and comparable to the jitter of the oscillator) and a sampling rate of 10 kHz, which, together with the jitter of the oscillator, determines the sensitivity of the temperature measurements. A Fourier transform is performed on the acquired data picked up by each element at each depth until the distinct frequency that carries the temperature information is detected. Two examples of the acoustic data obtained at 27 °C and 50 °C are shown in the left of Figure 5.10a and Figure 5.10b with an oscillation frequency of 4.4 Hz and 18.6 Hz, respectively.

To determine the high-to-low and low-to-high transitions of the oscillator, the difference between adjacent time-points in the data is calculated. Events in this signal are determined by setting a threshold for magnitudes larger than 2 kPa. The mean magnitude of these events is taken as the average signal, while the standard deviation of the remaining difference values is taken as the rms noise. The SNR is calculated as this average signal divided by this rms noise. As shown in Figure 5.10a and Figure 5.10b, the SNR values are 25.05 dB and 28.04 dB, respectively, for the two presented sets of acoustic data. In addition, the period of oscillation can be calculated as the difference between these high-to-low or low-to-high transition events, and the averaged period value within each 1.28-s acquisition time is converted to a

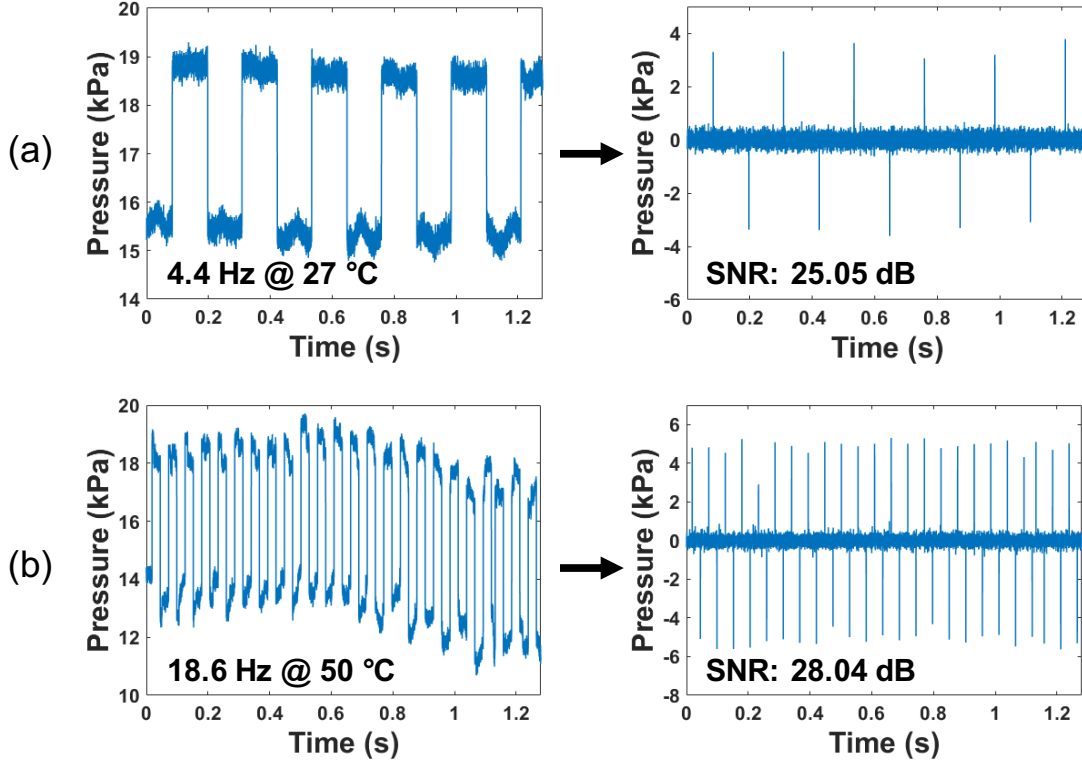


Figure 5.10: (a) Backscattering data acquired at 27 °C with an SNR of 25.05 dB; (b) backscattering data acquired at 50 °C with an SNR of 28.04 dB.

temperature value with the fitting model presented in the Equation 3.15 in Chapter 3. The process repeats in real time to obtain continuous temperature measurements.

#### 5.1.4 Graphical user interface (GUI)

The control of the ultrasound interface and the acquisition and processing of the backscattering data were performed through custom programs embedded in a graphical user interface (GUI) in MATLAB, as shown in Figure 5.11. The GUI consists of three panels. Panel 1 in the lower right corner is the interface to set certain parameters for the ultrasound used to power up and communicate with the motes, such as the excitation voltage, the focal length, and the time gain compensation. Other relevant parameters, including the operating frequency, pulse repetition period, and the number of cycles in each pulse, can be specified in the programs prior to initializing this GUI. This panel also allows freezing the programs to stop ultrasound

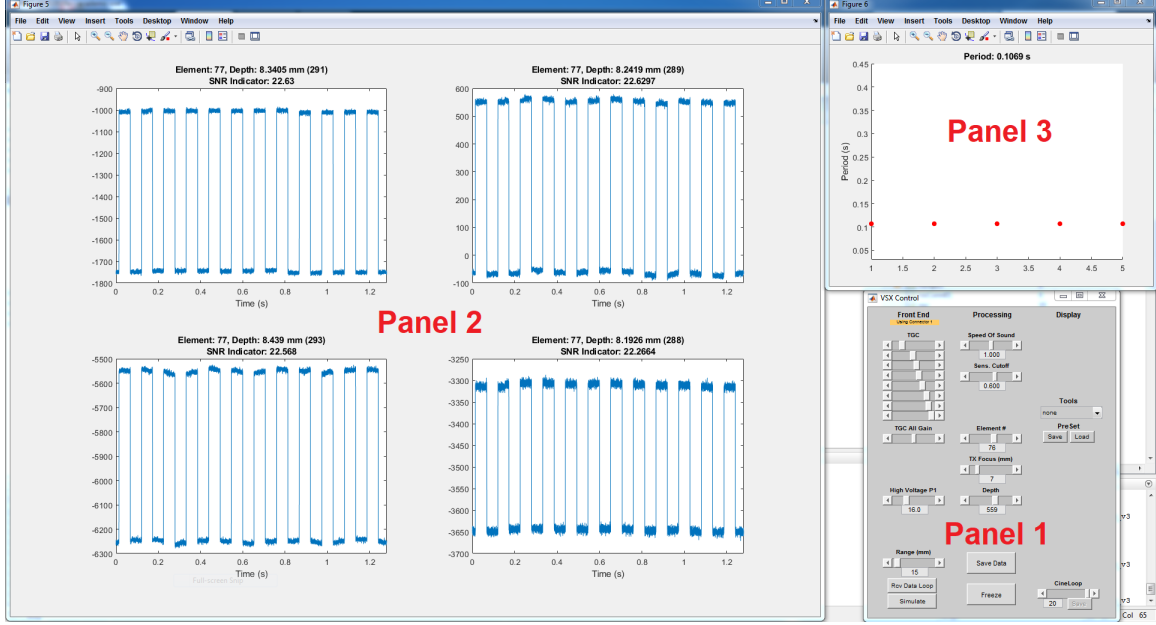


Figure 5.11: The GUI for controlling the ultrasound interface and acquiring and analyzing the backscattering data.

delivery and saving the acquired data when needed. Panel 2 in the left shows four sets of real-time backscattering data with the top-four SNRs among all the acquired data sets corresponding to each element at each depth. Panel 3 in the upper right corner displays the period values, which translate to temperature, extracted from the backscattering data in real time. Such a GUI enables convenient tuning of the ultrasound parameters and also allows the continuous data acquisition and analysis.

### 5.1.5 Temperature sensing performance

The temperature curves of the three wire-bonded motes from 25 °C to 50 °C, the biologically relevant temperature range, were acquired acoustically where the frequency varies with temperature from 3.67 Hz to 16.06 Hz in average (Figure 5.12a). With a two-point calibration at 30 °C and 44 °C, a fitting curve can be obtained for each mote. The fit provides an average temperature error of +0.18/-0.29 °C with the error across temperature for each mote shown in Figure 5.12b. This performance is comparable to other wireless temperature sensors with much larger form factors

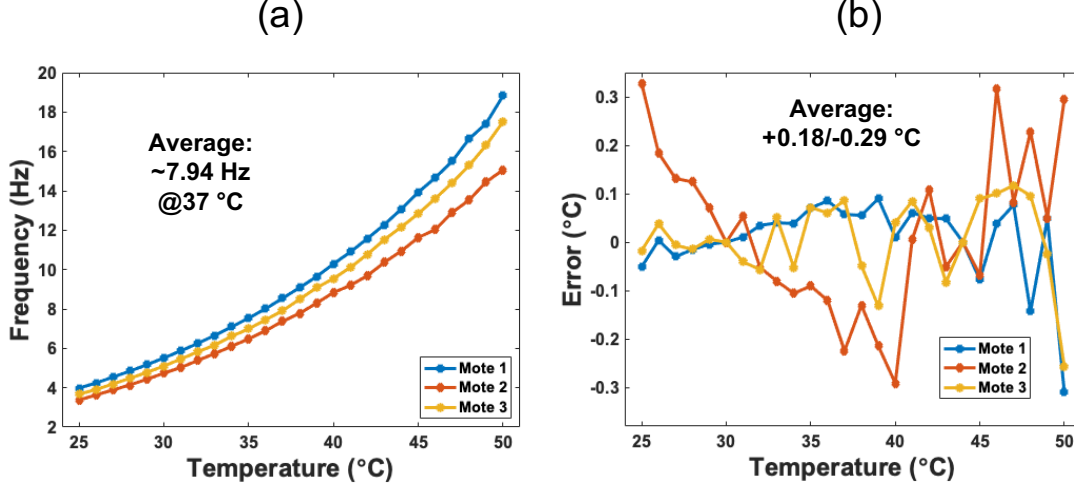


Figure 5.12: (a) The temperature curves of three wire-bonded motes; (b) the temperature error for the motes with an average of  $+0.18/-0.29$  °C.

[45, 73].

From measurements of these three motes, we find the average oscillator period jitter to be 447.66 ppm ( $154.8 \mu\text{s}$ ) ( $\sigma / \mu = 0.076$ ) by taking 100 consecutive period measurements at 22 °C, which is very close to the jitter performance quantified in the electrical testing. This shows that wireless powering with ultrasound introduces a less-than-50-ppm increase in the period jitter of the oscillator. Dividing the jitter by the measured temperature sensitivity at 22 °C ( $0.0198 \text{ s}/^\circ\text{C}$ ), the temperature resolution ( $1\sigma$ ) is found to be  $0.0078$  °C rms on average (Figure 5.13), sufficient for physiological temperature monitoring [56].

Also we can convert the line sensitivity of  $0.61 \text{ \%}/\text{V}$  to  $0.088$  °C/V with the temperature sensitivity expressed as a percentage ( $6.9 \text{ \%}/^\circ\text{C}$ ), which is low enough for the proper temperature sensing functionality. Specifically, the required  $I_{SPTA}$  of the input ultrasound power to generate a rectifier output from 0.8 V to 1.8 V was measured to be from  $0.07 \text{ mW}/\text{mm}^2$  to  $0.25 \text{ mW}/\text{mm}^2$ , a wide input range within which the temperature error due to supply variation is only 0.088 °C.

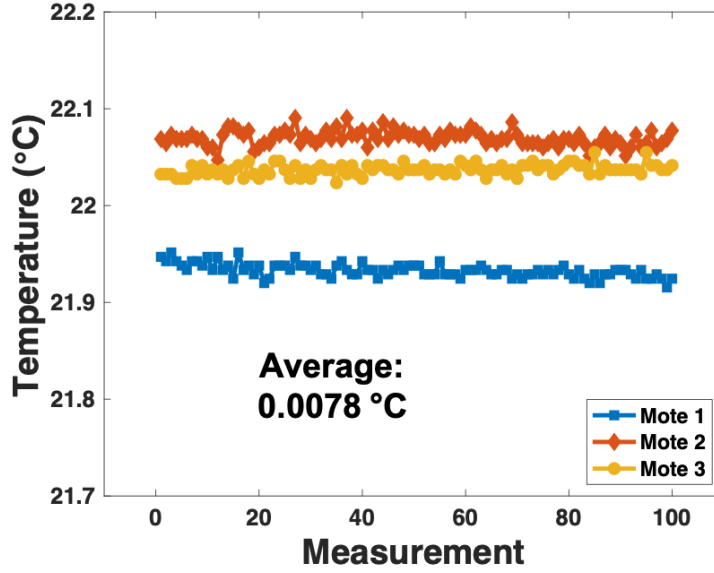


Figure 5.13: The temperature resolution of the three wire-bonded motes.

### 5.1.6 Ultrasound beam profile

The measurements of these wire-bonded motes assumed good alignments between the motes and the ultrasound source with a  $0^\circ$  incident angle, which can be impaired when the motes are implanted. The effects of misalignment were investigated by acquiring the beam profile of the ultrasound applied to a  $250\text{ }\mu\text{m} \times 250\text{ }\mu\text{m}$  PZT transducer, that is, one having the same size and fabricated in the same way as the on-chip transducers. As illustrated at the top of Figure 5.14, the L12-3v probe was swept in 3D using the translation stage while the output voltage across the receiving PZT transducer was measured at each swept location for the ultrasound source and converted to the received pressure amplitude. The acquired pressure map in a  $2\text{ mm} \times 2\text{ mm}$  XY-plane parallel to the receiving transducer at a 22-mm distance is shown at the bottom left of Figure 5.14. Additionally, the ultrasound beam pattern in a  $2\text{ mm} \times 2\text{ mm}$  XZ-plane at 21-mm-to-23-mm distances perpendicular to the PZT is shown at the bottom right of Figure 5.14.

Both plots illustrate a maximum received pressure when the PZT transducer is well-aligned with the ultrasound source with a  $0^\circ$  incident angle. Any misalignment

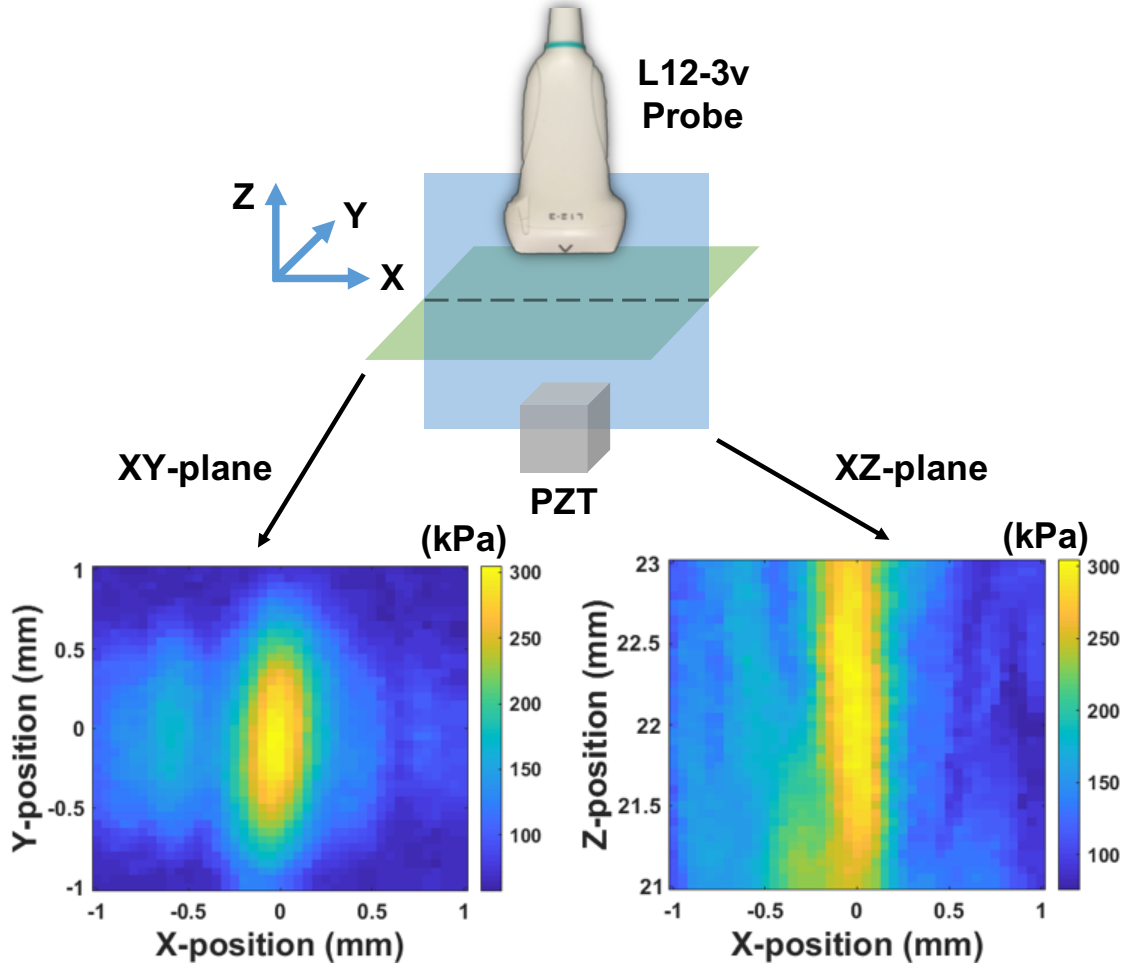


Figure 5.14: Top: an illustration of measuring the ultrasound beam profile using a fabricated  $250\ \mu\text{m} \times 250\ \mu\text{m}$  PZT transducer; bottom left: the pressure map in the XY-plane at a 22-mm distance in a  $2\ \text{mm} \times 2\ \text{mm}$  region; bottom right: the beam pattern in the XZ-plane in a  $2\ \text{mm} \times 2\ \text{mm}$  region.

with a non-zero incident angle requires an increased ultrasound power to compensate for the loss of the received pressure, as shown in 5.15a, where the peak pressure amplitude received by the PZT transducer with respect to the incident angle from  $-20^\circ$  to  $20^\circ$  was measured. It is found that the pressure level at  $+20^\circ$  or  $-20^\circ$  is approximately a third of that at  $0^\circ$ . Correspondingly, the required ultrasound intensities to activate the mote and reliably receive the backscattering data at these incident angles were also quantified, where the intensity at  $+20^\circ$  or  $-20^\circ$  is around nine times that at  $0^\circ$  (Figure 5.15b). These measurements suggest a preferable orientation with no angular mismatch between the motes and the ultrasound source and confirm an inevitable



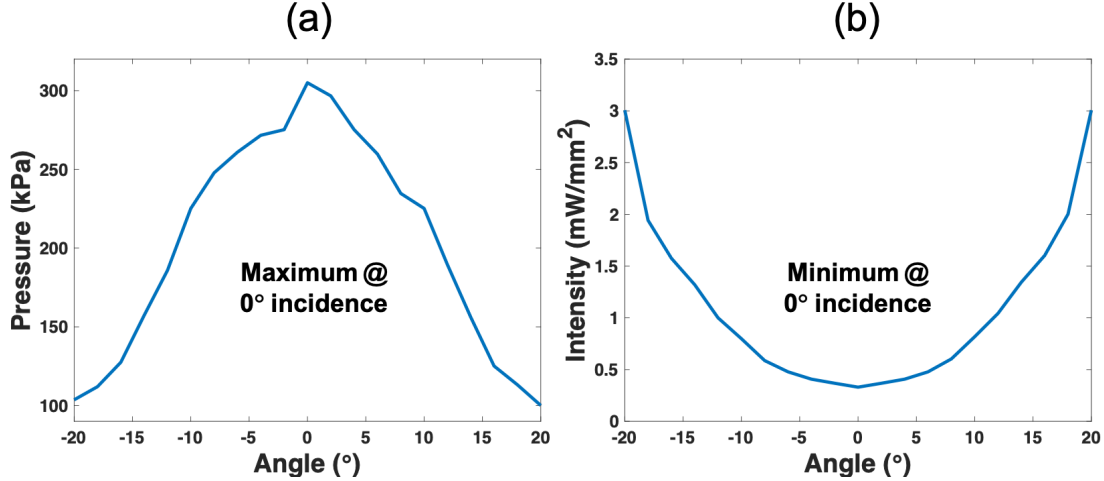


Figure 5.15: (a) The peak pressure amplitude received by the PZT transducer with respect to the incident angle from  $-20^\circ$  to  $20^\circ$ ; (b) the required ultrasound intensity to activate the mote with respect to the incident angle.

increase in the required ultrasound energy when the motes are not well-aligned with the source. Therefore, the motes should be oriented towards and aligned with the external ultrasound source as much as possible when implanted.

## 5.2 *In-vitro* experimentation with the standalone motes

### 5.2.1 Testing with chicken tissues

Knowing the beam profile of the ultrasound received by the PZT transducer, we further tested three integrated and standalone motes released from the dies fully-wirelessly with only an ultrasound energy source. In this way, no electrical outputs can be acquired and the only way to determine circuit operation is through the acquired acoustic backscattering data.

The experimental setup is shown in Figure 5.16. Each mote was separately mounted to the center of a 3D-printed case, similar to the setup for testing the wire-bonded motes. A piece of  $\sim 3$ -mm-thick chicken thigh was placed on top of the

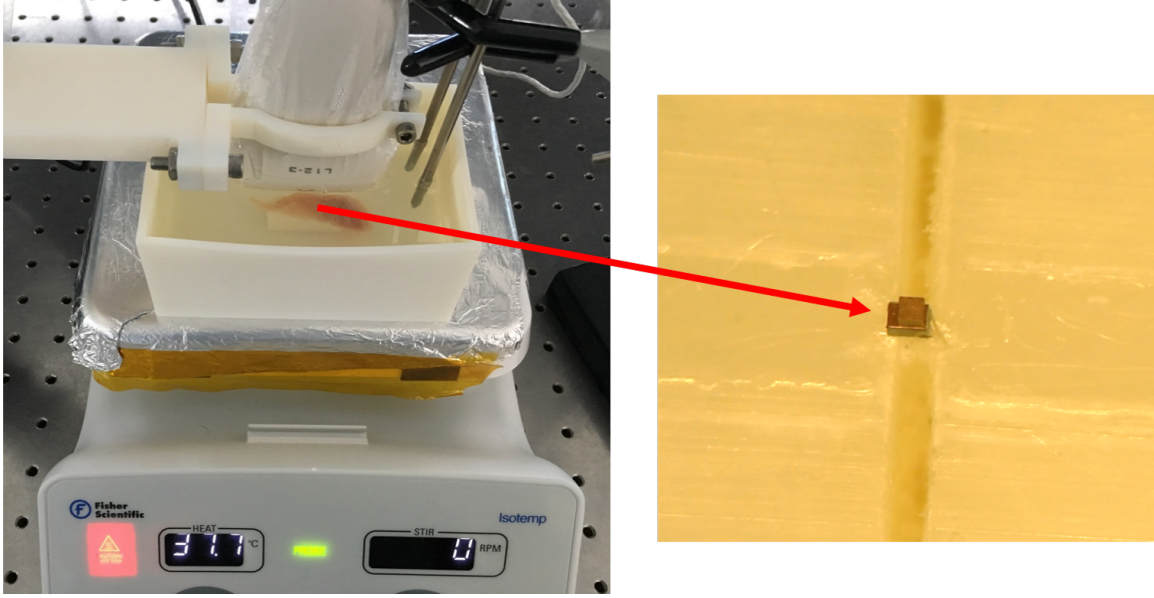


Figure 5.16: The experimental setup for fully-wireless ultrasound testing with a mote released from the die. Similar to the testing setup for the wire-bonded motes, the standalone mote was mounted on a case and covered with a piece of 3-mm-thick chicken thigh as a biological tissue medium.

mote to mimic biological tissues. In addition, the mote was tested without blocking the light as it was found that the deposited copper metal on the mote effectively shielded the light and made the mote immune to optical effects.

The imaging script was first used to locate the mote-under-test in an ultrasound image (Figure 5.17). The data collection script was then used to send focused ultrasound to power up the mote. To overcome the attenuation due to the chicken thigh, ultrasound was transmitted with a peak pressure amplitude of  $\sim 451.1$  kPa and an  $I_{SPTA}$  of  $\sim 0.33$  mW/mm<sup>2</sup>, much lower than the FDA limit of 7.2 mW/mm<sup>2</sup> [55]. On the other hand, the mechanical index (MI) that characterizes the effects of the peak pressure on animal tissues [130] is calculated to be 0.11, also much lower than the limit of 1.9 [55]. In addition, the thermal index [130] is estimated to be 0.12, indicating a minimal temperature increase of  $\sim 0.12$  °C due to ultrasound under these conditions.

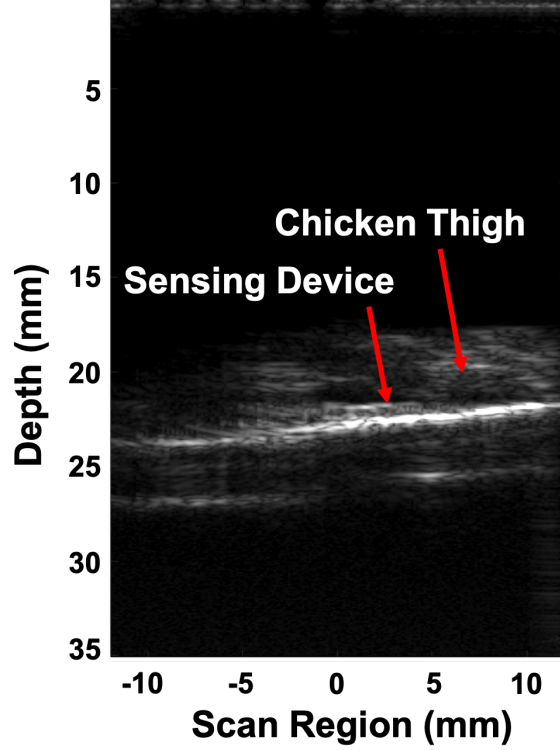


Figure 5.17: The ultrasound image showing a piece of chicken thigh placed on top of a sensing mote during a fully-wireless testing.

### 5.2.2 Temperature sensing performance

Acoustic backscattering data was acquired again from 25 °C to 50 °C for wireless operation of the three standalone motes (Figure 5.18a). After a two-point calibration at 30 °C and 46 °C, the average temperature error is found to be  $+0.26/-0.26$  °C, as shown in Figure 5.18b, similar to the wire-bonded motes. The average temperature error for the three wire-bonded motes and the three standalone motes combined is found to be  $+0.22/-0.28$  °C. Due to device-to-device variation, the six tested motes show moderately different frequency readouts at the same temperature (Figure 5.12a and Figure 5.18a). However, after two-point calibration, the six motes produce accurate and similar temperature outputs when compared with the reference temperature, as shown in Figure 5.19, with an average  $\sigma / \mu$  of 0.0035 across the temperature range.

A long-term continuous measurement for one of the motes was performed at  $\sim 45$  °C for over four hours. The acquired temperature data that tracked the temperature

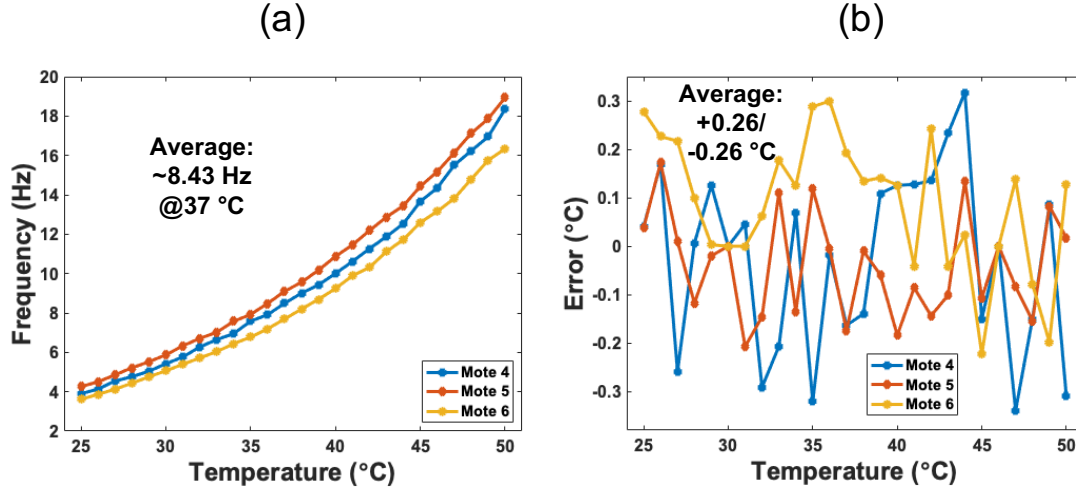


Figure 5.18: (a) The temperature curves of three standalone motes; (b) the temperature error for the motes with an average of  $+0.26/-0.26^{\circ}\text{C}$ .

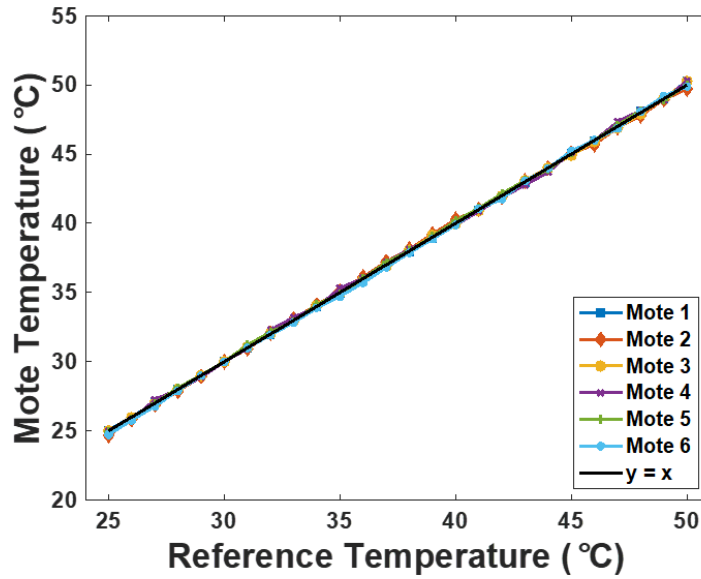


Figure 5.19: The calibrated temperature outputs from the six tested motes compared with the reference temperature.

fluctuations due to the environment is shown in Figure 5.20a, along with the logged reference temperature simultaneously measured with the thermometer. The Allan deviation of the long-term measurement from the mote is shown in Figure 5.20b, showing a floor of  $<138.6 \text{ ppm}$ , limited only by the measurement time. This demonstrates the minimal self-heating effects from ultrasound on the circuit operation and the feasibility of using the proposed mote for long-term physiological temperature

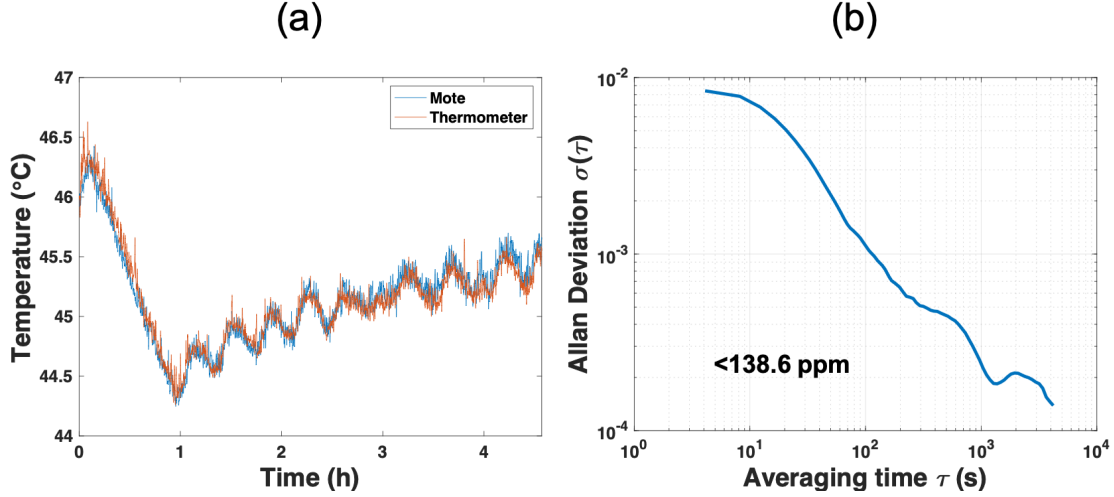


Figure 5.20: (a) A long-term measurement of over four hours of one wireless mote at  $\sim 45^\circ\text{C}$  compared with the reference thermometer; (b) the Allan deviation of the long-term temperature measurement in (a) showing a floor of  $<138.6$  ppm (limited by the measurement time).

monitoring. Moreover, continuous immersion of a standalone mote in water for  $>7$  days revealed no damage to the film and negligible effects on the circuit functionality, demonstrating the effective encapsulation with parylene.

### 5.2.3 Comparison with the state-of-the-art

Comparison to the state-of-the-art Table 5.1 compares the proposed temperature sensing mote with other similar wireless sensing systems, showing a better or similar sensing performance including temperature resolution and error, but with a more compact form factor with the CMOS-PZT integration efforts pursued in this work.

## 5.3 *In-vivo* evaluation in mice with the standalone motes

Following the comprehensive *in vitro* characterization, these standalone motes were deployed in laboratory mice to verify their proper operation and evaluate their sens-

Table 5.1: Comparison with the state-of-the-art.

	<b>This work</b>	<b>[45]</b>	<b>[48]</b>	<b>[73]</b>
<b>Technology</b>	180 nm	55 nm	130 nm	180 nm
<b>Dimension</b>	$380 \times 300 \times 570 \mu\text{m}^3$	$360 \times 400 \times 280 \mu\text{m}^3$	$480 \times 480 \mu\text{m}^2$ (chip only)	$1.1 \times 2.2 \times 0.4 \text{ mm}^3$
<b>Volume</b>	$0.065 \text{ mm}^3$	$0.04 \text{ mm}^3$	-	$0.97 \text{ mm}^3$
<b>Monolithic Integration</b>	Yes	No	No	No
<b>Calibration</b>	Two-point	Two-point	Two-point	Two-point
<b>Resolution (rms)</b>	$0.0078 \text{ }^\circ\text{C}$	$0.034 \text{ }^\circ\text{C}$	$0.046 \text{ }^\circ\text{C}$	$0.3 \text{ }^\circ\text{C}$
<b>Sensing Error</b>	$+0.22/-0.28 \text{ }^\circ\text{C}$	$+0.38/-0.33 \text{ }^\circ\text{C}$	$+1.3/-2.6 \text{ }^\circ\text{C}$	$+1.5/-1.4 \text{ }^\circ\text{C}$
<b>Power Source</b>	Ultrasound	Light	RF	Battery
<b>Power Consumption</b>	0.813 nW	16 nW	$1.05 \mu\text{W}$	71 nW

ing performance in a real biological environment. Implantation of the motes were performed by Dr. Victoria Andino Pavlovsky on mice brains as well as in mice hind limbs to examine the feasibility of using these motes as temperature sensors at different locations. The core body temperature on the brain and in the limb were separately recorded fully-wirelessly with only an ultrasound source. In addition, in collaboration with Professor Konofagou and her student, Stephen Alexander Lee, we performed neuromodulation at the sciatic nerves located inside hind limbs of mice with focused ultrasound (FUS). The temperature changes during the stimulation were simultaneously recorded with motes implanted under the nerves in an effort to investigate the thermal effects of FUS and the associated neuromodulation effects.

For all the *in vivo* experiments, ultrasound transmission gel (Aquasonic 100, Parker Laboratories Inc., Fairfield, NJ) was used as the coupling medium in place of DI water to accommodate the normal animal activities. Gel has similar acoustic properties as water and is widely used in medical ultrasound imaging. To remove

the air bubbles inside the gel, which heavily attenuate ultrasound, centrifuging was performed on the gel at 3000 rpm for 1 hour at room temperature. In addition, the degassed gel was microwaved for 8 s to warm it up to the body temperature of mice prior to the use.

The Institutional Animal Care and Use Committee (IACUC) reviews and approves protocols for Columbia University's programme for the humane care and use of animals and inspects the animal facilities and the research laboratories. Evaluation of the implanted motes was performed in compliance with IACUC regulations under the approved protocol of AC-AAAZ0451. Mice were obtained from Jackson laboratories and housed in the Institute of Comparative Medicine facility of Columbia University. Surgeries were performed in animals 3-8 weeks old.

### **5.3.1 On the brain**

A mouse was anesthetized with 1 g/kg urethane administered intraperitoneal. While head-fixed by means of a Kopf stereotaxic apparatus, fur was removed with hair-removal cream, the scalp was open and a  $1.5 \times 1.5$  mm cranial window (Figure 5.21 left) was drilled using 0.5 mm bits. A single mote was then placed on the exposed brain (Figure 5.21 middle). The edge of the substrate was fixed through its edges to the surrounding skull with biocompatible cyanoacrylate glue (Krazy Glue). The scalp was then closed, covering the implanted device (Figure 5.21 right).

Figure 5.22 shows the experimental setup for testing the implanted mote. The L12-3v probe was positioned  $\sim 5$  mm above the head of the mouse, as identified with ultrasound imaging (Figure 5.23). Ultrasound energy with an intensity of  $0.24 \text{ mW/mm}^2$  was transmitted to the mote through ultrasound gel, which successfully powered up the mote. Backscattering data was obtained in this configuration, as shown in Figure 5.24. An external temperature probe was placed subdermally in the neck area in order to log temperature recordings for reference. The acoustically-

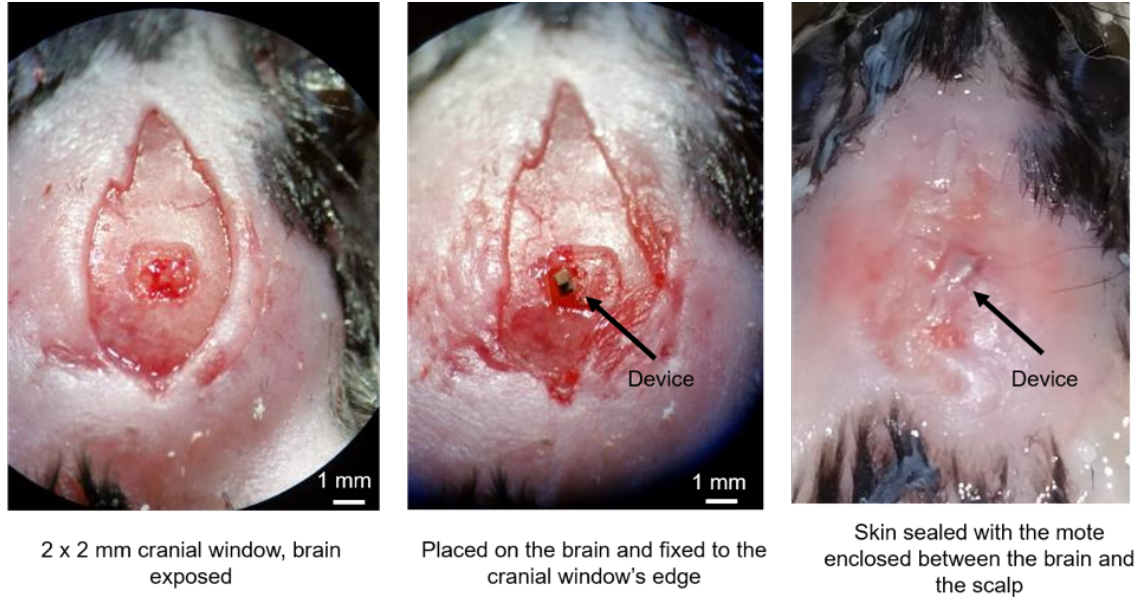


Figure 5.21: The surgical procedures for subdermal implantation on the brain.

obtained backscattering data was converted to temperature, as shown in Figure 5.25 for a continuous recording of 10 minutes, which complied well with the reference temperature. The recorded temperature values were lower than the normal core temperature because the mouse had been experiencing long anesthesia when we took the measurements.

### 5.3.2 In the hind limb

Thereafter, we performed subdermal implantation of a different mote in the hind limb of a mouse in a similar way as the implantation procedures performed on the brain. The mouse was anesthetized with 1 g/kg urethane administered intraperitoneal. The hind limb was fixed to an acrylic base with Krazy glue to minimize movement caused by breathing. The skin and underlying tissue were cut open with fine scissors, and the mote fixed on a polyimide (PI) substrate for handling (Figure 5.26a) was placed between the skin and the muscle, without further fixation. The skin was closed, covering the device, as shown in Figure 5.26b.

Ultrasound energy with an intensity of  $0.38 \text{ mW/mm}^2$  was coupled to the im-



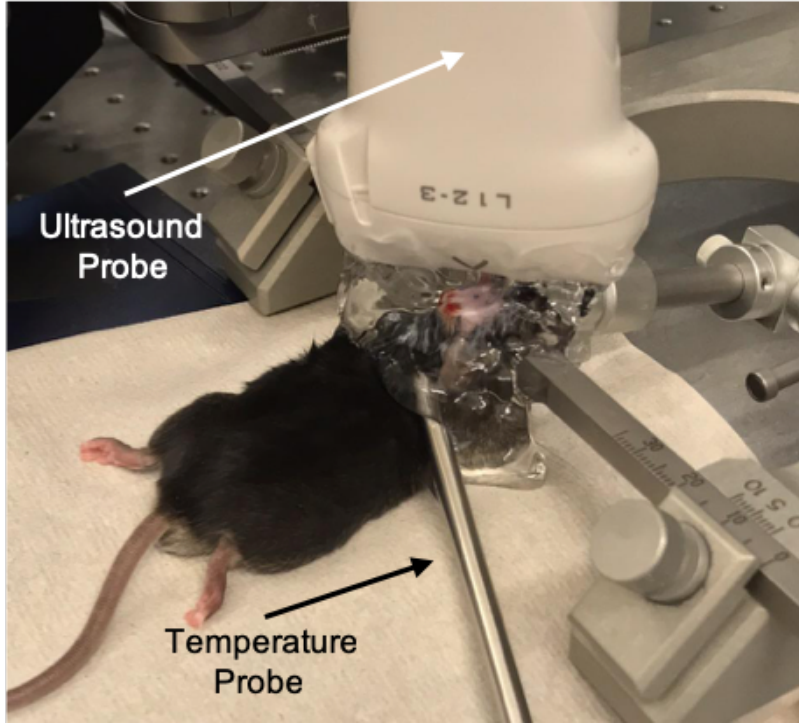


Figure 5.22: The experimental setup with the mote implanted on the brain.

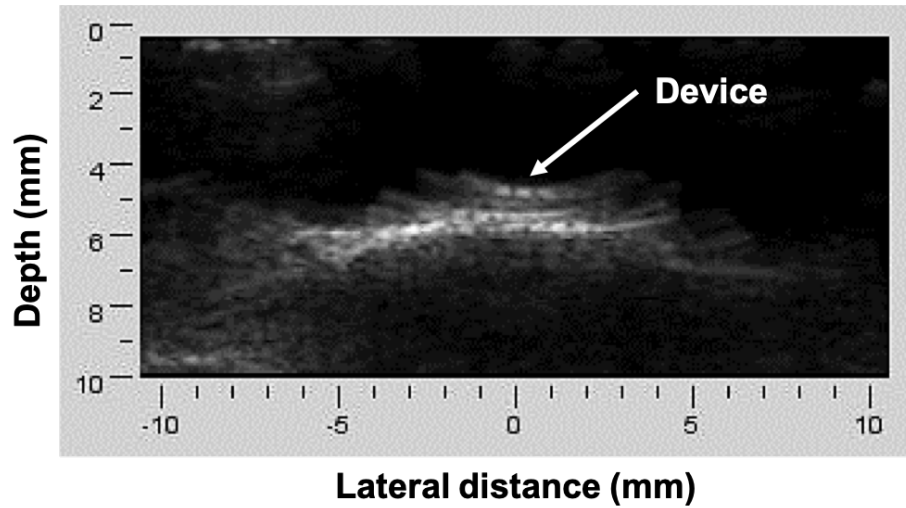


Figure 5.23: The ultrasound image showing the mote located above the skull.

planted mote through gel, as shown in Figure 5.27, and backscattering data was acquired fully-wirelessly (Figure 5.28). A long-term measurement of the body temperature in this configuration for  $\sim 6$  minutes is shown in Figure 5.29. For this experiment, the heating pad was removed for a short period, resulting in a decrease in the body temperature. This shows an accurate tracking of temperature with our

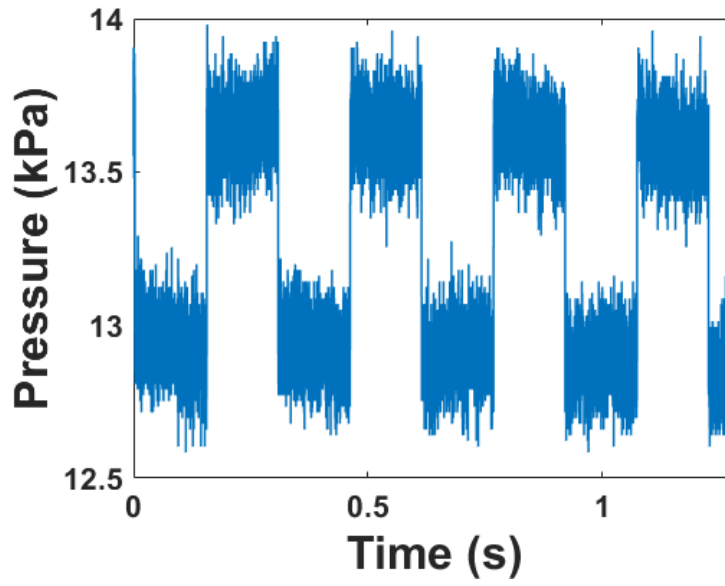


Figure 5.24: The acoustic data obtained with the mote implanted on the brain.

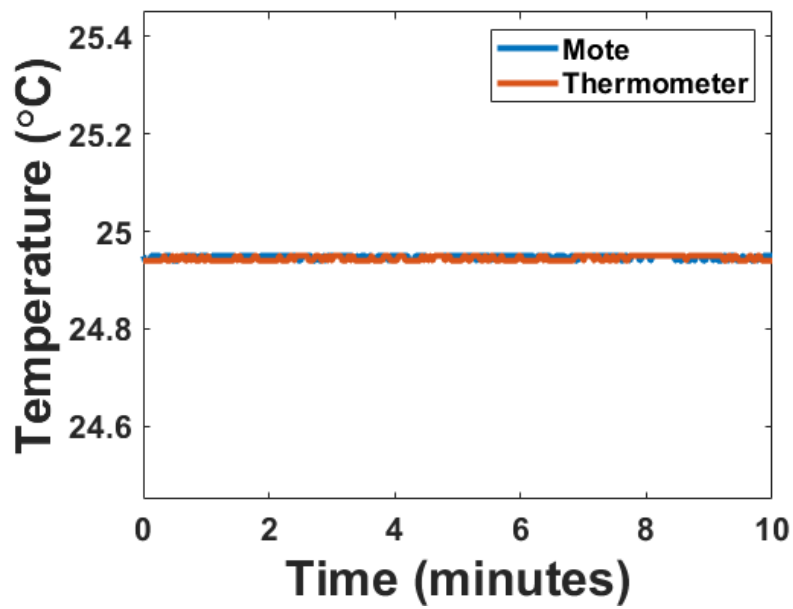


Figure 5.25: A continuous temperature recording for 10 minutes with the mote implanted on the brain.

mote.

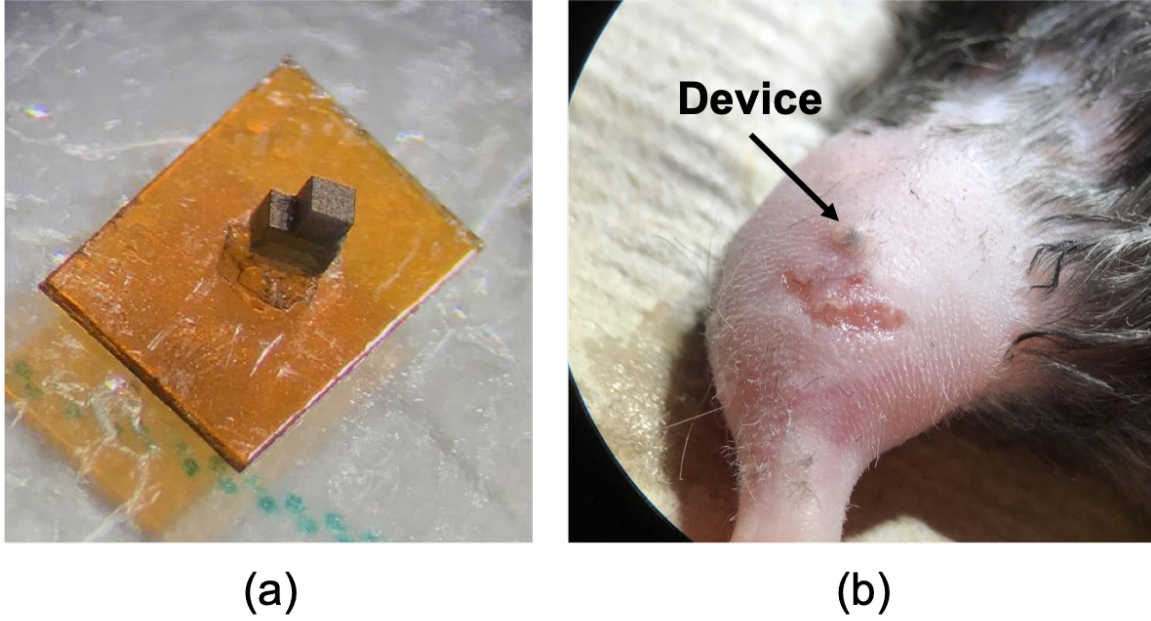


Figure 5.26: (a) A mote fixed on a PI substrate for implantation; (b) subdermal implantation of the mote in the hind limb.

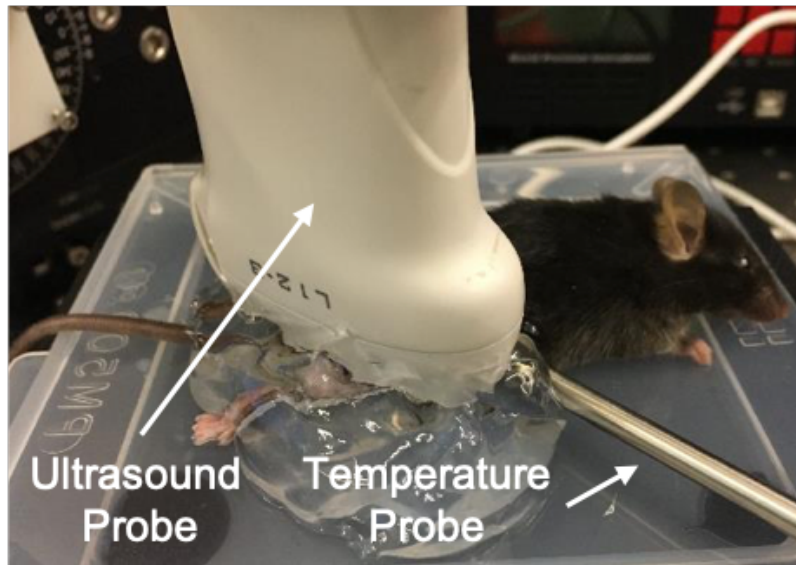


Figure 5.27: The experimental setup with the mote implanted in the hind limb.

### 5.3.3 Under the sciatic nerve

Further utility of the mote was investigated in regards to FUS neuromodulation of the peripheral nervous system. We studied sciatic nerve temperature in response to FUS. A mouse was anesthetized with isoflurane (1-5% v/v). The mouse's hind

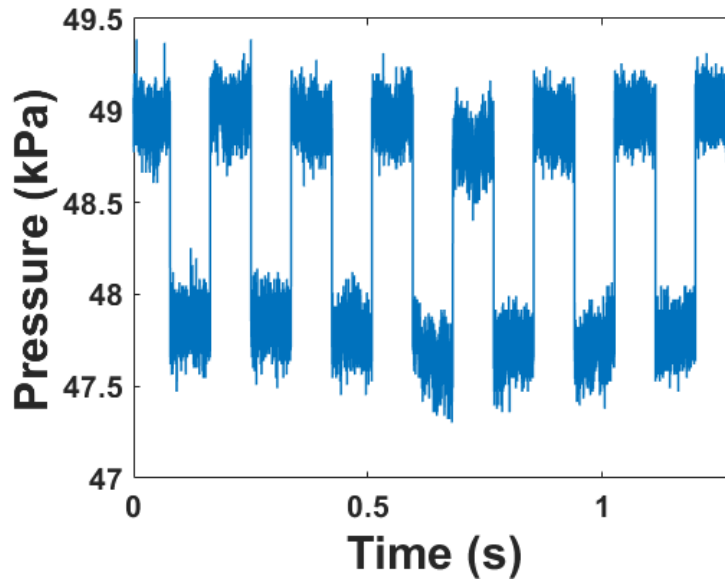


Figure 5.28: The acoustic data obtained with the mote implanted in the hind limb.

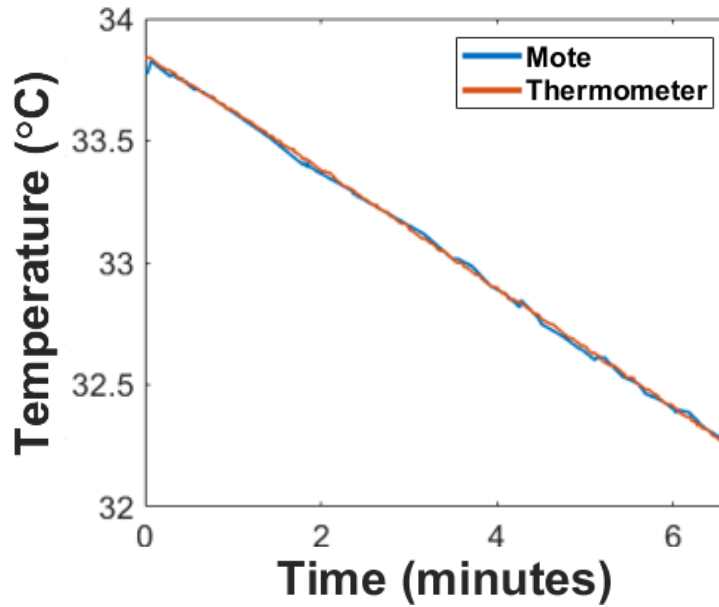


Figure 5.29: A continuous temperature recording for  $\sim 6$  minutes with the mote implanted in the hind limb.

limb was fixed with glue to a plastic base. An incision was made right under the femur bone and the muscle was cut open in order to expose the sciatic nerve. Once the sciatic nerve was exposed, it was gently lifted using curved tweezers and a PI substrate ( $\sim 1 \text{ mm} \times 3 \text{ mm}$ ) with two motes attached was carefully placed under the

nerve. A cartoon illustration of the strategy for such implantation is shown in Figure 5.30a. The motes were fixed with glue to the two edges of the substrate ( $\sim 1 \text{ mm} \times 3 \text{ mm}$ ), leaving a space in the middle to accommodate for the sciatic nerve. In such a way, each mote was conveniently located at each side of the nerve (Figure 5.30b) to record temperature changes right at the nerve during FUS stimulation. Additionally, a saline solution was applied to the incision to prevent the nerve from drying out during the experiment.

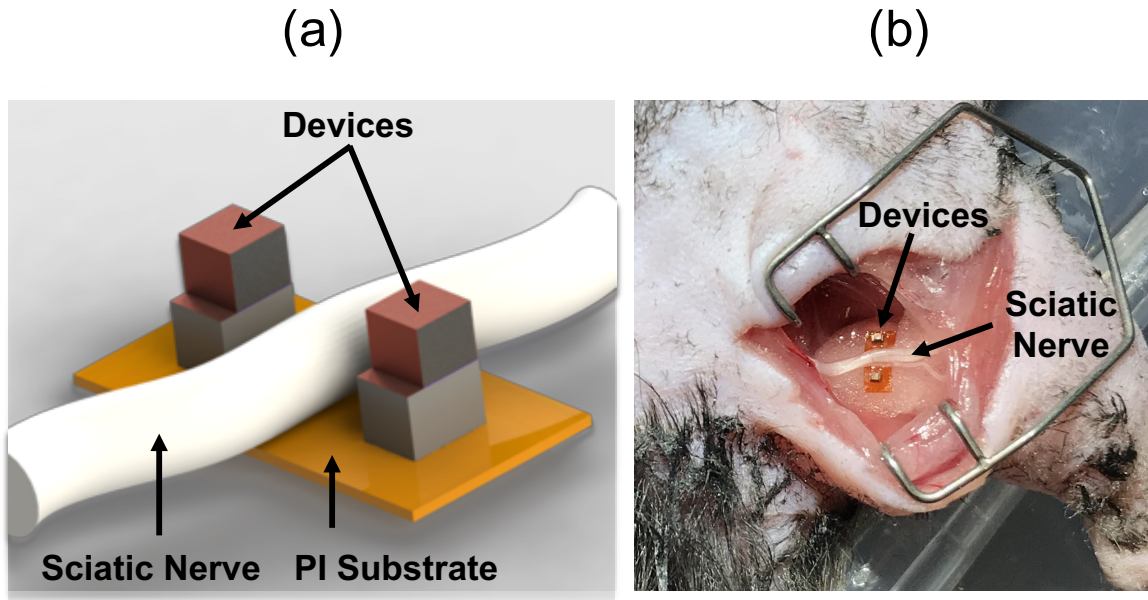


Figure 5.30: (a) A cartoon illustration of the strategy for implantation at the sciatic nerve; (b) implantation of two motes at the sciatic nerve.

Following the implantation, a hind limb of the mouse was placed on top of a custom 3D-printed FUS coupling cone filled with degassed water (Figure 5.31). The cone was designed for a 3.57-MHz therapeutic ultrasound transducer (SU-107, SonicConcepts, Bothell, WA) where the focus was indicated by cross-hairs on the cone itself. The transducer was connected to a function generator (33120A, Agilent, Santa Clara, CA) and RF amplifier (A150, E&I, Rochester, NY) for generating ultrasound pulses with a 3.57-MHz operating frequency and a 1-ms pulse duration. Four stimulation intensities were used in accordance with parameters found successful in a previous



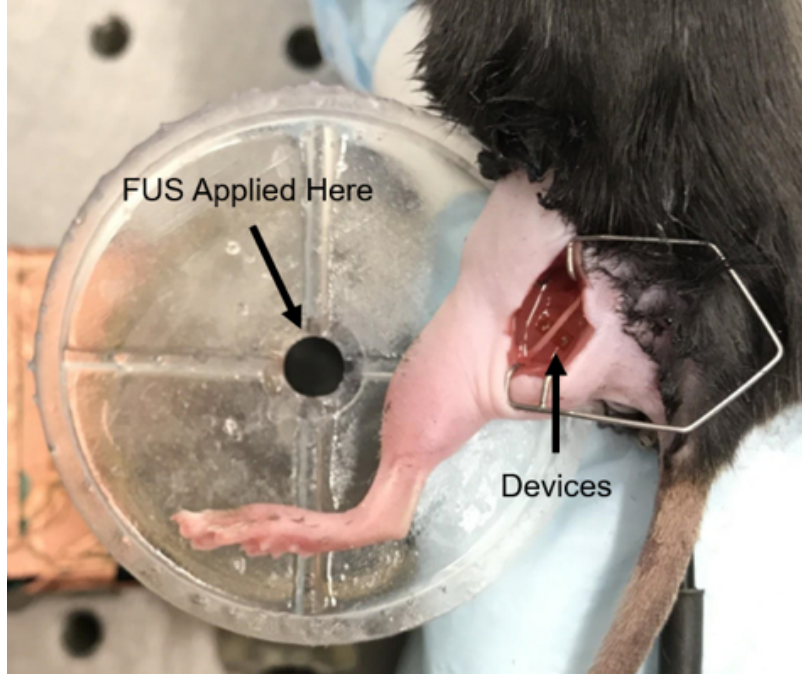


Figure 5.31: Illustration of applying FUS from beneath the sciatic nerve.

neuromodulation study [36] to stimulate the sciatic nerves inside the lower hind limb. Ultrasonic pulse trains of 1-ms pulse duration, 10-Hz pulse repetition frequency, and peak-to-peak pulse amplitudes of 400 mV, 500 mV, 600 mV, and 700 mV, respectively, were used to induce muscle contractions in the gastrocnemius muscle of the lower hind limb (Figure 5.32), confirmed with electromyography (EMG) recordings with a needle electrode (Biopac, CA), as shown in Figure 5.33. Our results indicate that higher ultrasound intensities lead to larger areas under the curve and higher peak amplitudes in the EMG recordings (Figure 5.34).

At the same time, the L12-3v probe measured the resulting temperature rise at the motes (Figure 5.35). Acoustic backscattering data was reliably obtained with an ultrasound intensity of  $0.2 \text{ mW/mm}^2$ , as shown in Figure 5.36. Temperature increases at the sciatic nerve were calculated by subtracting the temperature measured immediately before FUS exposure from the value measured immediately after FUS exposure. As shown in Figure 5.37a, both motes recorded similar temperature increases, ranging from  $0.24^\circ\text{C}$  to  $0.77^\circ\text{C}$ , for the four different stimulation intensities. A higher

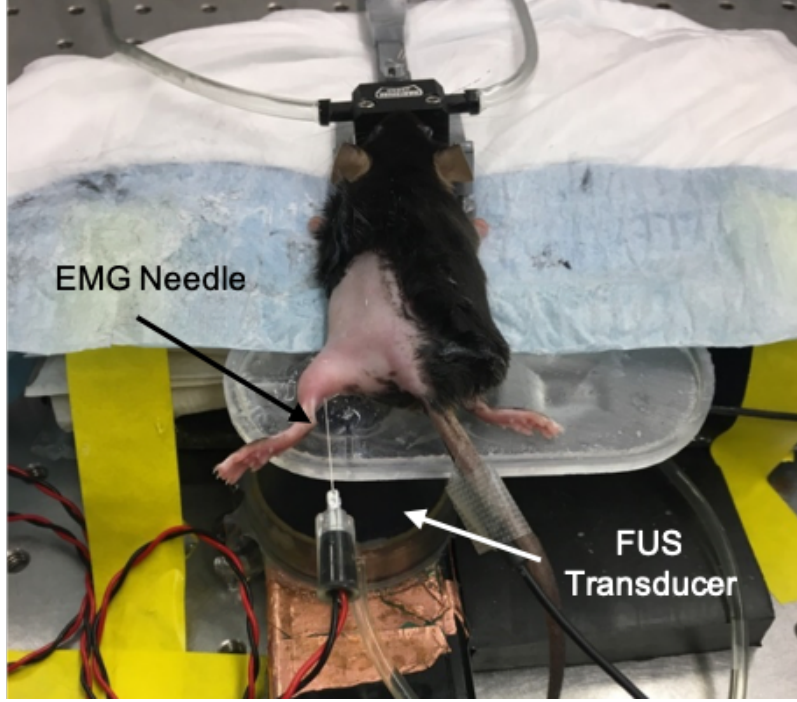


Figure 5.32: The experimental setup for measuring the EMG responses in the leg of a mouse with FUS stimulation at the sciatic nerve.

intensity results in a larger temperature increases as expected, which shows the same trend as the EMG results. In comparison, temperature increases were not seen for single FUS pulses (Figure 5.37b), showing minimal effects of FUS on the temperature sensing performance of the motes.

Since previous studies have shown electrical changes in membrane capacitance due to infrared-induced local heating [131], FUS neuromodulation may also use these same mechanisms. With the therapeutic parameters, it is hard to discount the contribution of cavitation on the mechanisms. However, taken together, these results show that, using our device, temperature at the nerve during FUS may change but may not be the main driving force behind sciatic nerve neuromodulation.

Therefore, the proposed motes can be used towards different kinds of *in vivo* temperature sensing applications from routine measurements of core body temperature to temperature monitoring during thermal-related procedures. They can replace the conventional temperature probes or MRI machines, which are either inconvenient or

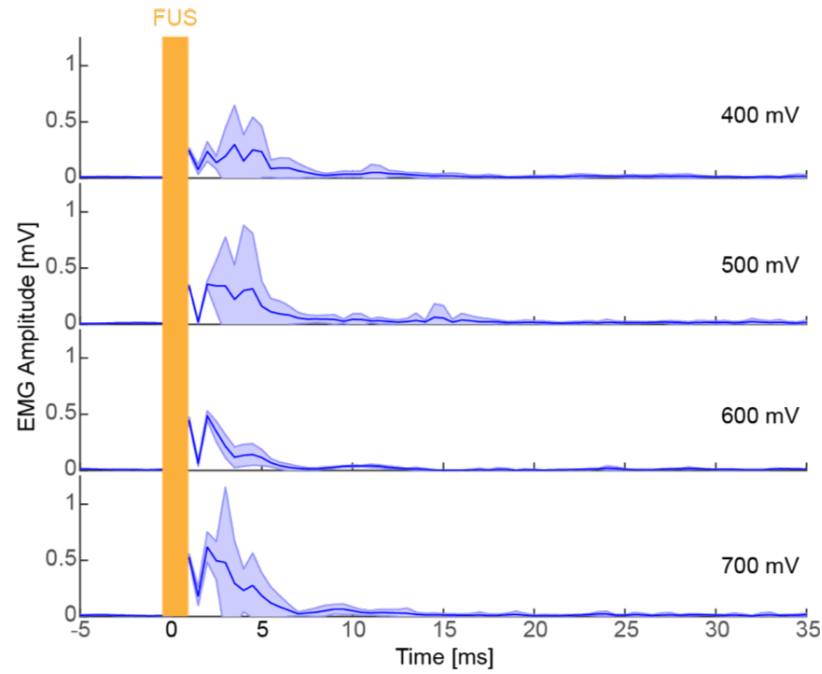


Figure 5.33: EMG signals recorded with FUS stimulation at the sciatic nerve.

expensive, for more localized and distributed sensing of physiological temperature in a fully-wireless approach.



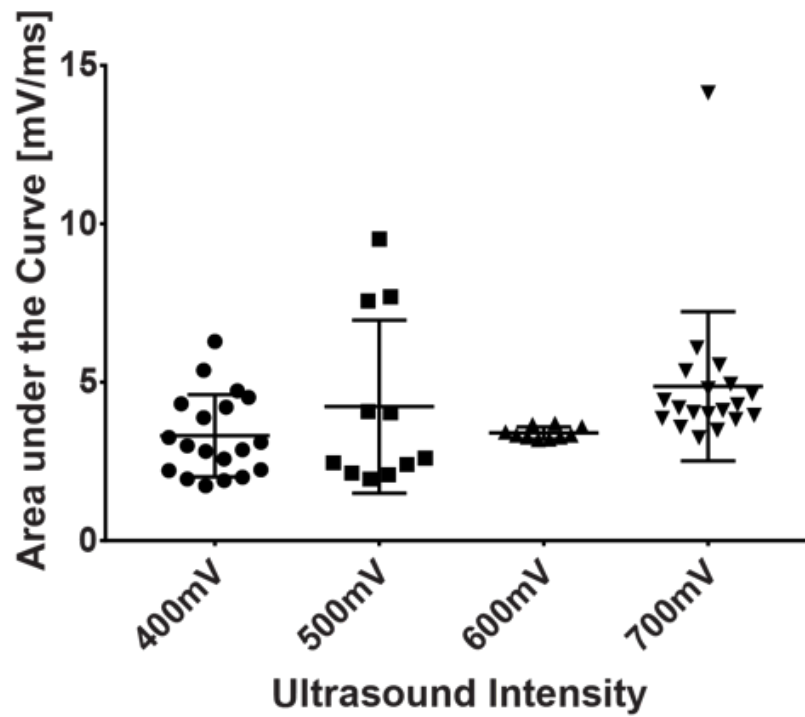


Figure 5.34: Area-under-the-curve analysis of EMGs acquired from FUS stimulation.

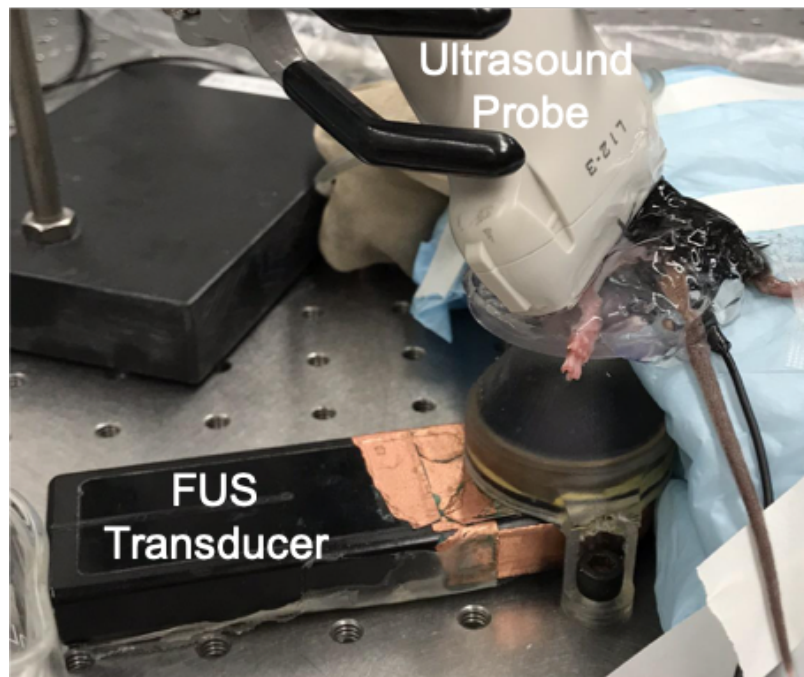


Figure 5.35: The experimental setup to measure temperature increases with FUS stimulation.

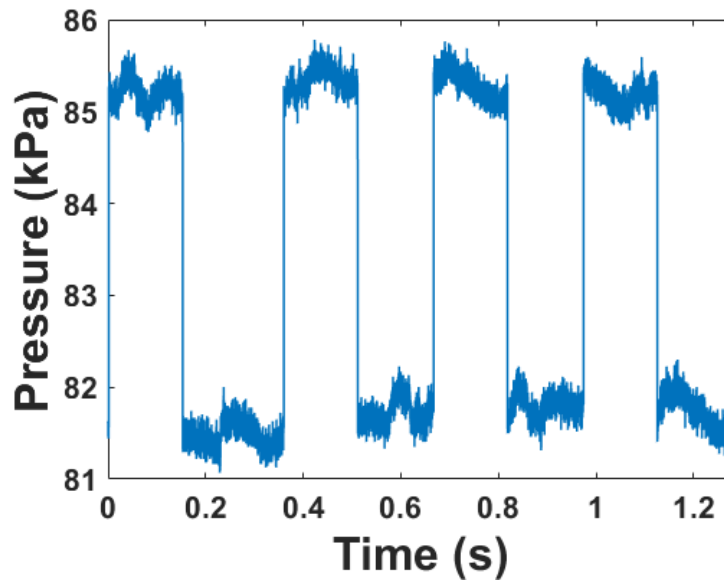


Figure 5.36: The acoustic data obtained with the motes implanted under the sciatic nerve.

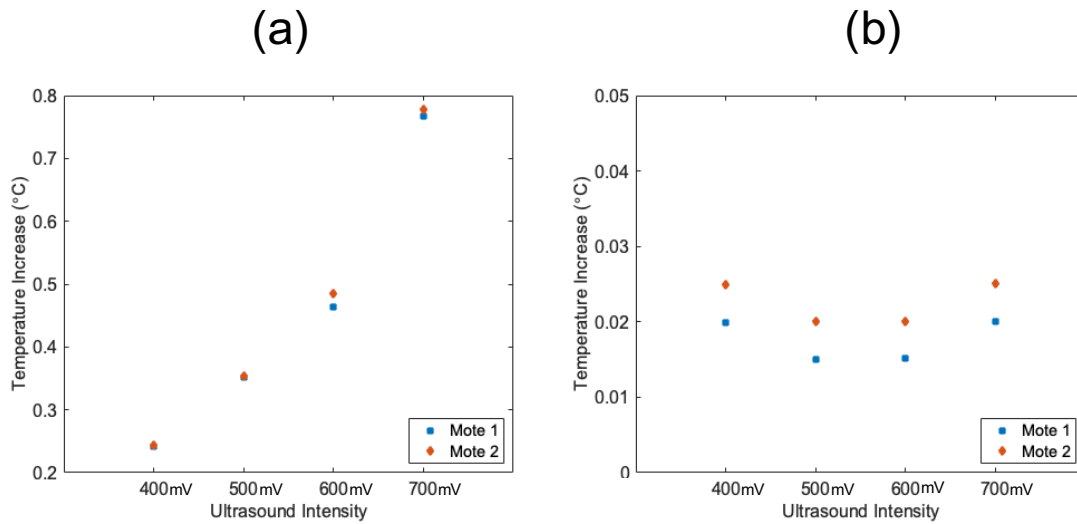


Figure 5.37: (a) The temperature increases with four different stimulation intensities; (b) negligible temperature increases with single FUS pulses.

---

## Chapter 6

# Conclusions and Future Work

---

### 6.1 Summary

In summary, this thesis presents a miniaturized, low-power, fully-wireless sensing mote with a monolithically-integrated ultrasound transducer for accurate and safe physiological temperature monitoring. The mote achieves aggressive miniaturization ( $380\text{ }\mu\text{m} \times 300\text{ }\mu\text{m} \times 570\text{ }\mu\text{m}$ ,  $0.065\text{-mm}^3$ ) by integrating a CMOS temperature sensor chip with a micron-scale PZT transducer. This on-chip transducer harvests ultrasound for wireless power and transmits temperature data through acoustic backscattering fully-wirelessly.

*In vitro* measurements of these fully-integrated motes show a temperature reso-

lution of 0.0078 °C rms, temperature error of +0.22/-0.28 °C from 25 °C to 50 °C with a  $\sim 0.813$ -nW power consumption at 37 °C. Long-term measurements show a negligible effect from ultrasound on the proper operation of the proposed mote. In addition, successful *in vivo* evaluation with these motes implanted at different locations of mice, including the brain, the hind limb, and the sciatic nerve, shows the feasibility of applying them to both the clinical and basic scientific research scenarios for continuous physiological temperature monitoring.

The extremely-miniaturized form factor and completely-wireless operation enable a number of these sensing motes to be implanted or injected using minimally invasive procedures into the targeted sites of interest. They can be deployed to perform real-time, distributed and localized *in vivo* temperature monitoring and mapping.

## 6.2 Future work

To continue the endeavor of this work, the limit on the size scaling for these motes can be investigated. Further scaling down these motes to the 100- $\mu$ m size-scale or even the 10- $\mu$ m size-scale is an interesting yet challenging topic.

Additionally, impedance matching layers can be fabricated on the integrated PZT transducers to improve acoustic performance, facilitate the ultrasonic transmission, and allow for more coupled power.

Furthermore, different kinds of piezoelectric materials can be considered, such as the PMN-PT single crystal, which has even more superior piezoelectric properties than PZT.

## 6.3 Final thoughts

The proposed sensing mote provides a complete platform for developing wireless, miniaturized implantable devices for physiological temperature monitoring. It can be

extended to the *in vivo*, wireless measurements of other types of biological parameters, such as pH, pressure, and glucose concentration. Similar techniques can be applied to integrate custom sensing electronics with piezoelectric transducers through similar microfabrication to create miniaturized, monolithic ultrasonic wireless systems and devices for biomedical sensing and monitoring applications.

---

# Bibliography

---

- [1] N. H. E. Weste and D. Harris, *CMOS VLSI Design: A Circuits and Systems Perspective*. Reading, MA: Addison Wesley, 4th ed., 2010.
- [2] G. E. Moore, “Progress in digital integrated electronics,” in *IEDM Tech. Digest*, 1975.
- [3] V. K. Khanna, *Implantable Medical Electronics: Prosthetics, Drug Delivery, and Health Monitoring*. Cham: Springer, 2016.
- [4] G.-Z. Yang, *Implantable Sensors and Systems: From Theory to Practice*. Springer, 2018.
- [5] H.-J. Yoo and C. van Hoof, *Bio-Medical CMOS ICs*. New York: Springer, 2011.
- [6] “Invasive Devices - Sepsis Alliance.” <https://www.sepsis.org/sepsisand/invasive-devices/>, 2017.
- [7] S. Bhunia, S. J. Majerus, and M. Sawan, *Implantable Biomedical Microsystems: Design Principles and Applications*. Amsterdam; Boston: Elsevier/William Andrew, 2015.
- [8] M. A. Wood and K. A. Ellenbogen, “Cardiac pacemakers from the patient’s perspective,” *Circulation*, vol. 105, no. 18, pp. 2136–2138, 2002.
- [9] F. G. Zeng, S. Rebscher, W. Harrison, X. Sun, and H. Feng, “Cochlear implants: system design, integration, and evaluation,” *IEEE Rev. Biomed. Eng.*, vol. 1, pp. 115–142, 2008.
- [10] J. Lee, H. G. Rhew, D. R. Kipke, and M. P. Flynn, “A 64 channel programmable closed-loop neurostimulator with 8 channel neural amplifier and logarithmic ADC,” *IEEE J. Solid-State Circuits*, vol. 45, no. 9, pp. 1935–1945, 2010.
- [11] M. H. Nazari, M. Mujeeb-U-Rahman, and A. Scherer, “An implantable continuous glucose monitoring microsystem in 0.18 $\mu$ m CMOS,” in *Proc. IEEE Symp. VLSI Circuits*, pp. 1–2, 2014.

- [12] S. J. A. Majerus, S. L. Garverick, M. A. Suster, P. C. Fletter, and M. S. Damaser, "Wireless, ultra-low-power implantable sensor for chronic bladder pressure monitoring," *ACM J. Emerg. Technol.*, vol. 8, no. 2, 2012.
- [13] R. J. Sun, S. C. Carreira, Y. Chen, C. Q. Xiang, L. L. Xu, B. Zhang, M. D. Chen, I. Farrow, F. Scarpa, and J. Rossiter, "Stretchable piezoelectric sensing systems for self-powered and wireless health monitoring," *Adv. Mater. Technol.*, vol. 4, no. 5, 2019.
- [14] P. Bingger, M. Zens, and P. Woias, "Highly flexible capacitive strain gauge for continuous long-term blood pressure monitoring," *Biomed. Microdevices*, vol. 14, no. 3, pp. 573–581, 2012.
- [15] N. J. Cleven, J. A. Muntjes, H. Fassbender, U. Urban, M. Gortz, H. Vogt, M. Grafe, T. Gottsche, T. Penzkofer, T. Schmitz-Rode, and W. Mokwa, "A novel fully implantable wireless sensor system for monitoring hypertension patients," *IEEE Trans. Biomed. Eng.*, vol. 59, no. 11, pp. 3124–3130, 2012.
- [16] S. J. Updike, M. C. Shults, B. J. Gilligan, and R. K. Rhodes, "A subcutaneous glucose sensor with improved longevity, dynamic range, and stability of calibration," *Diabetes Care*, vol. 23, no. 2, pp. 208–214, 2000.
- [17] C. L. Lim, C. Byrne, and J. K. W. Lee, "Human thermoregulation and measurement of body temperature in exercise and clinical settings," *Ann. Acad. Med. Singapore*, vol. 37, no. 4, pp. 347–353, 2008.
- [18] D. I. Sessler, "Temperature monitoring and perioperative thermoregulation," *Anesthesiology*, vol. 109, no. 2, pp. 318–338, 2008.
- [19] J. Cilia, D. C. Piper, N. Upton, and J. J. Hagan, "A comparison of rectal and subcutaneous body temperature measurement in the common marmoset," *J. Pharmacol. Toxicol. Methods*, vol. 40, no. 1, pp. 21–26, 1998.
- [20] C. Byrne and C. L. Lim, "The ingestible telemetric body core temperature sensor: a review of validity and exercise applications," *Br. J. Sports Med.*, vol. 41, no. 3, pp. 126–133, 2007.
- [21] D. S. Moran and L. Mendal, "Core temperature measurement: methods and current insights," *Sports Med.*, vol. 32, no. 14, pp. 879–885, 2002.
- [22] J. E. McKenzie and D. W. Osgood, "Validation of a new telemetric core temperature monitor," *J. Therm. Biol.*, vol. 29, no. 7-8, pp. 605–611, 2004.
- [23] B. Hildebrandt, P. Wust, O. Ahlers, A. Dieing, G. Sreenivasa, T. Kerner, R. Felix, and H. Riess, "The cellular and molecular basis of hyperthermia," *Crit. Rev. Oncol. Hematol.*, vol. 43, no. 1, pp. 33–56, 2002.
- [24] P. Wust, B. Hildebrandt, G. Sreenivasa, B. Rau, J. Gellermann, H. Riess, R. Felix, and P. M. Schlag, "Hyperthermia in combined treatment of cancer," *Lancet Oncol.*, vol. 3, no. 8, pp. 487–97, 2002.

- [25] F. A. Jolesz, K. Hynynen, N. McDannold, and C. Tempny, “MR imaging-controlled focused ultrasound ablation: a noninvasive image-guided surgery,” *Magn. Reson. Imaging Clin. N. Am.*, vol. 13, no. 3, pp. 545–60, 2005.
- [26] K. Hynynen, “MRIgHIFU: a tool for image-guided therapeutics,” *J. Magn. Reson. Imaging*, vol. 34, no. 3, pp. 482–493, 2011.
- [27] M. H. Falk and R. D. Issels, “Hyperthermia in oncology,” *Int. J. Hyperthermia*, vol. 17, no. 1, pp. 1–18, 2001.
- [28] J. van der Zee, “Heating the patient: a promising approach?,” *Ann. Oncol.*, vol. 13, no. 8, pp. 1173–1184, 2002.
- [29] S. S. Yoo, A. Bystritsky, J. H. Lee, Y. Z. Zhang, K. Fischer, B. K. Min, N. J. McDannold, A. Pascual-Leone, and F. A. Jolesz, “Focused ultrasound modulates region-specific brain activity,” *NeuroImage*, vol. 56, no. 3, pp. 1267–1275, 2011.
- [30] M. T. Burgess, I. Apostolakis, and E. E. Konofagou, “Power cavitation-guided blood-brain barrier opening with focused ultrasound and microbubbles,” *Phys. Med. Biol.*, vol. 63, no. 6, 2018.
- [31] M. E. Poorman, V. L. Chaplin, K. Wilkens, M. D. Dockery, T. D. Giorgio, W. A. Grissom, and C. F. Caskey, “Open-source, small-animal magnetic resonance-guided focused ultrasound system,” *J. Ther. Ultrasound*, vol. 4, no. 22, pp. 1–16, 2016.
- [32] W. B. Qiu, J. Zhou, Y. Chen, M. Su, G. F. Li, H. X. Zhao, X. Y. Gu, D. Meng, C. Z. Wang, Y. Xiao, K. H. Lam, J. Y. Dai, and H. R. Zheng, “A portable ultrasound system for non-invasive ultrasonic neuro-stimulation,” *IEEE Trans. Neural Syst. Rehabil. Eng.*, vol. 25, no. 12, pp. 2509–2515, 2017.
- [33] W. J. Tyler, Y. Tufail, M. Finsterwald, M. L. Tauchmann, E. J. Olson, and C. Majestic, “Remote excitation of neuronal circuits using low-intensity, low-frequency ultrasound,” *PLoS One*, vol. 3, no. 10, p. e3511, 2008.
- [34] Y. Tufail, A. Matyushov, N. Baldwin, M. L. Tauchmann, J. Georges, A. Yoshihiro, S. I. H. Tillery, and W. J. Tyler, “Transcranial pulsed ultrasound stimulates intact brain circuits,” *Neuron*, vol. 66, no. 5, pp. 681–694, 2010.
- [35] W. Lee, H. C. Kim, Y. Jung, Y. A. Chung, I. U. Song, J. H. Lee, and S. S. Yoo, “Transcranial focused ultrasound stimulation of human primary visual cortex,” *Sci. Rep.*, vol. 6, p. 34026, 2016.
- [36] M. E. Downs, S. A. Lee, G. Yang, S. Kim, Q. Wang, and E. E. Konofagou, “Non-invasive peripheral nerve stimulation via focused ultrasound in vivo,” *Phys. Med. Biol.*, vol. 63, no. 3, 2018.



- [37] M. Kindermann, B. Schwaab, M. Berg, and G. Frohlig, “Longevity of dual chamber pacemakers: device and patient related determinants,” *Pacing Clin. Electrophysiol.*, vol. 24, no. 5, pp. 810–815, 2001.
- [38] R. G. Hauser, “The growing mismatch between patient longevity and the service life of implantable cardioverter-defibrillators,” *J. Amer. College Cardiol.*, vol. 45, no. 12, pp. 2022–2025, 2005.
- [39] J. S. Ho, A. J. Yeh, E. Neofytou, S. Kim, Y. Tanabe, B. Patlolla, R. E. Beygui, and A. S. Y. Poon, “Wireless power transfer to deep-tissue microimplants,” *Proc. Nat. Acad. Sci. USA*, vol. 111, no. 22, pp. 7974–7979, 2014.
- [40] K. Agarwal, R. Jegadeesan, Y. X. Guo, and N. V. Thakor, “Wireless power transfer strategies for implantable bioelectronics,” *IEEE Rev. Biomed. Eng.*, vol. 10, pp. 136–161, 2017.
- [41] T. Sun, X. Xie, and Z. Wang, *Wireless Power Transfer for Medical Microsystems*. New York: Springer, 2013.
- [42] F. Yuan, *CMOS Circuits for Passive Wireless Microsystems*. New York: Springer, 2011.
- [43] T. C. Chang, M. J. Weber, J. Charthad, S. Baltsavias, and A. Arbabian, “Scaling of ultrasound-powered receivers for sub-millimeter wireless implants,” in *Proc. IEEE Biomed. Circuits Syst. Conf. (BioCAS)*, pp. 1–4.
- [44] S. Gollakota, H. Hassanieh, B. Ransford, D. Katabi, and K. Fu, “They can hear your heartbeats: non-invasive security for implantable medical devices,” *SIGCOMM Comput. Commun. Rev.*, vol. 41, no. 4, pp. 2–13, 2011.
- [45] X. Wu, I. Lee, Q. Dong, K. Yang, D. Kim, J. Wang, Y. Peng, Y. Zhang, M. Saligane, M. Yasuda, K. Kumeno, F. Ohno, S. Miyoshi, M. Kawaminami, D. Sylvester, and D. Blaauw, “A 0.04mm<sup>3</sup> 16nW wireless and batteryless sensor system with integrated Cortex-M0+ processor and optical communication for cellular temperature measurement,” in *Proc. IEEE Symp. VLSI Circuits*, pp. 191–192, 2018.
- [46] “Guidelines for evaluating the environmental effects of radiofrequency radiation,” report, Federal Communications Commission, 1996.
- [47] *IEEE Standard for Safety Levels with Respect to Human Exposure to Radio Frequency Electromagnetic Fields, 3 kHz to 300 GHz*, 2005.
- [48] P. Saffari, A. Basaligheh, V. J. Sieben, and K. Moez, “An RF-powered wireless temperature sensor for harsh environment monitoring with non-intermittent operation,” *IEEE Trans. Circuits Syst. I, Reg. Papers*, vol. 65, no. 5, pp. 1529–1542, 2018.

- [49] J. Choi, E. Aklimi, C. Shi, D. Tsai, H. Krishnaswamy, and K. L. Shepard, “Matching the power, voltage, and size of biological systems: A nw-scale, 0.023-mm<sup>3</sup> pulsed 33-ghz radio transmitter operating from a 5 kt/q-supply voltage,” *IEEE Trans. Circuits Syst. I, Reg. Papers*, vol. 62, no. 8, pp. 1950–1958, 2015.
- [50] Y. Ma, Z. Luo, C. Steiger, G. Traverso, and F. Adib, “Enabling deep-tissue networking for miniature medical devices,” in *ACM SIGCOMM*.
- [51] W. D. O’Brien, “Ultrasound-biophysics mechanisms,” *Prog. Biophys. Mol. Biol.*, vol. 93, no. 1-3, pp. 212–255, 2007.
- [52] J. Charthad, M. J. Weber, T. C. Chang, and A. Arbabian, “A mm-sized implantable medical device (IMD) with ultrasonic power transfer and a hybrid bi-directional data link,” *IEEE J. Solid-State Circuits*, vol. 50, no. 8, pp. 1741–1753, 2015.
- [53] A. Sawaby, M. L. Wang, E. So, J. Chien, H. Nan, B. T. Khuri-Yakub, and A. Arbabian, “A wireless implantable ultrasound array receiver for thermoacoustic imaging,” in *Proc. IEEE Symp. VLSI Circuits*, pp. 189–190, 2018.
- [54] M. O. Culjat, D. Goldenberg, P. Tewari, and R. S. Singh, “A review of tissue substitutes for ultrasound imaging,” *Ultrasound Med. Biol.*, vol. 36, no. 6, pp. 861–873, 2010.
- [55] “Information for manufacturers seeking marketing clearance of diagnostic ultrasound systems and transducers,” report, U.S. Department of Health and Human Services, Food and Drug Administration, Center for Devices and Radiological Health, 2008.
- [56] G. Harsányi, *Sensors in Biomedical Applications: Fundamentals, Technology and Applications*. Lancaster, PA: Technomic Pub. Co., 2000.
- [57] K. Opasjumruskit, T. Thanthipwan, O. Sathusen, P. Sirinamarattana, P. Gadmanee, E. Pootarapan, N. Wongkomet, A. Thanachayanont, and M. Tham-sirianunt, “Self-powered wireless temperature sensors exploit rfid technology,” *IEEE Pervasive Comput.*, vol. 5, no. 1, pp. 54–61, 2006.
- [58] P. A. Haddad, G. Gosset, J. P. Raskin, and D. Flandre, “Automated design of a 13.56 MHz 19  $\mu$ W passive rectifier with 72% efficiency under 10  $\mu$ A load,” *IEEE J. Solid-State Circuits*, vol. 51, no. 5, pp. 1290–1301, 2016.
- [59] J. Charthad, T. C. Chang, Z. K. Liu, A. Sawaby, M. J. Weber, S. Baker, F. Gore, S. A. Felt, and A. Arbabian, “A mm-sized wireless implantable device for electrical stimulation of peripheral nerves,” *IEEE Trans. Biomed. Circuits Syst.*, vol. 12, no. 2, pp. 257–270, 2018.
- [60] X. L. Li, W. A. Serdijn, W. Zheng, Y. B. Tian, and B. Zhang, “The injectable neurostimulator: an emerging therapeutic device,” *Trends Biotechnol.*, vol. 33, no. 7, pp. 388–394, 2015.

- [61] I. Lee, W. Jung, H. Ha, S. Jeong, Y. Kim, G. Kim, Z. Foo, J. Y. Sim, D. Sylvester, and D. Blaauw, "An ultra-low-power biomedical chip for injectable pressure monitor," in *Proc. IEEE Biomed. Circuits Syst. Conf. (BioCAS)*, pp. 141–144.
- [62] T. C. Chang, M. J. Weber, J. Charthad, S. Baltsavias, and A. Arbabian, "End-to-end design of efficient ultrasonic power links for scaling towards submillimeter implantable receivers," *IEEE Trans. Biomed. Circuits Syst.*, vol. 12, no. 5, p. 1100–1111, 2018.
- [63] D. Gallego-Perez, N. J. Ferrell, N. Higueta-Castro, and D. J. Hansford, "Versatile methods for the fabrication of polyvinylidene fluoride microstructures," *Biomed. Microdevices*, vol. 12, no. 6, pp. 1009–1017, 2010.
- [64] M. Meng and M. Kiani, "Design and optimization of ultrasonic wireless power transmission links for millimeter-sized biomedical implants," *IEEE Trans. Biomed. Circuits Syst.*, vol. 11, no. 1, pp. 98–107, 2017.
- [65] W. Arden, M. Brillouët, P. Cogez, M. Graef, B. Huizing, and R. Mahnkopf, "More-than-Moore, White Paper." [http://www.itrs2.net/uploads/4/9/7/7/49775221/irc-itrs-mtm-v2\\_3.pdf](http://www.itrs2.net/uploads/4/9/7/7/49775221/irc-itrs-mtm-v2_3.pdf).
- [66] R. K. Cavin, P. Lugli, and V. V. Zhirnov, "Science and engineering beyond Moore's law," *Proc. IEEE*, vol. 100, pp. 1720–1749, 2012.
- [67] G. K. Fedder, R. T. Howe, T. J. K. Liu, and E. P. Quevy, "Technologies for cofabricating MEMS and electronics," *Proc. IEEE*, vol. 96, no. 2, pp. 306–322, 2008.
- [68] M. J. Madou, *Fundamentals of Microfabrication: The Science of Miniaturization*. Boca Raton: CRC Press, 2nd ed., 2002.
- [69] J. M. Hsu, L. Rieth, R. A. Normann, P. Tathireddy, and F. Solzbacher, "Encapsulation of an integrated neural interface device with Parylene C," *IEEE Trans. Biomed. Eng.*, vol. 56, no. 1, pp. 23–29, 2009.
- [70] *Certificate of Compliance, USP Biological Tests*, North American Sci. Assoc., Inc., Northwood, OH, 2005.
- [71] P. J. Chen, D. C. Rodger, S. Saati, M. S. Humayun, and Y. C. Tai, "Microfabricated implantable parylene-based wireless passive intraocular pressure sensors," *J. Microelectromech. Syst.*, vol. 17, no. 6, pp. 1342–1351, 2008.
- [72] C. Shi, T. Costa, J. Elloian, and K. L. Shepard, "Monolithic integration of micron-scale piezoelectric materials with CMOS for biomedical applications," in *IEDM Tech. Dig.*, pp. 4.5.1–4.5.4, 2018.
- [73] S. Jeong, Z. Foo, Y. Lee, J. Y. Sim, D. Blaauw, and D. Sylvester, "A fully-integrated 71 nW CMOS temperature sensor for low power wireless sensor nodes," *IEEE J. Solid-State Circuits*, vol. 49, no. 8, pp. 1682–1693, 2014.

- [74] M. J. Weber, Y. Yoshihara, A. Sawaby, J. Charthad, T. C. Chang, and A. Arbabian, "A miniaturized single-transducer implantable pressure sensor with time-multiplexed ultrasonic data and power links," *IEEE J. Solid-State Circuits*, vol. 53, no. 4, pp. 1089–1101, 2018.
- [75] D. Seo, R. M. Neely, K. Shen, U. Singhal, E. Alon, J. M. Rabaey, J. M. Carmena, and M. M. Maharbiz, "Wireless recording in the peripheral nervous system with ultrasonic neural dust," *Neuron*, vol. 91, no. 3, pp. 529–539, 2016.
- [76] D. Seo, J. M. Carmena, J. M. Rabaey, M. M. Maharbiz, and E. Alon, "Model validation of untethered, ultrasonic neural dust motes for cortical recording," *J. Neurosci. Methods*, vol. 244, pp. 114–122, 2015.
- [77] Y. Zhang and K. L. Shepard, "A 0.6-mm<sup>2</sup> powering and data telemetry system compatible with ultrasound B-mode imaging for freely moving biomedical sensor systems," in *Proc. Custom Integr. Circuits Conf.*, pp. 1–4, 2019.
- [78] M. J. Weber, Y. Yoshihara, A. Sawaby, J. Charthad, T. C. Chang, R. Garland, and A. Arbabian, "A high-precision 36 mm<sup>3</sup> programmable implantable pressure sensor with fully ultrasonic power-up and data link," in *Proc. IEEE Symp. VLSI Circuits*, pp. C104–C105, 2017.
- [79] M. G. Silk, *Ultrasonic Transducers for Nondestructive Testing*. Bristol, UK: Adam Hilger, Ltd., 1984.
- [80] S. Roundy, *Energy scavenging for wireless sensor nodes with a focus on vibration to electricity conversion*. dissertation in engineering-mechanical engineering, 2003.
- [81] T. T. Wang, J. M. Herbert, and A. M. Glass, *The Applications of Ferroelectric Polymers*. New York: Chapman and Hall, 1988.
- [82] M. T. Chorsi, E. J. Curry, H. T. Chorsi, R. Das, J. Baroody, P. K. Purohit, H. Ilies, and T. D. Nguyen, "Piezoelectric biomaterials for sensors and actuators," *Adv. Mater.*, vol. 31, no. 1, 2019.
- [83] S. Roundy, P. K. Wright, and J. M. Rabaey, *Energy Scavenging for Wireless Sensor Networks with Special Focus on Vibrations*. Kluwer Academic Press, 2003.
- [84] H. Ohigashi, "Electromechanical properties of polarized polyvinylidene fluoride films as studied by piezoelectric resonance method," *J. Appl. Phys.*, vol. 47, no. 3, pp. 949–955, 1976.
- [85] H. Kawai, "The piezoelectricity of poly (vinylidene fluoride)," *Jpn. J. Appl. Phys.*, vol. 8, no. 7, pp. 975–976, 1969.
- [86] L. F. Brown, "Design considerations for piezoelectric polymer ultrasound transducers," *IEEE Trans. Ultrason., Ferroelect., Freq. Control*, vol. 47, no. 6, pp. 1377–1396, 2000.

- [87] R. G. Swartz and J. D. Plummer, "On the generation of high-frequency acoustic energy with polyvinylidene fluoride," *IEEE Trans. Sonics Ultrason.*, vol. 27, no. 6, pp. 295–303, 1980.
- [88] Y. J. Hsu, Z. Jia, and I. Kymissis, "A locally amplified strain sensor based on a piezoelectric polymer and organic field-effect transistors," *IEEE Trans. Electron Devices*, vol. 58, no. 3, pp. 910–917, 2011.
- [89] J. Xu, M. J. Dapino, D. Gallego-Perez, and D. Hansford, "Microphone based on Polyvinylidene Fluoride (PVDF) micro-pillars and patterned electrodes," *Sens. Actuator A-Phys.*, vol. 153, no. 1, pp. 24–32, 2009.
- [90] M. Ramos, H. Correia, and S. Lanceros-Mendez, "Atomistic modelling of processes involved in poling of PVDF," *Comput. Mater. Sci.*, vol. 33, no. 1-3, pp. 230–236, 2005.
- [91] L. F. Brown and D. L. Carlson, "Ultrasound transducer models for piezoelectric polymer films," *IEEE Trans. Ultrason., Ferroelect., Freq. Control*, vol. 36, no. 3, pp. 313–318, 1989.
- [92] D. A. Christensen, *Ultrasonic Bioinstrumentation*. New York: Wiley, 1988.
- [93] "Material Properties - Piezo Support." <https://support.piezo.com/article/62-material-properties>, 2019.
- [94] C. H. Park, "On the circuit model of piezoceramics," *J. Intell. Material Syst. Struct.*, vol. 12, no. 7, pp. 515–522, 2001.
- [95] Y. K. Ramadass and A. P. Chandrakasan, "An efficient piezoelectric energy harvesting interface circuit using a bias-flip rectifier and shared inductor," *IEEE J. Solid-State Circuits*, vol. 45, no. 1, pp. 189–204, 2010.
- [96] D. Levacq, C. Liber, V. Dessard, and D. Flandre, "Composite ULP diode fabrication, modelling and applications in multi- $V_{th}$  FD SOI CMOS technology," *Solid-State Electron.*, vol. 48, no. 6, pp. 1017–1025, 2004.
- [97] S. H. Song, A. Kim, and B. Ziaie, "Omni-directional ultrasonic powering for millimeter-scale implantable devices," *IEEE Trans. Biomed. Eng.*, vol. 62, no. 11, pp. 2717–2723, 2015.
- [98] A. L. Lopez-Sanchez and L. W. Schmerr, "Determination of an ultrasonic transducer's sensitivity and impedance in a pulse-echo setup," *IEEE Trans. Ultrason., Ferroelect., Freq. Control*, vol. 53, no. 11, pp. 2101–2112, 2006.
- [99] R. W. Martin and R. A. Sigelmann, "Force and electrical thevenin equivalent circuits and simulations for thickness mode piezoelectric transducers," *J. Acoust. Soc. Am.*, vol. 58, no. 2, pp. 475–489, 1975.
- [100] K. Roy, S. Mukhopadhyay, and H. Mahmoodi-Meimand, "Leakage current mechanisms and leakage reduction techniques in deep-submicrometer CMOS circuits," *Proc. IEEE*, vol. 91, no. 2, pp. 305–327, 2003.

- [101] Q. Dong, K. Yang, D. Blaauw, and D. Sylvester, "A 114-pW PMOS-only, trim-free voltage reference with 0.26% within-wafer inaccuracy for nW systems," in *Proc. IEEE Symp. VLSI Circuits*, pp. 1–2, 2016.
- [102] D. Griffith, P. T. Røine, J. Murdock, and R. Smith, "A 190nW 33kHz RC oscillator with  $\pm 0.21\%$  temperature stability and 4ppm long-term stability," in *IEEE Int. Solid-State Circuits Conf. Dig. Tech. Papers (ISSCC)*, pp. 300–301, 2014.
- [103] G. Gonzalez, *Foundations of Oscillator Circuit Design*. Boston: Artech House, 2007.
- [104] K. Yang, Q. Dong, W. Y. Jung, Y. Q. Zhang, M. Choi, D. Blaauw, and D. Sylvester, "A 0.6nJ  $-0.22/+0.19^\circ\text{C}$  inaccuracy temperature sensor using exponential subthreshold oscillation dependence," in *IEEE Int. Solid-State Circuits Conf. Dig. Tech. Papers (ISSCC)*, pp. 160–160, 2017.
- [105] A. Bellaouar, A. Fridi, M. J. Elmasry, and K. Itoh, "Supply voltage scaling for temperature insensitive CMOS circuit operation," *IEEE Trans. Circuits Syst. II, Analog Digit. Signal Process.*, vol. 45, no. 3, pp. 415–417, 1998.
- [106] C. Q. Tran, H. Kawaguchi, and T. Sakurai, "Low-power high-speed level shifter design for block-level dynamic voltage scaling environment," in *Proc. Int. Conf. Integrated Circuit Design and Technology*, pp. 229–232, 2005.
- [107] J. M. Zhang, W. Chang, V. K. Varadan, and V. V. Varadan, "Passive underwater acoustic damping using shunted piezoelectric coatings," *Smart Mater. Struct.*, vol. 10, no. 2, pp. 414–420, 2001.
- [108] C. Dagdeviren, F. Javid, P. Joe, T. von Erlach, T. Bense, Z. J. Wei, S. Saxton, C. Cleveland, L. Booth, S. McDonnell, J. Collins, A. Hayward, R. Langer, and G. Traverso, "Flexible piezoelectric devices for gastrointestinal motility sensing," *Nat. Biomed. Eng.*, vol. 1, no. 10, pp. 807–817, 2017.
- [109] G. Tang, J. Q. Liu, B. Yang, J. B. Luo, H. S. Liu, Y. G. Li, C. S. Yang, D. N. He, V. D. Dao, K. Tanaka, and S. Sugiyama, "Fabrication and analysis of high-performance piezoelectric MEMS generators," *J. Micromech. Microeng.*, vol. 22, no. 6, 2012.
- [110] T. Costa, C. Shi, K. Tien, and K. L. Shepard, "A CMOS 2D transmit beam-former with integrated PZT ultrasound transducers for neuromodulation," in *Proc. Custom Integr. Circuits Conf.*, pp. 1–4, 2019.
- [111] I. Ladabaum, X. C. Jin, H. T. Soh, A. Atalar, and B. T. Khuri-Yakub, "Surface micromachined capacitive ultrasonic transducers," *IEEE Trans. Ultrason., Ferroelect., Freq. Control*, vol. 45, no. 3, pp. 678–690, 1998.
- [112] B. T. Khuri-Yakub and O. Oralkan, "Capacitive micromachined ultrasonic transducers for medical imaging and therapy," *J. Micromech. Microeng.*, vol. 21, no. 5, 2011.

- [113] Y. Q. Qiu, J. V. Gigliotti, M. Wallace, F. Griggio, C. E. M. Demore, S. Cochran, and S. Trolier-McKinstry, "Piezoelectric micromachined ultrasound transducer (PMUT) arrays for integrated sensing, actuation and imaging," *Sensors*, vol. 15, no. 4, pp. 8020–8041, 2015.
- [114] F. Akasheh, T. Myers, J. D. Fraser, S. Bose, and A. Bandyopadhyay, "Development of piezoelectric micromachined ultrasonic transducers," *Sens. Actuator A-Phys.*, vol. 111, no. 2-3, pp. 275–287, 2004.
- [115] D. Tsai, D. Sawyer, A. Bradd, R. Yuste, and K. L. Shepard, "A very large-scale microelectrode array for cellular-resolution electrophysiology," *Nat. Commun.*, vol. 8, 2017.
- [116] P. Ueberschlag, "PVDF piezoelectric polymer," *Sens. Rev.*, vol. 21, no. 2, pp. 118–126, 2001.
- [117] R. H. Tancrrell, D. T. Wilson, and D. Ricketts, "Properties of PVDF polymer for sonar," in *IEEE Ultrason. Symp.*, pp. 624–629.
- [118] J. S. Lee, G. H. Kim, S. M. Hong, H. J. Choi, and Y. Seo, "Surface functionalization of a poly(vinylidene fluoride): effect on the adhesive and piezoelectric properties," *ACS Appl. Mater. Interfaces*, vol. 1, no. 12, pp. 2902–2908, 2009.
- [119] C. L. Sun, J. Shi, D. J. Bayerl, and X. D. Wang, "PVDF microbelts for harvesting energy from respiration," *Energy Environ. Sci.*, vol. 4, no. 11, pp. 4508–4512, 2011.
- [120] T. Sharma, S. S. Je, B. Gill, and J. X. J. Zhang, "Patterning piezoelectric thin film PVDF-TrFE based pressure sensor for catheter application," *Sens. Actuator A-Phys.*, vol. 177, pp. 87–92, 2012.
- [121] Y. Bormashenko, R. Pogreb, O. Stanevsky, and E. Bormashenko, "Vibrational spectrum of PVDF and its interpretation," *Polym. Test.*, vol. 23, no. 7, pp. 791–796, 2004.
- [122] R. Gregorio and E. M. Ueno, "Effect of crystalline phase, orientation and temperature on the dielectric properties of poly (vinylidene fluoride) (PVDF)," *J. Mater. Sci.*, vol. 34, no. 18, pp. 4489–4500, 1999.
- [123] P. Martins, A. C. Lopes, and S. Lanceros-Mendez, "Electroactive phases of poly(vinylidene fluoride): Determination, processing and applications," *Prog. Polym. Sci.*, vol. 39, no. 4, pp. 683–706, 2014.
- [124] C. Chen, S. B. Raghunathan, Z. Yu, M. Shabanimotlagh, Z. Chen, Z. Y. Chang, S. Blaak, C. Prins, J. Ponte, E. Noothout, H. J. Vos, J. G. Bosch, M. D. Verweij, N. de Jong, and M. A. Pertijs, "A prototype PZT matrix transducer with low-power integrated receive ASIC for 3-D transesophageal echocardiography," *IEEE Trans. Ultrason., Ferroelect., Freq. Control*, vol. 63, no. 1, pp. 47–59, 2016.

- [125] C. Chen, Z. Chen, D. Bera, S. B. Raghunathan, M. Shabanmotlagh, E. Niothout, Z. Y. Chang, J. Ponte, C. Prins, H. J. Vos, J. G. Bosch, M. D. Verweij, N. de Jong, and M. A. P. Pertijs, "A front-end ASIC with receive sub-array beamforming integrated with a  $32 \times 32$  PZT matrix transducer for 3-D transesophageal echocardiography," *IEEE J. Solid-State Circuits*, vol. 52, no. 4, pp. 994–1006, 2017.
- [126] J. S. Park, S. H. Lee, S. S. Park, J. W. Cho, S. W. Jung, J. H. Han, and S. G. Kang, "Acoustic and electromechanical properties of 1-3 PZT composites for ultrasonic transducer arrays fabricated by sacrificial micro PMMA mold," *Sens. Actuator A-Phys.*, vol. 108, no. 1-3, pp. 206–211, 2003.
- [127] C. H. Wang, X. S. Li, H. J. Hu, L. Zhang, Z. L. Huang, M. Y. Lin, Z. R. Zhang, Z. N. Yin, B. Huang, H. Gong, S. Bhaskaran, Y. Gu, M. Makihata, Y. X. Guo, Y. S. Lei, Y. M. Chen, C. F. Wang, Y. Li, T. J. Zhang, Z. Y. Chen, A. P. Pisano, L. F. Zhang, Q. F. Zhou, and S. Xu, "Monitoring of the central blood pressure waveform via a conformal ultrasonic device," *Nature Biomed. Eng.*, vol. 2, no. 9, pp. 687–695, 2018.
- [128] "Verasonics' Transducers - Verasonics." <https://verasonics.com/verasonics-transducers/>.
- [129] "The Vantage Systems Brochure." <https://verasonics.com/wp-content/uploads/2019/04/Vantage-Systems-Brochure.pdf>.
- [130] T. L. Szabo, *Diagnostic Ultrasound Imaging: Inside Out*. Burlington, MA: Elsevier, 2004.
- [131] M. G. Shapiro, K. Homma, S. Villarreal, C.-P. Richter, and F. Bezanilla, "Infrared light excites cells by changing their electrical capacitance," *Nat. Commun.*, vol. 3, p. 736, 2012.